DYNAMICS OF SEMICONDUCTOR LASERS UNDER EXTERNAL OPTICAL INJECTION

Thomas B. Simpson and Jia-ming Liu

Jaycor, Inc
P.O. Box 85154
San Diego, CA 92186-5154

August 1997

Final Report

19971202 013

APPROVED FOR PUBLIC RELEASE; DISTRIBUTION IS UNLIMITED.

DTIC QUALITY INSPECTED 3

PHILLIPS LABORATORY
Lasers and Imaging Directorate
AIR FORCE MATERIEL COMMAND
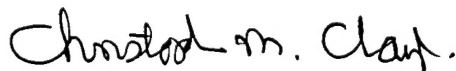**KIRTLAND AIR FORCE BASE, NM 87117-5776**

PL-TR-97-1143

This report has been approved for publication.
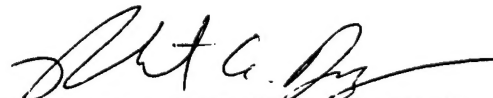

CHRISTOPHER M. CLAYTON
Project Manager

FOR THE COMMANDER

WILLIAM J. WELKER, LtCol USAF   ROBERT A. DURYEA, Col, USAF
Chief, Optical Sensing Division   Director, Lasers and Imaging Directorate

REPORT DOCUMENTATION PAGE

Form Approved OMB No. 074-0188

1. AGENCY USE ONLY (Leave blank)	2. REPORT DATE	3. REPORT TYPE AND DATES COVERED
	August 1997	Final; Sep 94 – Aug 97

4. TITLE AND SUBTITLE
Dynamics of Semiconductor Lasers Under External Optical Injection

5. FUNDING NUMBERS
C: F29601-94-C-0166
PE: 62601F
PR: 3326
TA: LH
WU: AK

6. AUTHOR(S)
Thomas B. Simpson
Jia-ming Liu

7. PERFORMING ORGANIZATION NAME(S) AND ADDRESS(ES)

Jaycor, Inc
P.O. Box85154
San Diego, CA 92186-5154

8. PERFORMING ORGANIZATION REPORT NUMBER
J211-97-0071/7211

9. SPONSORING / MONITORING AGENCY NAME(S) AND ADDRESS(ES)

Phillips Laboratory/LIMS
3550 Aberdeen Ave SE
Kirtland AFB NM 87117-5776

10. SPONSORING / MONITORING AGENCY REPORT NUMBER
PL-TR-97-1143

11. SUPPLEMENTARY NOTES

12a. DISTRIBUTION / AVAILABILITY STATEMENT
Approved for public release, distribution is unlimited

12b. DISTRIBUTION CODE

13. ABSTRACT (Maximum 200 Words)
Injection of an external optical signal into the oscillating mode of a semiconductor laser can modify the coupling between the circulating optical field and the carrier density (gain medium). The external optical signal modifies both the gain and the refractive index of the semiconductor gain medium by changing the free-carrier density. Depending on the strength of the optical injection and the frequency offset between the injected signal and the free-running oscillation frequency, this can lead to modulated output including multiwave mixing, unstable dynamics, and deterministic chaos, or to significantly improved modulation and noise characteristics relative to the free-running case. Experimental investigations were coupled with numerical and analytical modeling to investigate the modified output in a commercially available laser diode and a vertical-cavity surface-emitting laser (VCSEL). The modeling used a conventional coupled-equation model which, we found, identifies the key phenomena that we observe in our data.

14. SUBJECT TERMS
semiconductor lasers, nonlinear dynamics, injection locking, bandwidth enhancement, noise reduction

15. NUMBER OF PAGES
134

16. PRICE CODE

17. SECURITY CLASSIFICATION OF REPORT	18. SECURITY CLASSIFICATION OF THIS PAGE	19. SECURITY CLASSIFICATION OF ABSTRACT	20. LIMITATION OF ABSTRACT
Unclassified	Unclassified	Unclassified	Unlimited

CONTENTS

FIGURES

ACKNOWLEDGEMENTS

1.0 INTRODUCTION

Semiconductor lasers have been the subject of considerable research and development activity over the past 30 years and now are used in a variety of applications including compact disc players and telecommunications. They are also important as a test system for the understanding of many key features of laser operation. Due to the small size of the optical cavities that can be constructed with semiconductor material, and the high gain of that material, features of the optical spectrum can be related back to fundamental quantum noise sources of the system [1]. Semiconductor lasers differ from many other laser systems in that the free carriers which control the optical gain of the system also have a strong effect on the refractive index, giving it the characteristics of a detuned oscillator [2]. This feature leads to an enhancement of the linewidth of a semiconductor laser [3] and also has been exploited to induce unstable dynamics and deterministic chaos in semiconductor lasers by the addition of an extra external modulation [4] such as a current modulation [5], weak optical feedback [6] or external optical injection [7].

As a test system for studying nonlinear dynamics in semiconductor lasers, the laser undergoing external optical injection has certain advantages. The use of an independent laser, rather than feedback from the laser under investigation, adds the freedom to control the amplitude and offset frequency of the perturbing optical field. Optical injection, as opposed to current modulation, does not require high-speed electronics and bypasses the electronic parasitic effects that can obscure the intrinsic laser properties. Experimental investigations of nonlinear dynamics in a conventional edge-emitting Fabry-Perot laser diode biased well above threshold have shown quantitative agreement with a coupled equation model for single-mode laser operation [7, 8, 9, 10]. Here, we summarize that work and present the results in the form of a mapping of the observed dynamics of the laser output as a function of the amplitude and detuning of the external optical injection. Many features of the observed dynamics are expected to appear in a variety of laser structures, while some relate to characteristics of the specific laser structure. We also present results on optical injection of a vertical cavity

1

surface emitting laser (VCSEL). This laser displayed, in its free-running condition when biased near threshold, an optical output with a near-Gaussian, as opposed to a Lorentzian, spectrum. When the external optical injection destabilizes the dynamics of this system, the optical spectrum shows spectral spikes and holes in the Gaussian envelope. As before, all of the results can be reproduced with the coupled equation model.

In recent work, we have proposed that the modulation bandwidth and broadband noise characteristics of a conventional, edge-emitting laser diode are significantly improved under appropriate injection locking to a stable master laser [11, 12]. By strong, we mean an injection power on the order of 10^{-2} to 2-3 $\times$ 10^{-1} of the output power of the free-running slave laser. Calculations have indicated that the modulation bandwidth of the injection-locked laser could be improved beyond the theoretical limit of the free-running laser. This bandwidth improvement can be accompanied by significant reduction in the noise power of the laser. Significantly, the injected optical power required to induce these changes can be only a few percent of the free-running output power of the laser. Injection locking of a semiconductor laser also allows one to tailor the response characteristics to emphasize a specific feature such as modulation bandwidth, flatness of response, or gain at a particular modulation frequency. This capability can be used to generate a wide variety of output characteristics with controlled amplitude and phase. A block diagram of a generic transceiver element built around an injection-locked laser diode is shown in Figure 1. The master laser is a stable, narrowband laser oscillator which may have very poor high-frequency modulation characteristics. Between the master and slave laser, or multiple slave lasers, are optical elements which provide the proper coupling between the lasers and external signals and minimize unwanted feedback. The transceiver can be operated in the transmit mode where an electronic signal can be added to the bias current of the slave laser to produce an analog or digital modulation signal. Because the slave laser is operated as an injection-locked oscillator, it can have relatively poor free-running noise characteristics to emphasize high-frequency response. In the receive mode, the slave laser becomes a bandwidth tunable filter and preamplifier for modulated optical input to the photodetector. The master laser controls the central wavelength of the filter. By adjusting the bias of the slave laser, the bandwidth

2
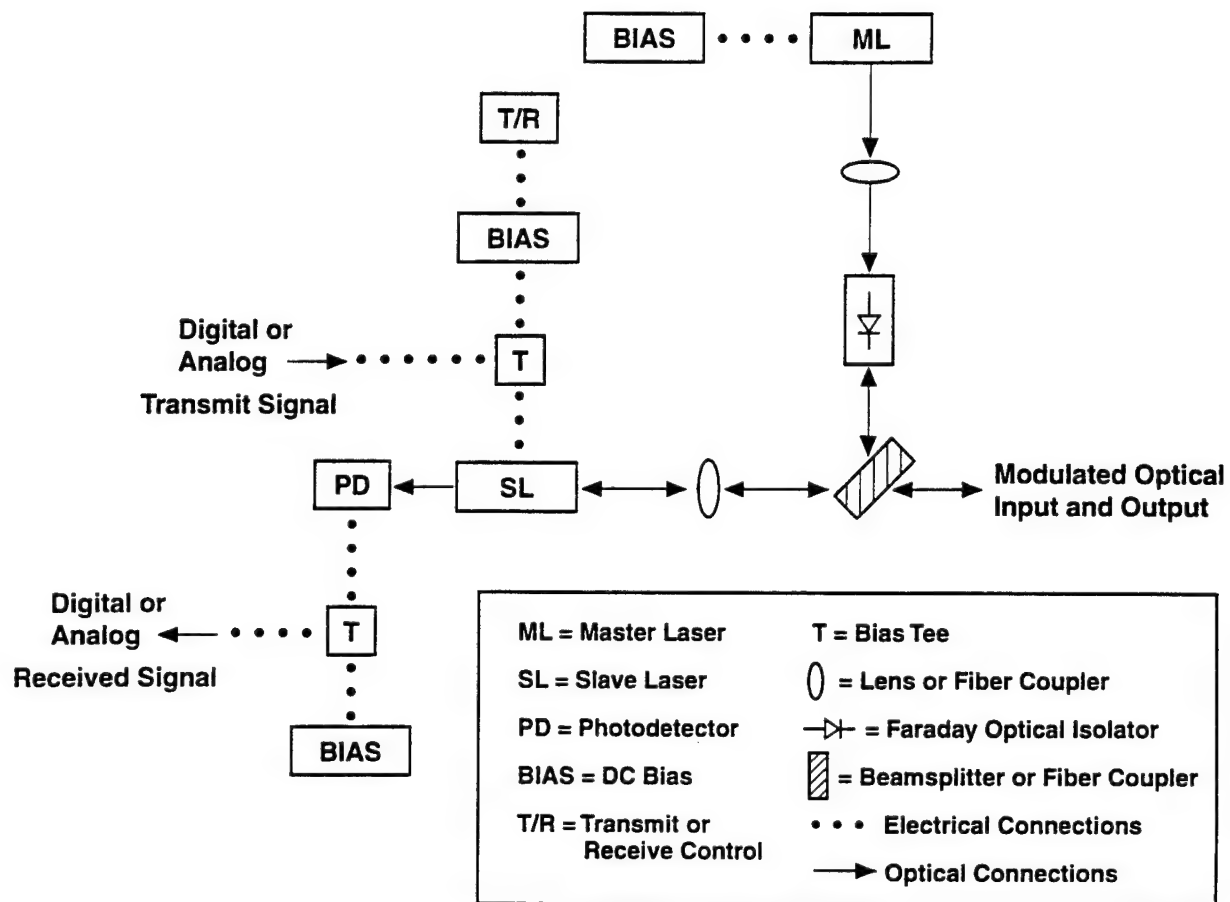
Figure 1: Transceiver concept using injection-locked semiconductor lasers.

of the filter can be controlled. Because the master laser only has to inject a locking signal of a few percent of the power of the slave laser, a single master laser can control multiple transceiver elements.

In this report, we summarize our findings on the nonlinear dynamics and bandwidth enhancement which can be induced in a semiconductor laser under external optical injection. In the next section, we review the model of a semiconductor laser subject to a strong optical signal, first describing the full nonlinear coupled equations and the proceeding to a perturbation analysis of the modulation characteristics of an injection-locked semiconductor laser. This is followed by descriptions of our experimental apparatus and some general features of the specific semiconductor lasers under investigation. Because nonlinear dynamics plays a critical role in the understanding of the semiconductor laser under strong optical injection, we then discuss a detailed mapping of the kinds of output dynamics that we observe under external optical injection. The mapping is generated by comparing optical spectra generated from calculated time-series data with and without noise terms with the spectra we observe. Removing the noise terms allows us to identify the underlying deterministic dynamics in a way which cannot be duplicated experimentally. We then discuss some interesting features of the VCSEL which were not observed in our previous studies of a conventional, edge-emitting laser diode, with emphasis on VCSEL characteristics near threshold. There has been considerable controversy about the description of microcavity lasers, like VCSELs, near threshold. However, we show how our model recovers all of the novel features that we observe. Next, we discuss the output characteristics of an injection-locked semiconductor laser under strong injection where stable dynamics are expected to be observed. We confirm the capability of the model to predict the enhancement of the characteristic resonance frequencies of the injection-locked laser and the noise reduction. The model presented in past publications [7, 12, 13] is also augmented by the inclusion of feedback from optical elements. As we describe below, we found that feedback effects could be observed in our data. However, the coupled-equation model correctly shows the influence of feedback. We then describe the measurements which showed that injection locking could be used to achieve modulation

bandwidths beyond the theoretical limit of the free-running laser diode. Even with the feedback, the enhanced operating characteristics could still be observed. Finally, we conclude with a brief discussion of possible future research.

2.0 COUPLED EQUATION MODEL

Semiconductor lasers have been the subject of extensive modelling. Like a variety of other laser systems, the polarization of the semiconductor gain medium has a relaxation rate which dominates all other dynamic frequencies in the system, except the optical emission frequency. In these lasers, called Class B lasers, the differential equation describing the polarization of the medium, P, can be adiabatically eliminated by writing P explicitly as a function of other parameters of the laser:

$$P = -\epsilon_0 \frac{nc}{\omega_L}(b+i)gAe^{-i\omega_0 t} \tag{1}$$

Here, the gain, g, and the linewidth enhancement factor, b, relate the complex intracavity field, A, and the polarization induced by the free carriers which make up the gain medium. In Equation 1, ϵ_0 is the permittivity of free space, n is the refractive index of the semiconductor medium, c is the speed of light and ω_0 is the optical frequency of the oscillating mode. The gain is assumed to obey a linear dependence on changes in the carrier density, with coefficient g_N, and changes in the photon density, with coefficient g_p, about an appropriately chosen operating point [13].

An isolated, single-mode laser of this type that is biased well above threshold is sufficiently described by only two rate equations: one for the photon density and another for the population density of the gain medium [2, 14]. When the laser is coupled to the outside world and is subject to the perturbation of external sources, such as the vacuum field or external optical signals, an equation for the complex, oscillating electric field must replace the simpler equation for the photon density. The two equations, one for the complex oscillating field within the laser cavity and one for the carrier density, which describe the dynamics of the single-mode laser under external optical injection are [7, 13, 15]:

$$\frac{dA}{dt} = -\frac{\gamma_c}{2}A + i(\omega_0 - \omega_c)A + \frac{\Gamma}{2}(1-ib)gA + F + \eta A_i \exp(-i\Omega t), \tag{2}$$

$$\frac{dN}{dt} = \frac{J}{ed} - \gamma_s N - \frac{2\epsilon_0 n^2}{\hbar\omega_0}g|A|^2. \tag{3}$$

6

Here, γ_c is the cavity decay rate, ω_c is the longitudinal mode frequency of the cold laser cavity, and Γ is the confinement factor which gives the spatial overlap between the active gain volume and the optical mode volume. N is the carrier density, J is the injection current density, e is the electronic charge, d is the active layer thickness, γ_s is the spontaneous carrier decay rate, and n is the refractive index of the semiconductor medium. Two source terms in the field equation are due to: 1) external optical injection with η being the coupling parameter, A_i the amplitude of the external field and Ω the offset frequency with respect to the free-running frequency of the injected laser, and 2) noise. F is the complex Langevin source term for the field noise due to spontaneous emission into the mode and external coupling out of the mode [3, 16].

$$\langle F(t) \rangle = 0 \tag{4}$$

$$\langle F(t)F^*(t') \rangle = R_{sp}\delta(t - t') \tag{5}$$

$$\langle F(t)F(t') \rangle = 0 \tag{6}$$

where R_{sp} gives the strength of the field source term. The noise source terms in the carrier equation are omitted. They are relatively unimportant in determining the optical field spectra which we will emphasize. These equations form the basis for a full, nonlinear analysis of the semiconductor laser under external optical injection. The full nonlinear form must be retained when the laser output departs from stable operation under external optical injection. The equations have proven to be quite robust and can be applied for arbitrary values of the injected field both inside and outside the range of injection-locked operation. While variations in spatial characteristics can be retained in this model [17], generally it is assumed that spatial inhomogeneities can be averaged over the cavity and a lumped element approach can be used.

2.1 SMALL-SIGNAL MODULATION ANALYSIS

In previous publications, we have described the weak injection limit and pointed out how key dynamic parameters of a semiconductor laser can be determined from the optical modulation

spectra [13, 25]. We have also described similarities between the noise spectra and the weak external-field modulation spectra of a free-running semiconductor laser [15]. In these analyses, we used the lumped-element model of the semiconductor laser, emphasizing certain key features. The modulation characteristics are determined from a perturbation analysis about the injection-modified operating point. We next make a more complete explication of the small signal analysis for a semiconductor laser subject to a strong, externally injected field which satisfies the conditions for injection locking. This small-signal analysis uses both a weak injection current and a second, weak optical field as the modulation sources. Both optical and current modulation characteristics are of interest in a variety of applications. We have attempted to use notation consistent with our earlier work on weak optical injection in semiconductor lasers [13]. The goals will be to further explain the similarities and differences between the modulation characteristics of the free-running and the injection-locked lasers and to show the effects of a strong external field on the modulation characteristics of the laser. Specifically, we emphasize the strong optical injection regime where enhancement of the modulation bandwidth and a broad tuning range for stable injection locking can be achieved. Past work on the modulation characteristics of injection-locked semiconductor lasers has not emphasized this regime [18, 19, 20, 21, 22]. We will also compare the results of our analysis of modulation in an optical cavity with past analyses of four-wave mixing in semiconductor travelling-wave amplifier configurations [23, 24] to show that the optical cavity plays a key role in the modified modulation characteristics. We will be able to use some of the results described here to analyze the noise spectra of a semiconductor laser subject to strong optical injection. A more complete analysis of the noise characteristics requires a full nonlinear treatment and will be described later in this report.

2.1.1 Theoretical Model

In our modulation analysis, we will consider a single-mode semiconductor laser subject to external optical injection and/or current modulation [7, 13, 25]. When free running, the laser is assumed to be biased above the threshold for oscillation. We replace the noise source term in the field equation with a second external optical injection field. This field is assumed

8

to be sufficiently weak so that it will act as a linear probe. A modulation current will also be added to the injection current. The modulation of the injection current will also be small and be used as a linear probe. The noise terms are dropped for the modulation analysis. The interaction can be described by two coupled equations:

$$\frac{dA}{dt} = -\frac{\gamma_c}{2}A + i(\omega_L - \omega_c)A + \frac{\Gamma}{2}(1 - ib)gA + \eta(A_l + A_i e^{-i\Omega t}), \tag{7}$$

$$\frac{dN}{dt} = \frac{J + J_m \cos(\Omega t)}{ed} - \gamma_s N - \frac{2\epsilon_0 n^2}{\hbar \omega_L}g\,|A|^2\,, \tag{8}$$

where A is the total complex intracavity field amplitude at the locked oscillating frequency ω_L, γ_c is the cavity decay rate, ω_c is the longitudinal-mode frequency of the cold laser cavity, Γ is the confinement factor, A_l and A_i are the amplitudes of the strong injection signal at the locking frequency and the weak probe signal at $\omega_L + \Omega$, respectively, η is the coupling rate, N is the carrier density, J is the steady-state injection current density, J_m is the weak current modulation at a frequency Ω, e is the electronic charge, d is the active layer thickness and γ_s is the spontaneous carrier decay rate.

The exact functional dependence of the gain on parameters such as the carrier density and the optical-field intensity is unknown, but it is important to consider the gain coefficient $g(N_L, S_L)$ as a function of the carrier density, N_L, and the intracavity photon density, S_L [13]. The subscript L indicates the values of the parameters in the injection-locked condition. Therefore, we make the assumption that the gain can be modeled perturbatively about a steady-state operating point determined by the injection current, J, the carrier density, N_L, the field amplitude, $|A_L|$, and the phase relative to the strong injection field, ϕ_L. The photon density is related to the field amplitude through:

$$S_L \simeq \frac{2n^2\epsilon_0}{\hbar \omega_L}|A_L|^2. \tag{9}$$

The steady-state operating point is found by setting the time derivatives and the weak-modulation terms to zero in Equations 7 and 8. At the operating point, this procedure

9

yields:

$$|A_L| = \frac{2\eta|A_l|\cos\phi_L}{\gamma_c - \Gamma g_L}, \tag{10}$$

$$\phi_L = \sin^{-1}\left[\frac{(\omega_L - \omega_c - b\Gamma g_L/2)|A_L|}{\eta|A_l|}\right], \tag{11}$$

$$N_L = \frac{1}{\gamma_s}\left(\frac{J}{ed} - \frac{2\epsilon_0 n^2}{\hbar\omega_L}g_L|A_L|^2\right). \tag{12}$$

The dependence of the gain on the carrier density and the photon density is included in the analysis through two new relaxation rates, γ_{nL} and γ_{pL}. While γ_s and γ_c are assumed to be constant, γ_{nL} and γ_{pL} are proportional to the intracavity photon density through the following relations:

$$\gamma_{nL} = g_n S_L = \left.\frac{\partial g}{\partial N}\right|_{N_L} S_L \quad \text{and} \quad \gamma_{pL} = -\Gamma g_p S_L = -\Gamma \left.\frac{\partial g}{\partial S}\right|_{N_L} S_L, \tag{13}$$

where g_n and g_p are the differential and nonlinear gain parameters defined as the derivatives of the gain coefficient, g, with respect to the carrier density and the photon density, respectively, evaluated at the operating point.

These definitions can be related back to our previous definitions used for weak injection in a free-running, single-mode laser by setting $A_l = 0$, returning the operating point to its free-running value [13]. This requires $\omega_L \Rightarrow \omega_0$, the free-running optical frequency, $A_L \Rightarrow A_0$, the free-running average field amplitude, and $N_L \Rightarrow \overline{N}$, the free-running average carrier density, as previously defined. Because the dynamic parameters of free-running laser diodes can be experimentally determined [13, 26], we can use these dynamic parameters in an analysis of the injection-locked laser. First, we must relate the oscillation points of the free-running and the injection-locked lasers. Within the injection-locked region, the frequency and phase of the slave laser are shifted relative to the free-running values. The frequency and phase shifts are related by [18, 19]:

$$\omega_L - \omega_0 = -bU + V. \tag{14}$$

Here, $U = \eta|A_l/A_L|\cos\phi_L$ is the in-phase injection term and $V = \eta|A_l/A_L|\sin\phi_L$ is the quadrature term. From Equations 10 and 11, the gain defect at the injection-locked operating point is $2U$ and the frequency offset, $\omega_L - \omega_c - b\Gamma g_L/2$, is V. Equation 14 places an upper bound on the detuning range for injection-locked operation: $|\omega_L - \omega_0| < \sqrt{1+b^2}\,\eta|A_l/A_L|$. The injection-locked range is further limited by the requirement that the injection-locked solution has a lower gain than the free-running solution [19]. The injection-locked solution is always in competition with an unlocked solution with unbounded phase. From Equation 10 this requires that $|\phi_L| < \pi/2$, or $-\sqrt{1+b^2}\,\eta|A_l/A_L| < \omega_L - \omega_0 < \eta|A_l/A_L|$.

The relation between $|A_L|$ and the free-running value, $|A_0|$, can be obtained through the cubic equation:

$$a_L^3 - Ya_L^2 - a_L - Y\frac{\gamma_s}{\gamma_n} = 0 \tag{15}$$

where $a_L = |A_L/A_0|$, γ_n is the field-induced decay rate due to the differential gain term for the free-running laser [13] and the factor, Y, is given by:

$$Y = 2\frac{\gamma_c\gamma_n}{\Omega_r^2}\xi\cos(\phi_L). \tag{16}$$

Here, Ω_r is the radial frequency of the carrier-field resonance, $\Omega_r^2 = \gamma_c\gamma_n + \gamma_s\gamma_p$, where γ_p is the field-induced decay rate due to the nonlinear gain term for the free-running laser [13], and $\xi = \eta|A_l|/\gamma_c|A_0|$ is the injection parameter [8]. The injected signal also modifies the threshold for oscillation. The pump parameter, $\tilde{J}_L = (J/ed)/\gamma_s N_L - 1$, of the locked oscillator is related to the free-running pump parameter, $\tilde{J} = (J/ed)/\gamma_s\overline{N} - 1$ [8], by:

$$\tilde{J}_L = \frac{[1 - 2\xi\cos(\phi_L)/a_L]a_L^2\tilde{J}}{1 - \gamma_s\tilde{J}[2\xi\cos(\phi_L)/a_L - \gamma_p(a_L^2-1)/\gamma_c]/\gamma_n} \tag{17}$$

11

Alternatively, $|A_0|$ and $|A_L|$ are related through an equation based on the injection-locked parameters:

$$a_L^2 = \frac{\Omega_L^2 + 2U\gamma_{nL}}{\Omega_L^2 - 2U\gamma_s} \tag{18}$$

where the factor $\Omega_L^2 = (\gamma_c - 2U)\gamma_{nL} + \gamma_s\gamma_{pL}$ is used for convenience.

We will illustrate the effects of injection locking in semiconductor lasers using the experimentally measured parameters of a commercially available, index-guided, GaAs/AlGaAs quantum-well laser diode. The relevant parameters for this laser, along with a reference list of key symbols, are summarized in Table 1. For the calculations described in this paper we will set $\tilde{J} = 2/3$ where experimental measurements have been consistent with the model [11]. Figure 2 is a mapping of the operating point characteristics in the detuning-frequency versus injection-level plane. The injection-locking range is bounded by the lines of constant phase at $\phi_L = \pi/2$, in the positive frequency range, and $\phi_L = -\arctan b^{-1}$, at negative offset frequencies. Shown in Figure 3(a) are lines of constant phase at $\phi_L = \arctan b$, the zero detuning axis, $\phi_L = 0.67 \approx 0.5 \arctan b$, and $\phi_L = 0$. The $\phi_L = 0$ line is barely distinguishable from the lower injection-locking boundary. The upper bound on the locking range is also a line of constant amplitude, $a_L = 1$. When the injection fields are small compared to the output field, $\xi \lesssim 0.05$, the lines of constant ϕ_L are nearly straight because the circulating field is essentially unchanged by the injection. At higher injection levels, the lines of constant phase at $\phi_L = \pi/2$ and at $\phi_L = \arctan b$ remain straight while the lines at $\phi_L = 0.67$, $\phi_L = 0$, and $\phi_L = -\arctan b^{-1}$ bend over as $|A_L|$ begins to depend on $|A_l|$. For the laser under consideration, at $\tilde{J} = 2/3$ the linearized treatment of g begins to break down for $a_L > 2$, when γ_{nL} and γ_{pL} become a sizeable fraction of γ_c. In addition, the applicability of a single-mode model must be questioned for large detunings, on the order of the longitudinal mode spacing. The laser with the parameters listed in Table 1 has a mode spacing of ≈ 86 GHz.

Before continuing, we wish to consider one limiting case of a semiconductor laser under strong optical injection. It is often true in semiconductor lasers that $\gamma_s \ll \gamma_c$ while γ_{pL} is somewhat larger but of the same order as γ_{nL}. When the free-running laser is biased just

Parameter	Symbol	Reference/Value*
Polarization of gain medium	P	Equation 1
Gain	g	Equation 1
Linewidth enhancement factor	b	4
Differential gain parameter	g_n	Reference [13]
Nonlinear gain parameter	g_p	Reference [13]
Intracavity field	A	Equation 2
Cavity decay rate	γ_c	2.4×10^{11} s^{-1}
External modulation Field	A_i	Equation 2
Injection coupling rate	η	Equation 2
Carrier Density	N	Equation 3
Spontaneous carrier relaxation rate	γ_s	1.458×10^9 s^{-1}
Steady-state injection current density	J/ed	Equation 3
Modulation offset frequency	Ω	Equations 2 and 3
Free-running oscillation frequency	ω_0	Equation 2
Free-running steady-state field	A_0	Reference [13]
Free-running steady-state carrier density	$\overline{N}$	Reference [13]
Free-running pump parameter	$\tilde{J}$	Reference [11]
Field-induced carrier decay rate	γ_n	$2\tilde{J} \times 10^9$ s^{-1}
Nonlinear gain decay rate	γ_p	$3.6\tilde{J} \times 10^9$ s^{-1}
Relaxation resonance angular frequency	Ω_r	$(\gamma_c\gamma_n + \gamma_s\gamma_p)^{1/2}$
Total carrier relaxation rate	γ_r	$\gamma_s + \gamma_n + \gamma_p$
External locking field	A_l	Equation 7
Locked oscillation frequency	ω_L	Equation 7
Modulation current amplitude	J_m	Equation 8
Locked steady-state field amplitude	$|A_L|$	Equation 9
Locked Photon Density	S_L	Equation 9
Locked steady-state phase	ϕ_L	Equation 11
Locked steady-state carrier density	N_L	Equation 12
In-phase locking parameter	U	$\eta(|A_l|/|A_L|)\cos\phi_L$
Quadrature locking parameter	V	$\eta(|A_l|/|A_L|)\sin\phi_L$
Normalized steady-state amplitude	a_L	$|A_L|/|A_0|$
Injection parameter	ξ	$\eta|A_l|/\gamma_c|A_0|$
Locked Pump parameter	$\tilde{J}_L$	Equation 17
Normalized modulation field amplitude	a	$|A|/|A_L| - 1$
Phase of the modulation field	$\tilde{\phi}$	Equation 23
Normalized modulation carrier density	$\tilde{n}$	$N/N_L - 1$
Normalized modulation current	$\tilde{J}_m$	$J_m/2ed\gamma_s N_L$
Locked field-induced carrier decay rate	γ_{nL}	$\gamma_n a_L^2$
Locked nonlinear gain decay rate	γ_{pL}	$\gamma_p a_L^2$
Reference angular frequency	Ω_L	$[(\gamma_c - 2U)\gamma_{nL} + \gamma_s\gamma_{pL}]^{1/2}$
Locked decay rate	γ_{rL}	$\gamma_s + \gamma_{nL} + \gamma_{pL} + U$

TABLE 1. Relevant symbols and experimentally determined parameters of a conventional, edge-emitting laser diode.
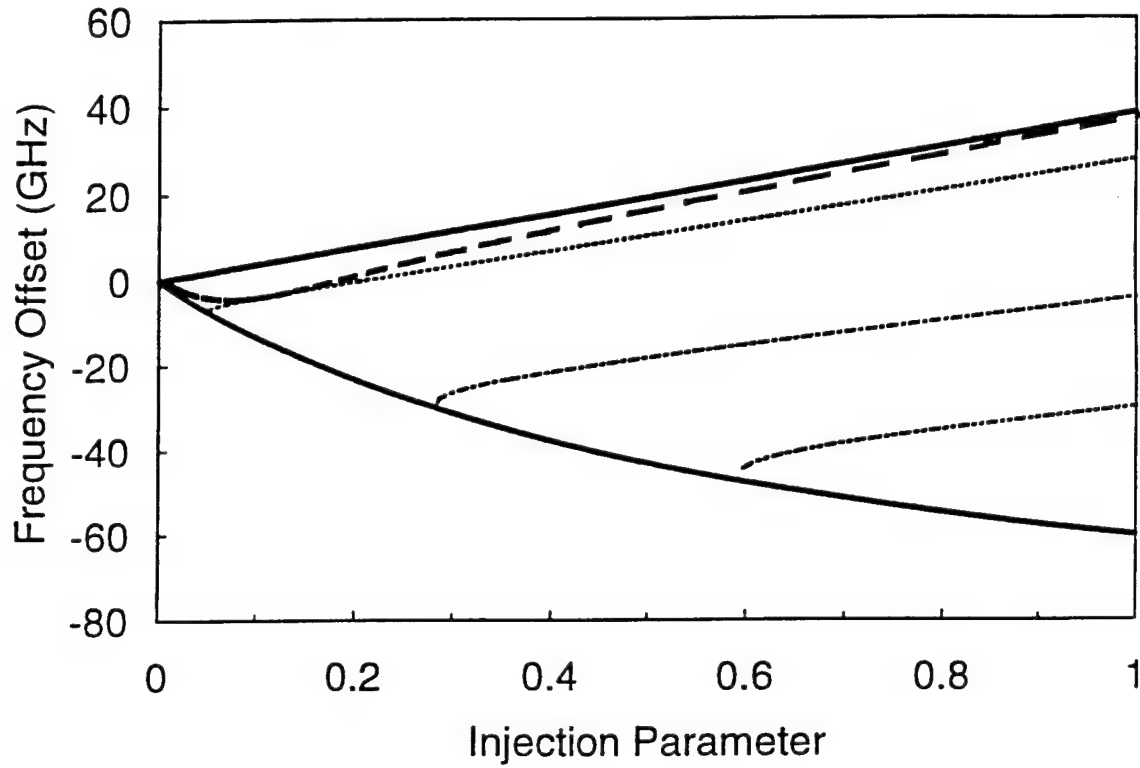
Figure 2: Mapping of the locking and stability characteristics of a semiconductor laser as a function of the frequency offset between the locking and free-running laser fields and the injection parameter, ξ. The thick solid line is the boundary of the injection-locked region. The low-frequency locking boundary is a constant phase line, $\phi_L = -\arctan b^{-1}$, and the high-frequency boundary is the line where $\phi_L = \pi/2$ and the relative circulating field amplitude is $a_L = 1$. Also shown in the interior of the locking region is the Hopf bifurcation line (thick dashed line) separating the stable and unstable operating regimes and the lines of constant amplitude at $a_L = 1.1$ (dotted line), $a_L = 1.5$ (dot-dashed line), and $a_L = 2$ (double dot-dashed line).

14

Figure 3(a). Frequency offsets.
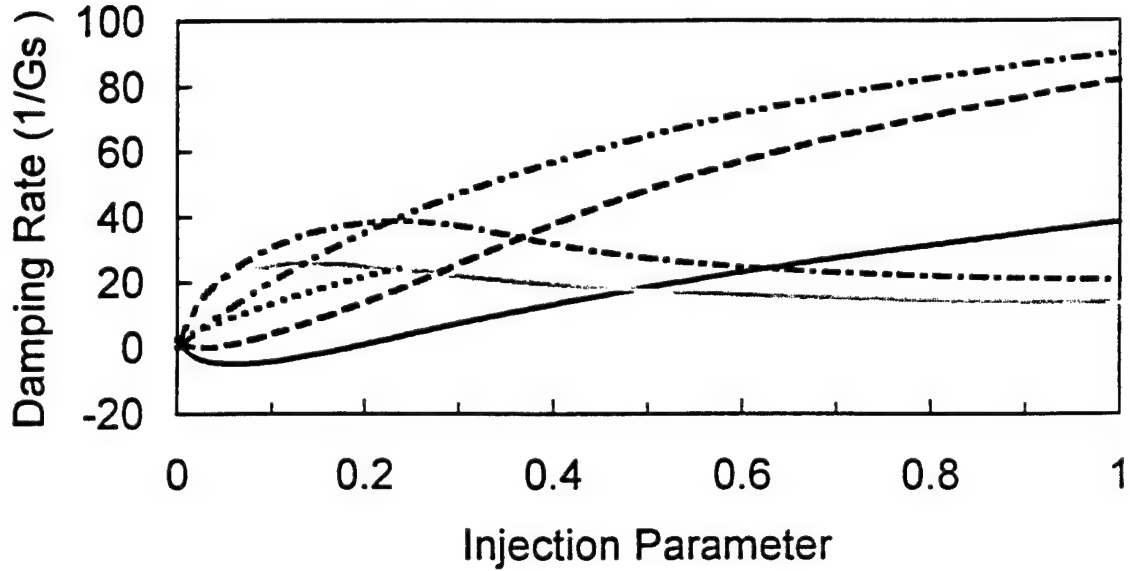
Figure 3(b). Damping rates.

Figure 3: Frequency offsets and damping rates as a function of the injection parameter, ξ, along lines of constant phase. In (a), the frequency offset of the locking frequency and eigenfrequency of the non-zero frequency resonance are shown: $\phi_L = 0$ offset (double dot-dashed line) and eigenfrequency (dotted line), $\phi_L = 0.67$ offset (dot-dashed line) and eigenfrequency (dashed line), and $\phi_L = \arctan b$ offset (light solid line) and eigenfrequency (dark solid line). In (b), the damping rates for the eigenfrequencies are shown: $\phi_L = 0$ zero (double dot-dashed line) and non-zero (dotted line) eigenfrequency damping rate, $\phi_L = 0.67$ zero (dot-dashed line) and non-zero (dashed line), and $\phi_L = \arctan b$ zero (light solid line) and non-zero (dark solid line).

15

above threshold and is subjected to a strong injection field, so that $a_L^{-1} \approx 0$, then:

$$U \approx \frac{\gamma_c \gamma_{nL}}{2(\gamma_s + \gamma_{nL})}, \tag{19}$$

$$V \approx \omega_L - \omega_0 + b\frac{\gamma_c \gamma_{nL}}{2(\gamma_s + \gamma_{nL})}, \tag{20}$$

$$\phi_L \approx \arctan\left[\frac{2(\gamma_s + \gamma_{nL})(\omega_L - \omega_0) + b\gamma_c \gamma_{nL}}{\gamma_c \gamma_{nL}}\right]. \tag{21}$$

We will use these relations to connect our results on the modulation characteristics of laser oscillators with the results of optical modulation in semiconductor travelling-wave amplifiers.

All modelling in the following sections is derived from this basic model, these definitions, and the assumption that both the modulation field and the modulation current can be modeled perturbatively through a linearization of the coupled equations about the operating point. Here, we conclude by noting that the weak external optical probe and the modulation current are assumed to be independent sources which perturb the operating point. In the linearized analysis this leads to independent contributions to the spectra from uncorrelated sources.

2.1.2 Linearized Analysis

With these relations we can recast the coupled equations into a form which emphasizes the different dynamic parameters. The full nonlinear equations have been used to describe the chaotic dynamics of a semiconductor laser under optical injection [7]. We perform a perturbation analysis of the effects of the weak optical probe and the current modulation by assuming that the normalized field magnitude, $a = |A|/|A_L| - 1$, the phase variation about ϕ_L, $\tilde{\phi}$, and the normalized carrier density, $\tilde{n} = N/N_L - 1$, are all much less than unity. The coupled equations are then linearized as:

$$\frac{da}{dt} = -(U + \gamma_{pL})a - V\tilde{\phi} + \frac{(\gamma_c - 2U)\gamma_{nL}}{2\gamma_s \tilde{J}_L}\tilde{n} + \eta a_i \cos \Omega t, \tag{22}$$

$$\frac{d\tilde{\phi}}{dt} = (V + b\gamma_{pL})a - U\tilde{\phi} - b\frac{(\gamma_c - 2U)\gamma_{nL}}{2\gamma_s \tilde{J}_L}\tilde{n} - \eta a_i \sin \Omega t, \tag{23}$$

16

$$\frac{d\tilde{n}}{dt} = 2\gamma_s \tilde{J}_m \cos \Omega t - 2\gamma_s \tilde{J}_L (1 - \frac{\gamma_{pL}}{\gamma_c - 2U})a - (\gamma_s + \gamma_{nL})\tilde{n}. \tag{24}$$

Here, $\tilde{J}_m = J_m/2ed\gamma_s N_L$ is the normalized modulation current magnitude and we have assumed that $a_i = (A_i/A_L)e^{-i\phi_L}$ is a real quantity so that we do not have to retain an extraneous phase factor through the calculation.

Considerable insight about the modifications in laser characteristics can be obtained by performing an eigenvalue, or stability, analysis, of the coupled equations without the perturbing modulation and noise terms. The resonance frequency and bandwidth can be approximated by finding the complex eigenvalues of the coupled equations [7]. For the free-running laser, the eigenvalues are determined by the equation:

$$-i\Omega(-\Omega^2 + \Omega_r^2 - i\Omega\gamma_r) = 0, \tag{25}$$

where $\gamma_r = \gamma_s + \gamma_n + \gamma_p$ is the field-enhanced decay rate. There are two non-zero eigenfrequencies given by $\pm(\Omega_r^2 - \gamma_r^2/4)^{1/2}$, each with an associated damping of $\gamma_r/2$. The third eigenfrequency of the free-running laser is zero, with zero damping, an unphysical result that arises from the linearization procedure's handling of the phase diffusion of the oscillating field. Retaining the full nonlinearity of the coupled equations yields the proper damping behavior.

The injected field modifies the eigenfrequencies and damping, as given by the zeros of the determinant,

$$D = (-i\Omega + U)[-\Omega^2 + \Omega_L^2 + (\gamma_s + \gamma_{nL})U - i\Omega\gamma_{rL}]$$

$$+(\Omega_L^2 - i\Omega\gamma_{pL})bV + (-i\Omega + \gamma_s + \gamma_{nL})V^2, \tag{26}$$

where $\gamma_{rL} = \gamma_s + \gamma_{nL} + \gamma_{pL} + U$. For the injection-locked laser, the zero offset eigenfrequency is now with respect to the locking optical frequency, not the free-running frequency, and has positive damping. The non-zero eigenfrequencies, and associated damping, are also modified. In all cases the modifications follow a complex dependence on the strength of the locking field

and the detuning beteen the master and slave lasers. The eigenvalue solution is relatively simple for the case where $\phi_L = 0$. In this case, $V = 0$ and the zero frequency eigenvalue has an associated damping of U. The relaxation resonance frequency is now modified so that

$$\Omega^2_{rL} = \gamma_c \gamma_{nL} + \gamma_s \gamma_{pL} + (\gamma_s - \gamma_{nL})U \tag{27}$$

and the field-enhanced decay rate is now γ_{rL}. The non-zero eigenfrequencies and associated damping follow with the obvious substitutions into the free-running formulas.

The damping associated with the non-zero eigenfrequencies can become negative, indicating that a Hopf bifurcation to unstable dynamics has occured. The condition for the occurance of a Hopf bifurcation is the solution of Equation 26 with a real non-zero eigenfrequency. By separately setting the resulting real and imaginary parts of Equation 26 equal to zero, this requires that:

$$(\gamma_{rL} - bV)\Omega^2_L + (\gamma_{rL} + U)[\gamma_{rL}U + V(b\gamma_{pL} + V)] + (\gamma_s + \gamma_{nL})(\gamma_{rL}U - V^2) = 0. \tag{28}$$

Depending upon the detuning between the master and slave oscillators, and the operating point of the slave laser, Equation 28 will be satisfied for zero, one or two injection field levels.

Figure 2 shows the line denoting the Hopf bifurcation in the detuning versus injection-parameter plane. At relatively low injection levels, $0.01 < \xi < 0.1$, the region of instability occupies a sizeable fraction of the injection-locked range. At higher injection levels, the Hopf bifurcation line asymptotically approaches the $\phi_L = \pi/2$, $a_L = 1$ boundary, and most of the injection-locked range has stable dynamics. For this laser at this operating point, stability is assured when $a_L > 1.1$. Increasing the value of b relatively expands the unstable operating range while increasing $\tilde{J}$ reduces it.

To give some insight into these solutions, we can make some approximations to simplify the formula. If $\gamma_r \ll \Omega_r$, as is often the case in operating semiconductor lasers, and U and V are

of the same order as γ_r, then $A_L \approx A_0$ and Equation 28 will have a solution when $bV - U \approx \gamma_r$. At this bifurcation, there will be a resonant frequency, Ω_{HB1}, of $\Omega_{HB1} \approx \Omega_r$. At high injection levels, the laser will undergo a reverse Hopf bifurcation back to stable operating conditions. This occurs when $2U(U^2 + V^2)/(bV - U) \approx \Omega_r^2$, assuming that $|A_L| \approx |A_0|$, and the resonant frequency, Ω_{HB2}, now satisfies $\Omega_{HB2}^2 \approx \Omega_r^2 + U^2 + V^2$. From these simplified formulas, it follows that when $\phi_L < \arctan b^{-1}$, the laser remains injection locked with stable operating characteristics. Numerically, for the laser under study we find that the range of dynamic instability is bounded by $\phi_L \approx 0.67 > \arctan b^{-1}$. Injection at the free-running frequency, where the phase offset is $\phi_L = \arctan b$, induces strong modifications in both the frequency and damping with increasing injection strength. The first Hopf bifurcation point occurs when $\eta|A_l|/|A_0| \approx b\gamma_r/(b^2 - 1)$ and the reverse bifurcation when $\eta|A_l|/|A_0| \approx \sqrt{(b^2 - 1)/2}\Omega_r$. Further,

$$\Omega_{HB2} \approx \sqrt{\frac{b^2 + 1}{b^2 - 1}} \eta \frac{|A_l|}{|A_0|} \tag{29}$$

showing that for strong injection fields the eigenvalue solution is proportional to the injection field. If the semiconductor laser has a free-running bias point such that $\gamma_r/\Omega_r > b^2/\sqrt{2}$, then an injection field can destabilize the dynamics in only a relatively narrow range near the $\phi_L = \pi/2$ boundary. Because of the relations between Ω_r and γ_r, this operating point usually demands that $\gamma_n > \gamma_c$. In practice, this requires the use of an external cavity, where the assumption of single-mode operation of this analysis is generally more difficult to justify.

Figure 3(a) plots the non-zero positive eigenfrequency and the associated frequency offset, $\nu_L - \nu_0$, of the master laser with respect to the free-running slave laser as a function of ξ along the constant phase lines $\phi_L = 0$, 0.67 and $\arctan b$. Along the $\phi_L = 0$ line, the non-zero eigenfrequency vanishes for $\xi > 0.24$, indicating a transition from underdamped to overdamped dynamics. Damping rates associated with the non-zero eigenfrequencies and the injection-locked oscillation frequency are shown in Figure 3(b). Negative damping indicates unstable dynamics. The $\phi_L = 0.67$ line approximately bounds the unstable region. When $\phi_L = 0$ and the dynamics are underdamped, the damping at the locking frequency is U.

Figure 4 shows similar plots at constant values of ξ as the injection-locked phase of the field is varied. Again, the non-zero eigenfrequency and the master-slave frequency offset are shown in Figure 4(a) and the associated damping rates in Figure 4(b). Note the zero crossing of the offset at $\phi_L = \arctan b$. At high injection levels, the damping remains positive over essentially the entire injection-locking range. Also, though the non-zero eigenfrequency is smaller than the free-running value for a range of ϕ_L, it vanishes only very close to $\phi_L = 0$ at the higher injection levels. The shift to true overdamped operation occurs for only a very narrow range of offset frequency and injection level.

When the free-running laser is biased close to threshold, then U and V can dominate the other dynamic rates, except γ_c at high, but accessible, injection powers. Using Equations 19 to 21, and considering injection at the free-running frequency, ω_0, the damping rate associated with the injection-locked oscillation frequency is approximately $3\gamma_s + \gamma_{nL}$. Note the similarity to the field-enhanced carrier decay rate, $\gamma_s + \gamma_{nL}$. The non-zero eigenfrequency is approximately V, with an associated damping rate of U. Both U and V depend on the ratio $\gamma_c\gamma_{nL}/[2(\gamma_s + \gamma_{nL})]$ in this limiting case.

When the optical and current modulation sources are added, the spectral characteristics are determined by the Fourier Transform of Equations 22 to 24.

$$\mathcal{F}(a) = \frac{(-i\Omega + \gamma_s + \gamma_{nL})[-i(\Omega - V) + U]}{D}\frac{\eta|A_i|}{2|A_L|} + c.c.$$

$$+\frac{(-i\Omega + U + bV)(\gamma_c - 2U)}{D}\frac{\gamma_{nL}\tilde{J}_m}{2\tilde{J}_L} + c.c., \tag{30}$$

$$\mathcal{F}(\tilde{\phi}) = \frac{1}{D}\{(-i\Omega + \gamma_s + \gamma_{nL})[-(\Omega - V - b\gamma_{pL}) - i(U + \gamma_{pL})]$$

$$+(b - i)(\gamma_c - 2U - \gamma_{pL})\gamma_{nL}\}\frac{\eta|A_i|}{2|A_L|} + c.c.$$

$$+\frac{1}{D}(ib\Omega - bU + V)(\gamma_c - 2U)\frac{\gamma_{nL}\tilde{J}_m}{2\tilde{J}_L} + c.c., \tag{31}$$

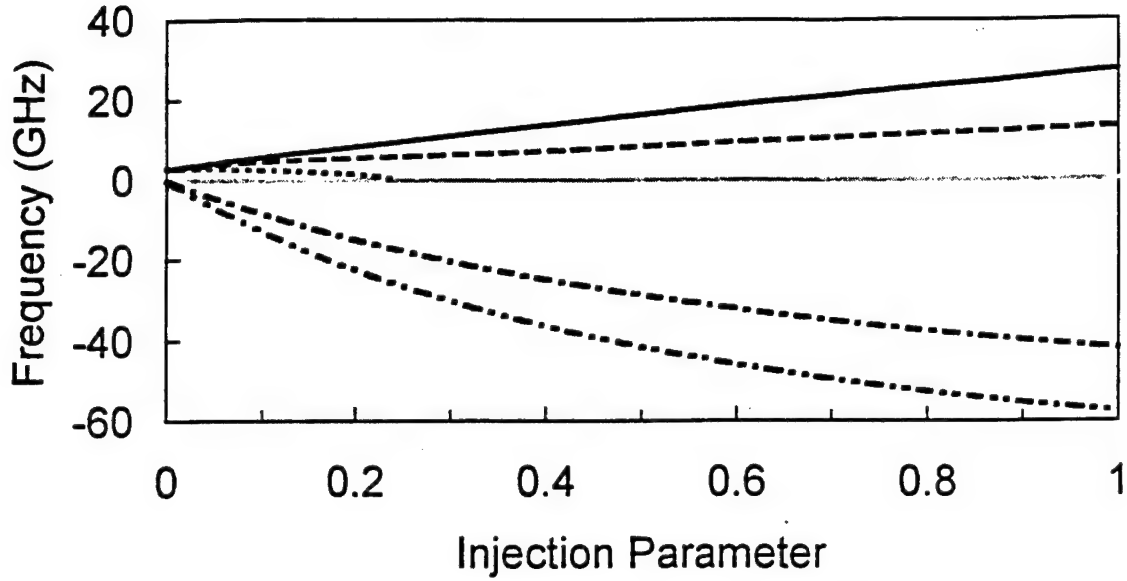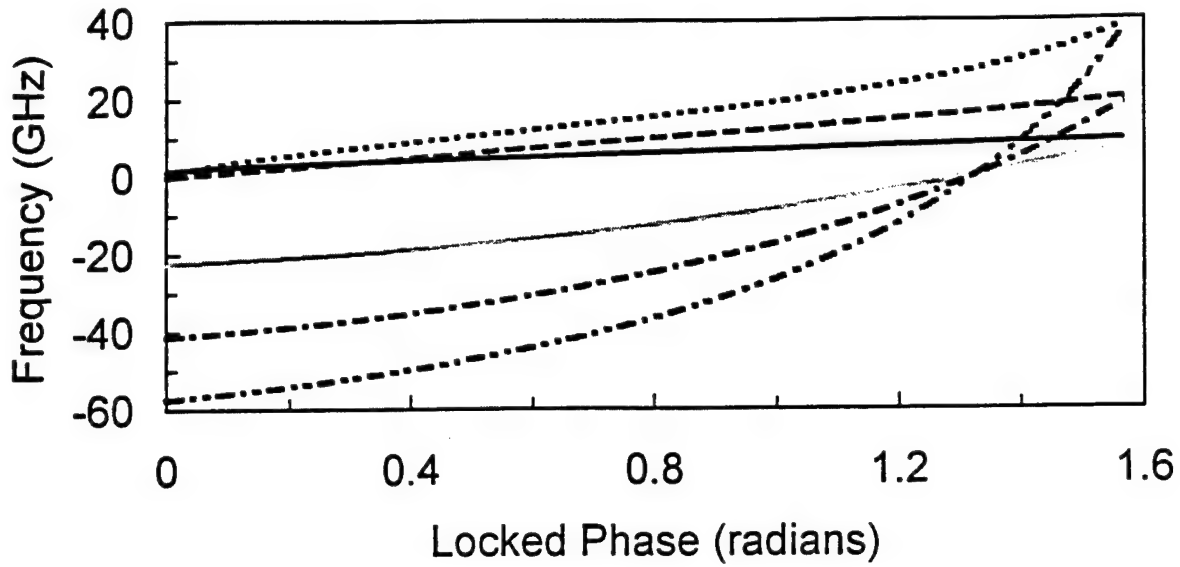**Figure 4(a). Frequency offsets.**
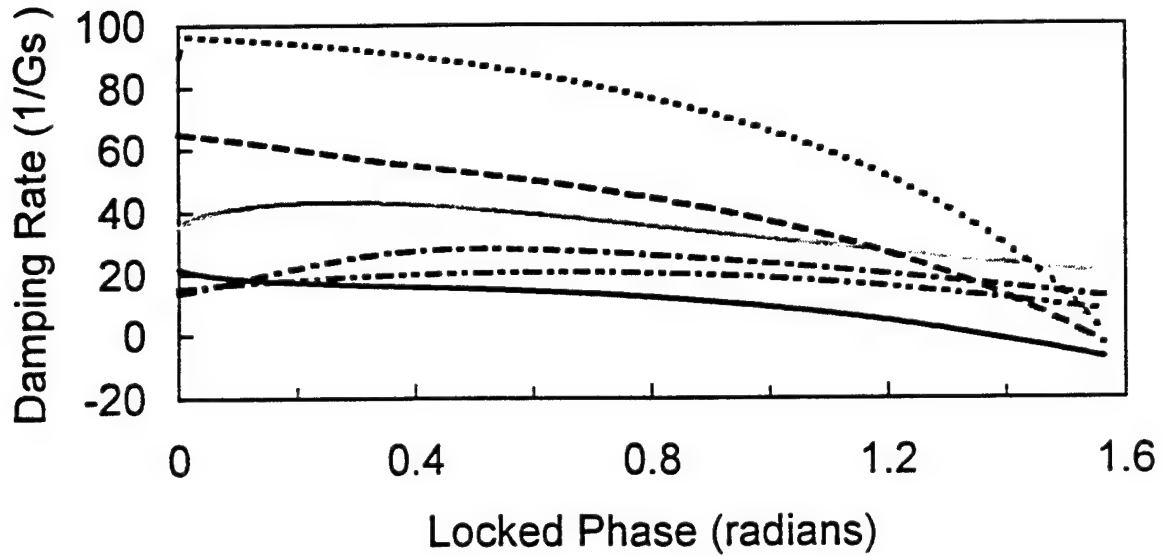
Figure 4(b). Damping rates.

Figure 4: Frequency offsets and damping rates as a function of the locked phase, ϕ_L, for constant values of the injection parameter. In (a), the frequency offset of the locking frequency and eigenfrequency of the non-zero frequency resonance are shown: $\xi = 1.0$ offset (double dot-dashed line) and eigenfrequency (dotted line), $\xi = 0.5$ offset (dot-dashed line) and eigenfrequency (dashed line), and $\xi = 0.2$ offset (light solid line) and eigenfrequency (dark solid line). In (b), the damping rates for the eigenfrequencies are shown: $\xi = 1.0$ zero (double dot-dashed line) and non-zero (dotted line) eigenfrequency damping rate, $\xi = 0.5$ zero (dot-dashed line) and non-zero (dashed line), and $\xi = 0.2$ zero (light solid line) and non-zero (dark solid line).

21

$$\mathcal{F}(\tilde{n}) = [(-i\Omega + U)(-i\Omega + U + \gamma_{pL}) + V(V + b\gamma_{pL})]\frac{\gamma_s \tilde{J}_m}{D} + c.c.$$

$$-(\gamma_c - 2U - \gamma_{pL})[-i(\Omega - V) + U]\frac{\eta|A_i|}{D|A_L|} + c.c. \tag{32}$$

Here, $\mathcal{F}(x)$ is the Fourier Transform of x, D is the determinant given by Equation 26 and $c.c.$ is the complex conjugate which corresponds to a frequency component equally and oppositely shifted with respect to ω_L for the optical frequency spectra, and with respect to zero for the carrier density and optical power spectra.

For optical modulation, the linearized analysis predicts that the output field of the injection-locked laser consists of spectral components at the locked oscillating frequency, ω_L, the injection frequency, $\omega_L + \Omega$, and the four-wave mixing parametric frequency, $\omega_L - \Omega$. From the view point of regenerative amplification and four-wave mixing, it can be mathematically described by

$$E(t) = A(t)e^{-i\omega_L t} + c.c. \tag{33}$$

with

$$A(t) = A_L + A_r e^{-i\Omega t} + A_f e^{i\Omega t}, \tag{34}$$

where A_r and A_f are the complex amplitudes of the regeneratively amplified and four-wave mixing fields, respectively. Alternatively, it can be described by

$$E(t) = E_L[1 + \sigma\cos(\Omega t - \varphi_1)]\cos[\omega_L t + \delta\cos(\Omega t - \varphi_2)], \tag{35}$$

as a field undergoing both amplitude and phase modulations, where

$$\hat{\sigma} = \sigma e^{i\varphi_1} \quad \text{and} \quad \hat{\delta} = \delta e^{i\varphi_2} \tag{36}$$

22

are the complex amplitudes of the amplitude and phase modulations, respectively. The two pictures are connected through

$$\hat{\sigma} = \frac{A_r A_L^* + A_f^* A_L}{|A_L|^2} \quad \text{and} \quad \hat{\delta} = i\frac{A_r A_L^* - A_f^* A_L}{|A_L|^2} \tag{37}$$

or

$$\frac{A_r}{A_L} = \frac{\hat{\sigma} - i\hat{\delta}}{2} \quad \text{and} \quad \frac{A_f^*}{A_L^*} = \frac{\hat{\sigma} + i\hat{\delta}}{2}. \tag{38}$$

Thus both A_r and A_f have contributions from both the amplitude and phase modulations of the laser field. The situation is similar for the case of current modulation, where A_r can be replaced by A_p and A_f by A_n to represent the positive and negative frequency components of the sinusoidal modulation, and the same formalism can be used.

As is the case with the free-running laser, the key component of the four-wave mixing process is the carrier pulsation in the semiconductor gain medium caused by the beating between the mixing optical fields. In a single-mode semiconductor laser, the spatial gratings are not important and the process is solely contributed by the temporal pulsation of the carrier density at the beat frequency [25, 23]. In the linearized analysis, the carrier density can be expressed as

$$N(t) = N_L + N_1 e^{-i\Omega t} + N_1^* e^{i\Omega t}, \tag{39}$$

where N_1 is the amplitude of the carrier pulsation.

To reveal the physical mechanisms involved in the process, we first use Equations 35 and 39 with Equations 30 to 32 to obtain

$$N_1 = -\frac{\gamma_c - 2U - \gamma_p}{\gamma_s + \gamma_{nL} - i\Omega}\frac{S_L}{\Gamma}\hat{\sigma}. \tag{40}$$

23

Clearly, this indicates that the carrier pulsation is caused by the amplitude fluctuation of the total optical field in the laser cavity. When $\Omega \to 0$, N_1 and $\hat{\sigma}$ are out of phase by π. This means that the induced carrier pulsation acts to reduce the amplitude fluctuation in the laser field caused by the optical modulation.

Using Equations 34 and 40 with Equations 30 to 32, we have

$$\frac{A_r}{A_L} = \frac{i}{\Omega + V + iU} \left(\frac{1 - ib}{2} \frac{\Omega_L^2 - i\Omega\gamma_{pL}}{\gamma_c - 2U - \gamma_{pL}} \frac{\Gamma N_1}{S_L} + \frac{\eta A_i}{A_L} \right), \tag{41}$$

$$\frac{A_f^*}{A_L^*} = \frac{i}{\Omega - V + iU} \left(\frac{1 + ib}{2} \frac{\Omega_L^2 - i\Omega\gamma_{pL}}{\gamma_c - 2U - \gamma_{pL}} \frac{\Gamma N_1}{S_L} \right). \tag{42}$$

From Equation 37, we further obtain

$$\hat{\sigma} = \frac{i(\Omega - V) - U}{\Omega^2 - (U^2 + V^2) + 2iU\Omega} \left[\frac{(\Omega + iU + ibV)(\Omega_L^2 - i\Omega\gamma_{pL})}{(\Omega - V + iU)(\gamma_c - 2U - \gamma_{pL})} \frac{\Gamma N_1}{S_L} + \frac{\eta A_i}{A_L} \right], \tag{43}$$

$$\hat{\delta} = \frac{i(\Omega - V) - U}{\Omega^2 - (U^2 + V^2) + 2iU\Omega} \left[\frac{(b\Omega + ibU - iV)(\Omega_L^2 - i\Omega\gamma_{pL})}{(\Omega - V + iU)(\gamma_c - 2U - \gamma_{pL})} \frac{\Gamma N_1}{S_L} + i\frac{\eta A_i}{A_L} \right]. \tag{44}$$

These relations show the various physical components of contribution to the regeneratively amplified and four-wave mixing signals, as well as those to the amplitude and phase modulations of the field. The factor

$$G(\Omega) = \frac{\Omega_L^2 - i\Omega\gamma_{pL}}{\gamma_c - 2U - \gamma_{pL}} \frac{\Gamma N_1}{S_L} \tag{45}$$

appears in all four relations. It is the gain caused by the carrier pulsation. This can be easily seen from the fact that when the nonlinear gain coefficient is negligible so that $\gamma_p = 0$, $G = g_n N_1$. In a semiconductor medium in general, and a free-running laser in particular, a change of gain by G is always accompanied by a change of refractive index by bG. Thus an amplification of the amplitude modulation by G is accompanied by an amplification of the phase modulation by bG. This is seen in Equations 43 and 44 when $U = V = 0$ and, more clearly in Reference [13]. Under injection locking, the quadrature injection term, V, changes the amplitude and phase coupling characteristics among the carriers, the circulating optical field and the injected optical field.

Both amplitude and phase modulations also have contributions from the externally injected field. In contrast, the externally injected field directly contributes only to the regeneratively amplified signal at the same frequency, but not to the four-wave mixing signal at a different frequency. It is only through the carrier pulsation that the external modulation field induces the four-wave mixing signal. This is seen by using Equations 32 and 39 to obtain

$$N_1 = \frac{(\gamma_c - 2U - \gamma_{pL})[U - i(\Omega - V)]}{D} \frac{S_L}{\Gamma} \frac{\eta A_i}{A_L}. \tag{46}$$

In the free-running laser, the modulation on the laser field at ω_0 by the gain fluctuation G and the accompanying refractive-index fluctuation bG at Ω generates sidebands at $\omega_0 + \Omega$ and $\omega_0 - \Omega$ with equal efficiency although different phases. Thus the regeneratively amplified signal and the four-wave mixing signal both have contributions from G and bG with equal magnitude but different phases. This is no longer true in the injection-locked laser due to the different resonant denominators in Equations 41 and 42. The resonant denominator for the four-wave mixing sideband is cancelled by a similar term in the numerator of Equation 46. There is no such cancellation in the regeneratively amplified sideband so that it will contain a resonance term at negative offset frequencies and a quenching term at positive offset frequencies.

The connection between optical modulation and carrier pulsation is direct in the case of current modulation of the carrier density. Now, from Equations 32 and 39, we have

$$N_1 = \frac{(-i\Omega + U)(i\Omega + U + \gamma_{pL}) + V(V + b\gamma_{pL})}{D} \frac{J_m}{2ed}. \tag{47}$$

The solutions for the positive and negative optical frequency components, A_p and A_n, respectively, can be obtained in the same way as A_r and A_f:

$$\frac{A_p}{A_L} = \frac{i + b}{2} \frac{(-\Omega + V - iU)\gamma_{nL}}{(-i\Omega + U)(-i\Omega + U + \gamma_{pL}) + V(V + b\gamma_{pL})} \frac{\Gamma N_1}{S_L}, \tag{48}$$

$$\frac{A_n^*}{A_L^*} = \frac{-i + b}{2} \frac{(\Omega + V - iU)\gamma_{nL}}{(-i\Omega + U)(-i\Omega + U + \gamma_{pL}) + V(V + b\gamma_{pL})} \frac{\Gamma N_1}{S_L}. \tag{49}$$

Similarly, we can obtain the solutions for the amplitude and phase modulation coefficients:

$$\hat{\sigma} = \frac{(-i\Omega + U + bV)\gamma_{nL}}{(-i\Omega + U)(-i\Omega + U + \gamma_{pL}) + V(V + b\gamma_{pL})} \frac{\Gamma N_1}{S_L}, \quad (50)$$

$$\hat{\delta} = \frac{(-ib\Omega + bU + V)\gamma_{nL}}{(-i\Omega + U)(-i\Omega + U + \gamma_{pL}) + V(V + b\gamma_{pL})} \frac{\Gamma N_1}{S_L}. \quad (51)$$

In Equations 48 to 51 the combination of parameters $\gamma_{nL}\Gamma N_1/S_L = g_n N_1$ is common and is the gain due to the carrier pulsation. Because the current modulates the carrier density directly, the gain term here is simpler than G derived for the case of optical modulation. As was the case with optical modulation, the quadrature injection-locking term, V, removes the simple ratio of b between the phase and amplitude modulations that exist in the case of the free-running laser.

2.1.3 Modulation Spectra

The spectral characterization of semiconductor lasers uses a variety of techniques. Techniques which use a narrowband optical filter, such as an optical spectrum analyzer or an optical heterodyne configuration, can be used to map out the squared amplitude of the modulation sidebands, $|A_r|^2$, $|A_f|^2$, $|A_p|^2$ and $|A_n|^2$. The sidebands contain differing combinations of the amplitude and phase modulation characteristics. Spectral techniques which analyze the spectrum of the signal generated by a fast photodiode when illuminated by the semiconductor laser contain only information about the amplitude modulation characteristics. When the detected signal from a fast photodiode is fed into an RF/microwave spectrum analyzer, the spectrum of the amplitude modulation coefficient, $|\hat{\sigma}|^2$, can be measured. The spectra of other quantities of potential interest, such as $|\hat{\delta}|^2$ and $|N_1|^2$, can be determined from measurements of the optical sidebands and the amplitude modulation coefficient.

Here, we present representative spectra for optical and current modulation of an injection-locked laser operating in the region of stable dynamics. The operating parameters of the laser are listed in Table 1 and $\tilde{J} = 2/3$ for these calculations. Comparisons will be made for two cases. First, the master laser has the same optical frequency as the free-running slave laser,

26

corresponding to $\phi_L = \arctan b$, and ξ is varied: 0.005, 0.2, 0.5 and 1.0. The first two values of ξ roughly bracket the region of unstable operation. Second, $\xi = 0.2$ and ϕ_L is varied: 0, 0.67 and $\arctan b$. At this injection strength, when $\phi_L = 0$ there is a frequency offset of -22.4 GHz between the locked and free-running oscillation frequencies. For $\phi_L = 0.67$ the offset is -14.9 GHz, and for $\phi_L = \arctan b$ the offset is 0. Also shown in this series are the spectra for the free-running laser. Note that the $\xi = 0.2$, $\phi_L = \arctan b$ curves are common to both cases to assist in comparisons betweem them. Spectra of optical field modulation characteristics will use the free-running slave-laser frequency as the zero frequency reference for the calculated spectra that follow.

Regenerative amplification and four-wave mixing sidebands generated by weak optical modulation of an injection-locked semiconductor laser will have the following spectral characteristics:

$$\frac{|A_r|^2}{|A_i|^2} = \frac{\eta^2}{|D|^2}\{[-\Omega^2 + (V + b\gamma_{pL}/2)\Omega + \Omega_L^2/2 + (\gamma_s + \gamma_{nL})U]^2$$

$$+[-\Omega(\gamma_{rL} - \gamma_{pL}/2) + V(\gamma_s + \gamma_{nL}) + b\Omega_L^2/2]^2\} \tag{52}$$

$$\frac{|A_f|^2}{|A_i|^2} = \frac{\eta^2}{|D|^2}\frac{1+b^2}{4}(\Omega_L^4 + \Omega^2\gamma_{pL}^2) \tag{53}$$

The regenerative amplification sideband spectrum is asymmetric with respect to detuning about the injection-locked operating frequency. This asymmetry is extreme under a broad range of operating conditions, with a strong resonance at negative offset frequencies and a quenching at positive offset frequencies. The four-wave mixing sideband spectrum, on the other hand, is symmetric with relatively weaker resonances equally and oppositely offset from the injection-locked frequency. The pole at zero detuning for the free-running laser is removed under injection locking, though the spectral characteristics around zero will be obscured, to some degree, by the spectrum of the master laser. Away from zero detuning, the resonant carrier-field coupling may be destabilized, leading to oscillation at the negative, and sometimes the positive, eigenfrequency over a range of operating conditions. Equations 52 and 53 are certainly not a good description of experimentally observed spectra in the unstable operating regime. In that case the full nonlinear equations must be retained.

27

Figure 5 plots the regenerative amplification spectra for different values of ξ and ϕ_L; the signal value is $(\gamma_c|A_r|/2\eta|A_i|)^2$. The frequency axis is taken relative to the free-running operating point. A weak asymmetry in favor of negative offset frequencies in the free-running laser becomes quite strong as the injection level is increased.

Figure 6 plots the four-wave mixing spectra for different values of ξ and ϕ_L; the signal value is $(\gamma_c|A_f|/2\eta|A_i|)^2$. Again, the frequency axis is relative to the free-running operating point. The frequency-dependent term in the numerator is small compared to the $\gamma_c\gamma_{nL}$ term so that the shape of the spectrum is determined by the $|D|^2$ term in the denominator. Here, the three resonances, or eigenfrequencies, remain clearly developed in a symmetric spectrum when the injection is at the free-running frequency, Figure 6(a). When the injection is frequency offset, Figure 6(b), the increased damping obscures the resonances offset from the locking frequency.

The amplitude modulation spectrum is, in general, asymmetric about the injection-locked frequency:

$$|\hat{\sigma}|^2 = \left|\frac{\eta A_i}{A_L}\right|^2 \frac{[\Omega^2 + (\gamma_s + \gamma_{nL})^2][(\Omega - V)^2 + U^2]}{|D|^2} \tag{54}$$

Figure 7 plots the spectra for different values of ξ and ϕ_L; the signal value is $|\hat{\sigma}|^2(\gamma_c|A_0|/2\eta|A_i|)^2$. Only in the free-running and $\phi_L = 0$ cases are the amplitude modulation spectra symmetric. The importance of V in this asymmetry is clear in Equation 54. Also note the strong quenching of the amplitude modulations near the locking frequency. The spectral width of this quenching region is primarily determined by the field-enhanced carrier decay rate, $\gamma_s + \gamma_{nL}$.

Because $|A_p(-\Omega)|^2 = |A_n(\Omega)|^2$, the optical spectra of the current modulation characteristic are given by

$$\frac{|A_p|^2}{|A_L|^2} = \frac{1 + b^2}{4} \frac{[(\Omega - V)^2 + U^2](\gamma_c - 2U)^2\gamma_{nL}^2}{|D|^2} \frac{\tilde{J}_m^2}{\tilde{J}_L^2} \tag{55}$$

28
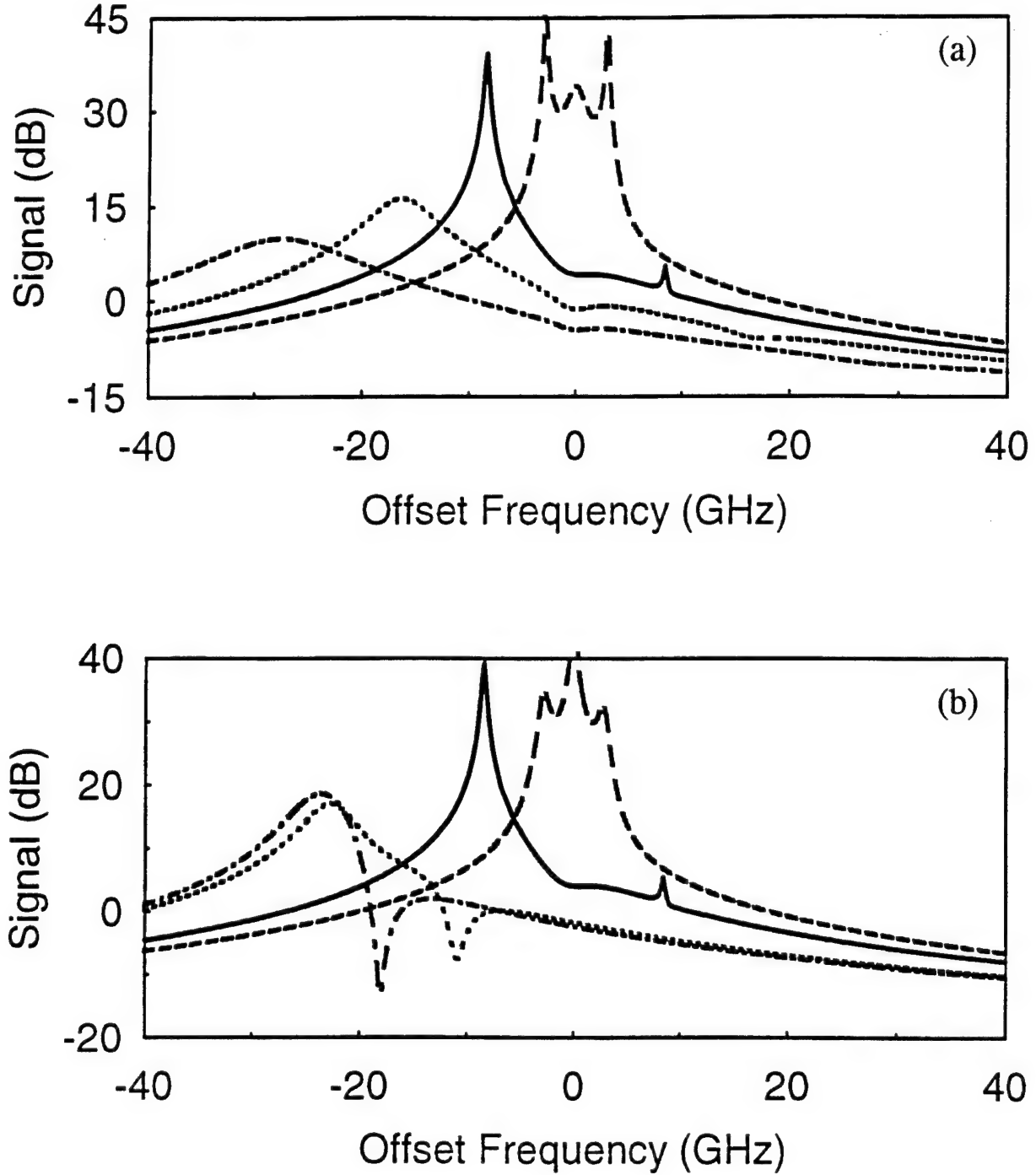
Figure 5: Spectrum of the regenerative amplification sideband characteristic due to a weak optical modulation, the signal value is $(\gamma_c |A_r|/2\eta|A_i|)^2$. The frequency offset is with respect to the free-running optical frequency. (a) Injection-locking field at the free-running optical frequency with $\xi = 0.005$ (dashed), $\xi = 0.2$ (solid), $\xi = 0.5$ (dotted), and $\xi = 1.0$ (dot-dashed). (b) Injection-locking field at $\xi = 0.0$ (dashed) and at $\xi = 0.2$ with $\dot{\phi}_L = 0.0$ (dot-dashed), $\dot{\phi}_L = 0.67$ (dotted), and $\dot{\phi}_L = \arctan b$ (solid).
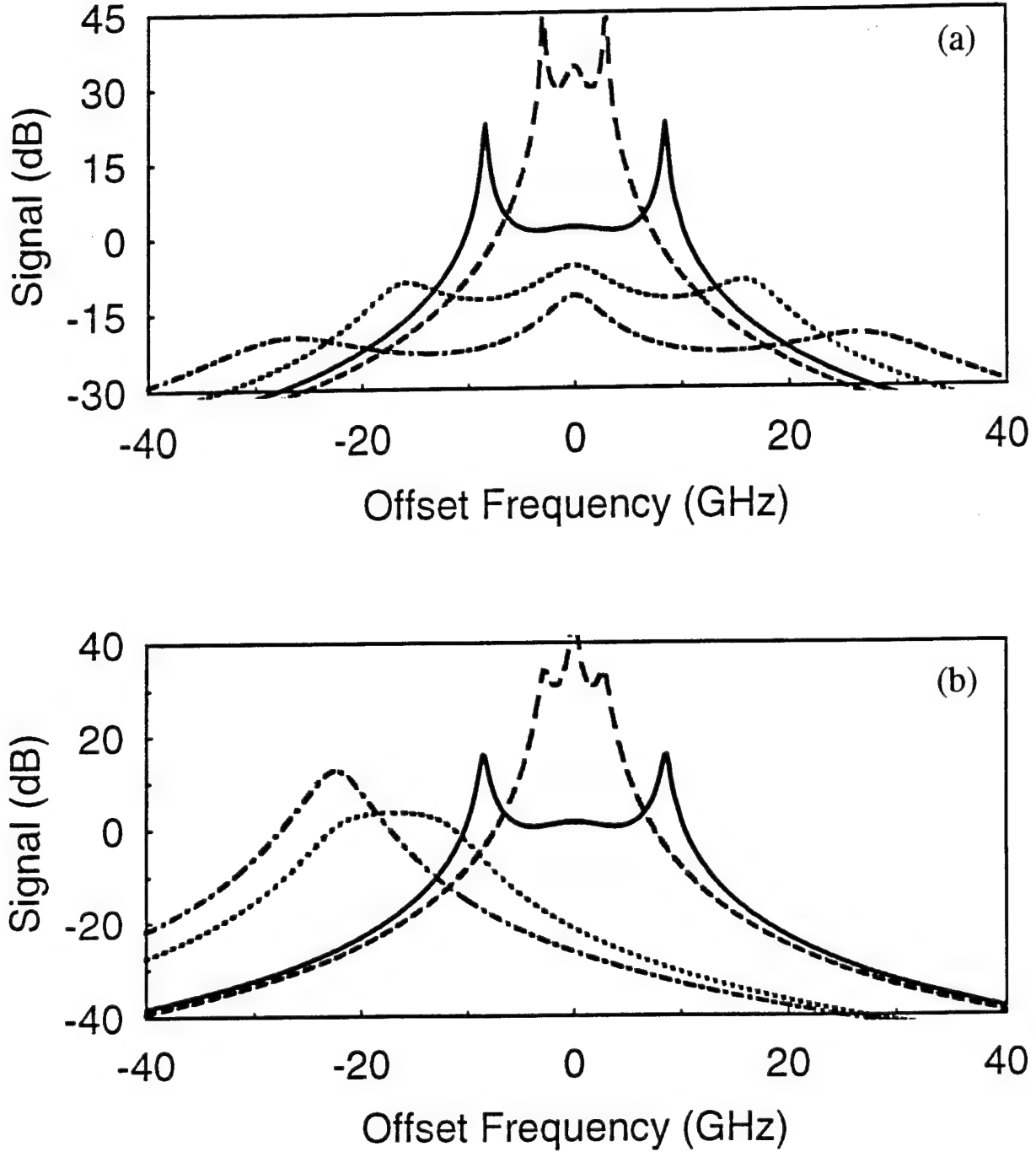
Figure 6: Spectrum of the four-wave mixing sideband characteristic due to a weak optical modulation. the signal value is $(\gamma_c |A_f|/2\eta|A_i|)^2$. The frequency offset is with respect to the free-running optical frequency. (a) Injection-locking field at the free-running optical frequency with $\xi = 0.005$ (dashed), $\xi = 0.2$ (solid), $\xi = 0.5$ (dotted), and $\xi = 1.0$ (dot-dashed). (b) Injection-locking field at $\xi = 0.0$ (dashed) and at $\xi = 0.2$ with $\phi_L = 0.0$ (dot-dashed), $\phi_L = 0.67$ (dotted), and $\phi_L = \arctan b$ (solid).

30
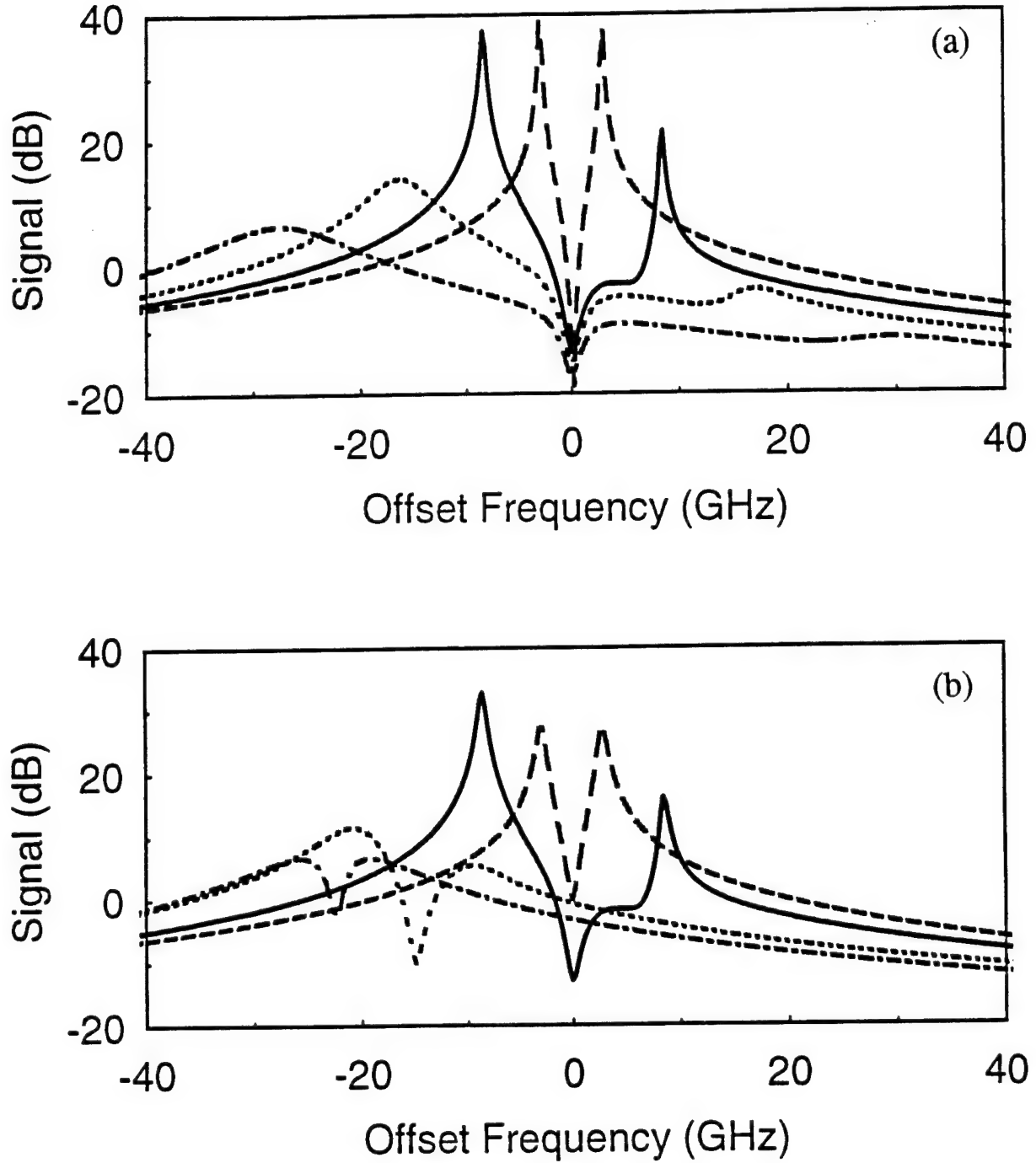
Figure 7: Spectrum of the amplitude modulation characteristic due to a weak optical modulation. The signal value is $|\hat{\sigma}|^2(\gamma_c|A_0|/2\eta|A_i|)^2$. (a) Injection-locking field at the free-running optical frequency with $\xi = 0.005$ (dashed), $\xi = 0.2$ (solid), $\xi = 0.5$ (dotted), and $\xi = 1.0$ (dot-dashed). (b) Injection-locking field at $\xi = 0.0$ (dashed) and at $\xi = 0.2$ with $\dot{\phi}_L = 0.0$ (dot-dashed), $\dot{\phi}_L = 0.67$ (dotted), and $\dot{\phi}_L = \arctan b$ (solid).

Except for the cases of the free-running and $\phi_L = 0$ operation, the spectra are asymmetric with respect to the oscillation frequency and, like the regenerative amplification spectra, have a stronger resonance at negative offset frequencies. Figure 8 plots the spectra for different values of ξ and ϕ_L; the signal value is $|A_p/A_L|^2/(J_m/2J)^2$. The frequency axis is relative to the free-running operating point. Injection locking breaks the spectral symmetry exhibited by the free-running spectrum. Like the regenerative amplification spectrum, the modulation is enhanced for negative offset frequencies.

The amplitude modulation spectra are symmetric with

$$|\hat{\sigma}|^2 = \frac{[\Omega^2 + (U + bV)^2](\gamma_c - 2U)^2\gamma_{nL}^2}{|D|^2}\frac{\tilde{J_m}^2}{\tilde{J_L}^2} \tag{56}$$

Figure 9 plots the amplitude modulation under current modulation for different values of ξ and ϕ_L; the signal value is $|\hat{\sigma}|^2/(J_m/2J)^2$. Only positive frequencies are shown because of the inherent spectral symmetry. Strong optical injection increases the non-zero resonance frequencies and quenches the resonances. In Figure 9(b) we see how either modulation bandwidth or flatness of response can be emphasized depending on the injection conditions. The bandwidth can be more than doubled by injection signals which are weak relative to the laser output.

2.2 LINEARIZED ANALYSIS INCLUDING FEEDBACK

Here, we augment the analysis described above by including the effects of optical feedback on the injection-locked operating characteristics. Optical feedback can be included in Equation 2 by adding a term $rA(t-\tau)$ where r is the coupling parameter for the strength of the feedback and τ is the round-trip time delay for the back-reflected output. It is well known that external feedback can induce nonlinear dynamics in a laser diode [27]. Therefore, this analysis will only be appropriate for feedback which is weak compared to the external optical injection and where the injection is not inducing an operating point close to the Hopf bifurcation

32
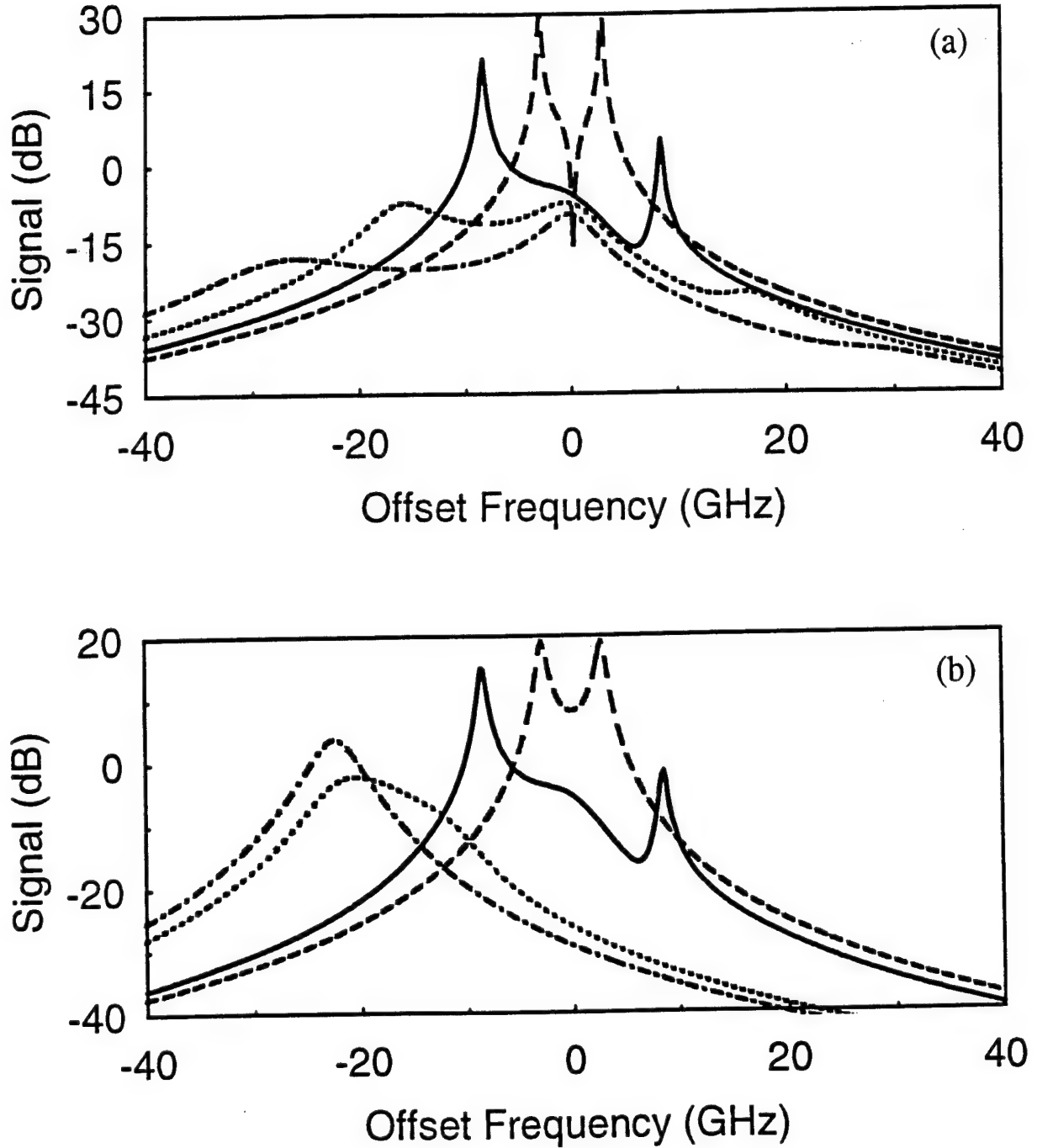
Figure 8: Spectrum of the optical field positive sideband characteristic due to a weak current modulation. The signal value is $|A_p/A_L|^2/(J_m/2J)^2$. The frequency offset is with respect to the free-running optical frequency. (a) Injection-locking field at the free-running optical frequency with $\xi = 0.005$ (dashed), $\xi = 0.2$ (solid), $\xi = 0.5$ (dotted), and $\xi = 1.0$ (dot-dashed). (b) Injection-locking field at $\xi = 0.0$ (dashed) and at $\xi = 0.2$ with $\phi_L = 0.0$ (dot-dashed), $\phi_L = 0.67$ (dotted), and $\phi_L = \arctan b$ (solid).
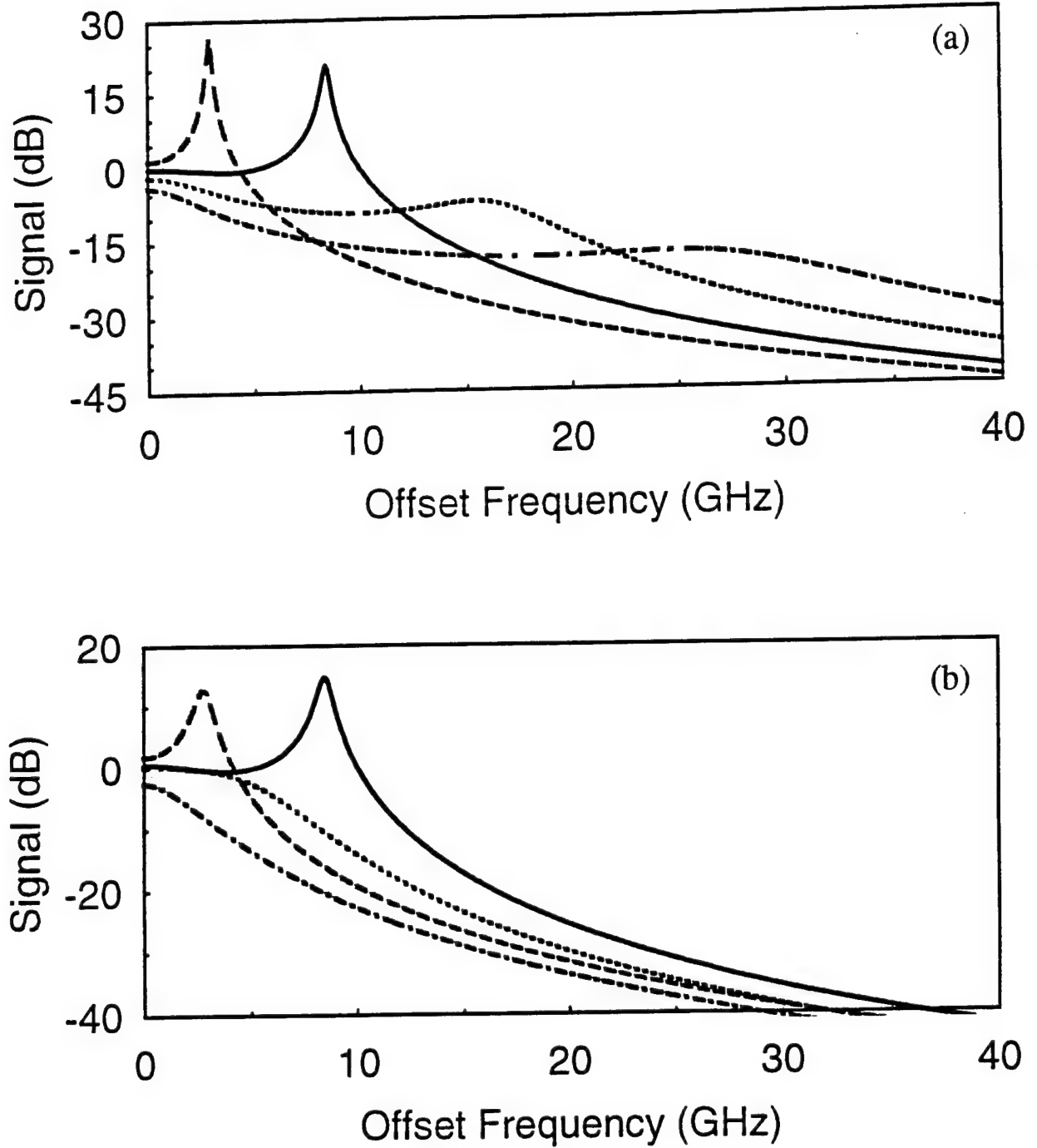
Figure 9: Spectrum of the amplitude modulation characteristic due to a weak current modulation. The signal value is $|\hat{\sigma}|^2/(J_m/2J)^2$. (a) Injection-locking field at the free-running optical frequency with $\xi = 0.005$ (dashed), $\xi = 0.2$ (solid), $\xi = 0.5$ (dotted), and $\xi = 1.0$ (dot-dashed). (b) Injection-locking field at $\xi = 0.0$ (dashed) and at $\xi = 0.2$ with $\phi_L = 0.0$ (dot-dashed), $\phi_L = 0.67$ (dotted), and $\phi_L = \arctan b$ (solid).

separating the regions of stable and unstable dyanmics. We proceed following the same line of analysis as used above. The notation will be kept as consistent as possible. The addition of the feedback further modifies the operating point of the laser so that now:

$$\omega_L - \omega_0 = -bU + V - br\cos(\omega_L\tau) + r\sin(\omega_L\tau). \tag{57}$$

Again, $U = \eta|A_l/A_L|\cos\phi_L$ is the in-phase injection term and $V = \eta|A_l/A_L|\sin\phi_L$ is the quadrature term. In the absence of feedback, the gain defect at the injection-locked operating point is $2U$ and the frequency offset, $\omega_L - \omega_c - b\Gamma g_L/2$, where g_L is the steady-state gain at the injection-locked operating point, is V, as described above. The feedback causes an additional shift such that the gain defect is now $2U + 2r\cos(\omega_L\tau) = 2U'$ and the locked phase is modified so that the frequency shift is now $V + \sin(\omega_L\tau) = V'$. The relation between $|A_L|$ and the free-running value, $|A_0|$, can be obtained through the cubic equation:

$$a_L^3 - Y'a_L^2 - a_L - Y'\frac{\gamma_s}{\gamma_n} = 0 \tag{58}$$

where $a_L = |A_L/A_0|$, the factor, Y', is given by:

$$Y' = 2\frac{\gamma_c\gamma_n}{\Omega_r^2}\left[\xi\cos(\phi_L) + \frac{r}{\gamma_c}\cos(\omega_L\tau)\right]. \tag{59}$$

The injected signal and feedback also modify the threshold for oscillation. The pump parameter of the locked oscillator is related to the free-running pump parameter by:

$$\tilde{J}'_L = \frac{(1 - 2U')a_L^2\tilde{J}}{1 - \gamma_s\tilde{J}[2U' - \gamma_p(a_L^2 - 1)/\gamma_c]/\gamma_n} \tag{60}$$

Alternatively, $|A_0|$ and $|A_L|$ are related through an equation based on the injection-locked parameters:

$$a_L^2 = \frac{\Omega_L^2 + 2U'\gamma_{nL}}{\Omega_L^2 - 2U'\gamma_s} \tag{61}$$

35

where, now, the factor $\Omega_L^2 = (\gamma_c - 2U')\gamma_{nL} + \gamma_s\gamma_{pL}$. The coupled equations, including weak feedback, are then linearized as:

$$\frac{da}{dt} = -(U' + \gamma_{pL})a + r\cos(\omega_L\tau)a(t - \tau) - V'\tilde{\phi} - r\sin(\omega_L\tau)\tilde{\phi}(t - \tau)$$

$$+\frac{(\gamma_c - 2U')\gamma_{nL}}{2\gamma_s\tilde{J}_L}\tilde{n} + \eta a_i\cos\Omega t, \tag{62}$$

$$\frac{d\tilde{\phi}}{dt} = (V' + b\gamma_{pL})a + r\sin(\omega_L\tau)a(t - \tau) - U'\tilde{\phi} + r\cos(\omega_L\tau)\tilde{\phi}(t - \tau)$$

$$-b\frac{(\gamma_c - 2U')\gamma_{nL}}{2\gamma_s\tilde{J}_L}\tilde{n} - \eta a_i\sin\Omega t, \tag{63}$$

$$\frac{d\tilde{n}}{dt} = 2\gamma_s\tilde{J}_m\cos\Omega t - 2\gamma_s\tilde{J}_L(1 - \frac{\gamma_{pL}}{\gamma_c - 2U'})a - (\gamma_s + \gamma_{nL})\tilde{n}. \tag{64}$$

Here, $\tilde{J}_m = J_m/2ed\gamma_s N_L$ is the normalized modulation current magnitude and we have assumed that $a_i = (A_i/A_L)e^{-i\phi_L}$ is a real quantity so that we do not have to retain an extraneous phase factor through the calculation, as before.

The spectral characteristics are determined by the Fourier Transform of Equations 62 to 64.

$$\mathcal{F}(a) = \frac{(-i\Omega + \gamma_s + \gamma_{nL})[-i(\Omega - V'') + U'']}{D}\frac{\eta|A_i|}{2|A_L|} + c.c.$$

$$+\frac{(-i\Omega + U'' + bV'')(\gamma_c - 2U')}{D}\frac{\gamma_{nL}\tilde{J}_m}{2\tilde{J}_L'} + c.c., \tag{65}$$

$$\mathcal{F}(\tilde{\phi}) = \frac{1}{D}\{(-i\Omega + \gamma_s + \gamma_{nL})[-(\Omega - V'' - b\gamma_{pL}) - i(U'' + \gamma_{pL})]$$

$$+(b - i)(\gamma_c - 2U' - \gamma_{pL})\gamma_{nL}\}\frac{\eta|A_i|}{2|A_L|} + c.c.$$

$$+\frac{1}{D}(ib\Omega - bU'' + V'')(\gamma_c - 2U')\frac{\gamma_{nL}\tilde{J}_m}{2\tilde{J}_L'} + c.c., \tag{66}$$

$$\mathcal{F}(\tilde{n}) = [(-i\Omega + U'')(-i\Omega + U'' + \gamma_{pL}) + V''(V'' + b\gamma_{pL})]\frac{\gamma_s\tilde{J}_m}{D} + c.c.$$

36

$$-(\gamma_c - 2U' - \gamma_{pL})[-i(\Omega - V'') + U'']\frac{\eta|A_i|}{D|A_L|} + c.c. \tag{67}$$

Here, $\mathcal{F}(x)$ is the Fourier Transform of x, $U'' = U' - e^{i\Omega t}r\cos(\omega_L\tau)$, $V'' = V' + e^{i\Omega t}r\sin(\omega_L\tau)$, D is the determinant given by:

$$
\begin{aligned}
D &= (-i\Omega + U'')[-\Omega^2 + \Omega_L^2 + (\gamma_s + \gamma_{nL})U'' - i\Omega\gamma_{rL}] \\
&\quad + (\Omega_L^2 - i\Omega\gamma_{pL})bV'' + (-i\Omega + \gamma_s + \gamma_{nL})V''^2,
\end{aligned} \tag{68}
$$

where $\gamma_{rL} = \gamma_s + \gamma_{nL} + \gamma_{pL} + U''$, and $c.c.$ is the complex conjugate which corresponds to a frequency component equally and oppositely shifted with respect to ω_L for the optical frequency spectra, and with respect to zero for the carrier density and optical power spectra. The equations above are given in the same format as was used above and in Reference [12]. and reduce to those equations when $r = 0$.

Regenerative amplification and four-wave mixing sidebands generated by weak optical modulation of an injection-locked semiconductor laser will have the following spectral characteristics:

$$
\begin{aligned}
\frac{|A_r|^2}{|A_i|^2} &= \frac{\eta^2}{|D|^2}\{[-\Omega^2 + (V'' + b\gamma_{pL}/2)\Omega + \Omega_L^2/2 + (\gamma_s + \gamma_{nL})U'']^2 \\
&\quad + [-\Omega(\gamma_{rL} - \gamma_{pL}/2) + V''(\gamma_s + \gamma_{nL}) + b\Omega_L^2/2]^2\}
\end{aligned} \tag{69}
$$

$$
\frac{|A_f|^2}{|A_i|^2} = \frac{\eta^2}{|D|^2}\frac{1 + b^2}{4}(\Omega_L''^4 + \Omega^2\gamma_{pL}^2) \tag{70}
$$

As before, the regenerative amplification sideband spectrum is asymmetric with respect to detuning about the injection-locked operating frequency. This asymmetry is extreme under a broad range of operating conditions, with a strong resonance at negative offset frequencies and a quenching at positive offset frequencies. The four-wave mixing sideband spectrum, on the other hand, remains symmetric with relatively weaker resonances equally and oppositely offset from the injection-locked frequency. The pole at zero detuning for the free-running laser is removed under injection locking, though the spectral characteristics around zero will be obscured, to some degree, by the spectrum of the master laser. Away from zero detuning, the resonant carrier-field coupling may be destabilized, leading to oscillation at

the negative, and sometimes the positive, eigenfrequency over a range of operating conditions. Equations 69 and 70 are certainly not a good description of experimentally observed spectra in the unstable operating regime. In that case the full nonlinear equations must be retained. The amplitude modulation spectrum is, in general, asymmetric about the injection-locked frequency:

$$|\hat{\sigma}|^2 = \left|\frac{\eta A_i}{A_L}\right|^2 \frac{[\Omega^2 + (\gamma_s + \gamma_{nL})^2][(\Omega - V'')^2 + U''^2]}{|D|^2} \tag{71}$$

The optical spectra of the current modulation characteristic are modified from the feedback-free case to:

$$\frac{|A_p|^2}{|A_L|^2} = \frac{1 + b^2}{4} \frac{[(\Omega - V'')^2 + U''^2](\gamma_c - 2U')^2\gamma_{nL}^2}{|D|^2} \frac{\tilde{J}_m^2}{\tilde{J}_L'^2} \tag{72}$$

As before, except for the cases of the free-running and $\phi_L = 0$ operation, the spectra are asymmetric with respect to the oscillation frequency and, like the regenerative amplification spectra, have a stronger resonance at negative offset frequencies. The amplitude modulation spectra are symmetric with

$$|\hat{\sigma}|^2 = \frac{[\Omega^2 + (U'' + bV'')^2](\gamma_c - 2U')^2\gamma_{nL}^2}{|D|^2} \frac{\tilde{J}_m^2}{\tilde{J}_L'^2}. \tag{73}$$

Again, the spectra revert to the formulas above and in Reference [12] when $r = 0$.

2.3 NUMERICAL SIMULATION OF INJECTION-LOCKED OPERATION

Because the coupled field and carrier density equations are nonlinear, in general, they must be solved numerically. Here, we describe the techniques used to solve the full nonlinear equations. By comparison of the numerical solutions of the full nonlinear equations with the analytical solutions of the linearized approximation, we can show where the linearization is

38

appropriate. Some care must be taken in the numerical integration of the coupled equations. Equation 2 is a stochastic nonlinear differential equation because it contains the stochastic noise source term as well as the deterministic external field source term. The numerical integration of differential equations is typically done using a Taylor-series type expansion [28]. One wants to determine the quantity $X(t + h)$, at the time $t + h$, knowing $X(t)$. The Taylor-series expansion parameter is h. There are several standard solution algorithms for solving deterministic differential equations. For example, the standard 4th order Runge-Kutta integrations scheme is available in commercial software packages such as Mathcad. It is called 4th order because the expansion is accurate to 4th order in the parameter h. However, it can, at best, only be made accurate to 1st order in h for a stochastic source [29]. Therefore, the stepsize, h, must be much smaller with a stochastic term in the equation than for a purely deterministic equation. Different algorithms are required for the numerical integration of stochastic differential equations with accuracy higher than first order in h [30, 31]. An algorithm accurate to 2nd order in h was implemented in Fortran for comparison with the modified Runge-Kutta algorithm which could be implemented with Mathcad. Based on this comparison, both algorithms gave the same solutions over the range of parameters discussed in this report. We have found that as long as the stepsize is sufficiently small, typically γ_c^{-1} is appropriate, and the integration time is sufficiently long, typically on the order of 10^6 steps, the numerical integration produced consistent results. These results agreed with the analytical solutions of the linearized analysis in the appropriate limit.

For numerical simulation, the following coupled equations [7] are used:

$$\frac{da}{dt} = \frac{1}{2}\left[\frac{\gamma_c\gamma_n}{\gamma_s\tilde{J}}\tilde{n} - \gamma_p(2a + a^2)\right](1 + a) + \xi\gamma_c\cos(\Omega t + \phi(t)) + F_a, \tag{74}$$

$$\frac{d\phi}{dt} = -\frac{b}{2}\left[\frac{\gamma_c\gamma_n}{\gamma_s\tilde{J}}\tilde{n} - \gamma_p(2a + a^2)\right] - \frac{\xi\gamma_c}{1 + a}\sin(\Omega t + \phi(t)) + \frac{F_\phi}{1 + a}, \tag{75}$$

$$\frac{d\tilde{n}}{dt} = -\gamma_s\tilde{n} - \gamma_n(1 + a)^2\tilde{n} - \gamma_s\tilde{J}(2a + a^2) + \frac{\gamma_s\gamma_p}{\gamma_c}\tilde{J}(2a + a^2)(1 + a)^2, \tag{76}$$

where γ_s is the spontaneous carrier relaxation rate, γ_n is the differential carrier relaxation rate, γ_p is the nonlinear carrier relaxation rate, b is the linewidth enhancement factor, and $\tilde{J} = (J/ed - \gamma_s N_0)/\gamma_s N_0$ with e being the electronic charge and d the active layer thickness of

the laser. The normalized noise-source parameters F_a and F_ϕ are related to the spontaneous emission rate, R_{sp}, of the laser through the following relations:

$$\langle F_a(t)F_a(t')\rangle \;=\; \langle F_\phi(t)F_\phi(t')\rangle = \frac{R_{sp}}{2|A_0|^2}\delta(t-t'), \tag{77}$$

$$\langle F_a(t)F_\phi(t')\rangle \;=\; \langle F_\phi(t)F_a(t')\rangle = 0. \tag{78}$$

As we discuss below, the carrier-field resonance is key to the issues of stability, bandwidth enhancement and noise reduction. Because field noise generally dominates carrier noise where there is resonance enhancement, we do not include the carrier-noise source terms.

Many characteristics of a semiconductor laser can be modified by injection locking. Under weak injection locking, single-mode oscillation, frequency-chirp reduction [32], and linewidth improvement [33] in a laser can be realized. Under strong injection, the dynamic character-istics of a laser can be substantially changed. Our recent analysis [11, 12] has revealed that the modulation characteristics of a semiconductor laser can be significantly improved with strong injection locking under proper conditions. Using a tunable optical signal to probe a strongly injection-locked semiconductor laser, we have observed a parasitic-free intrinsic bandwidth that is beyond the K-factor limit and is more than three times the bandwidth of the laser in the free-running condition [34]. Besides bandwidth enhancement, our previous analysis also indicated that strong injection locking can lead to a broadband reduction of the laser noise as well [11]. However, an enhancement in the modulation bandwidth is not necessarily accompanied by a reduction in the laser noise.

Referring back to the bandwidth enhanced transceiver in Figure 1, the specific application will determine what properties of the semiconductor laser under optical injection need to be emphasized. To capitalize on the potential benefit of strong injection locking of a semicon-ductor laser for its practical application as a large-bandwidth, low-noise device, it is clearly necessary that conditions exist for bandwidth enhancement, noise reduction, and stable lock-ing to be simultaneously achieved. Here, we quantify such conditions. It is well known that except for very weak injection, stable locking occurs predominantly with the frequency of the injection signal negatively detuned from the free-running oscillation frequency of the laser

[18, 19]. However, even in the stable locking region, a locking-unlocking bistability has been observed above a certain injection level [35]. We use the conventional, edge-emitting laser as our model system. Because its parameters have been accurately determined, the simulation results agree exceedingly well with any experimental data that we have collected. In the cases where the linearized analytical model [12] applies, the analytical results are also shown for comparison.

We fix the current injection level at $\tilde{J} = 2/3$, which corresponds to an injection current level of 40 mA and a free-running output power of 9 mW. At this current level, the corresponding laser parameters that are used in our numerical and analytical calculations for the laser characteristics are $\gamma_c = 2.4 \times 10^{11}$ s^{-1}, $\gamma_s = 1.458 \times 10^9$ s^{-1}, $\gamma_n = 1.34 \times 10^9$ s^{-1}, $\gamma_p = 2.41 \times 10^9$ s^{-1}, $b = 4$, and $R_{sp} = 4.7 \times 10^{18}$ V^{2}m^{-2}s^{-1}. Meanwhile, at $\tilde{J} = 2/3$, the resonance frequency of this laser in the free-running condition is $f_r = 2.93$ GHz. All of these parameters were determined experimentally [13].

At a given injection current level, the characteristics of a semiconductor laser subject to an external optical injection depend on two key parameters of the injection signal: the frequency detuning, $\Omega/2\pi$, of the injection signal with respect to the free-running frequency of the laser and the injection parameter, ξ, that indicates the strength of the injection signal received by the laser. Figure 10 shows the mapping of different characteristic operation regions of the laser under injection as a function of these two parameters. In this figure, as well as in the two following figures, the thick solid curves are obtained from the linearized analytical solution whereas the open symbols represent data obtained from numerical simulation using the full nonlinear model. The thick broken curves are merely guides of the eye.

The locking region shown in Figure 10 is asymmetric with respect to the zero frequency detuning and opens up significantly at high injection levels. Curve a is the Hopf bifurcation boundary above which the laser becomes unstable though it may be locked. Curve e is the boundary below which the laser cannot be locked. The region between curves c and e is the locking-unlocking bistability region. Note that the locking-unlocking bistability does not occur at an injection level lower than $\xi = 0.06$ or at a detuning less negative than -8 GHz.

41
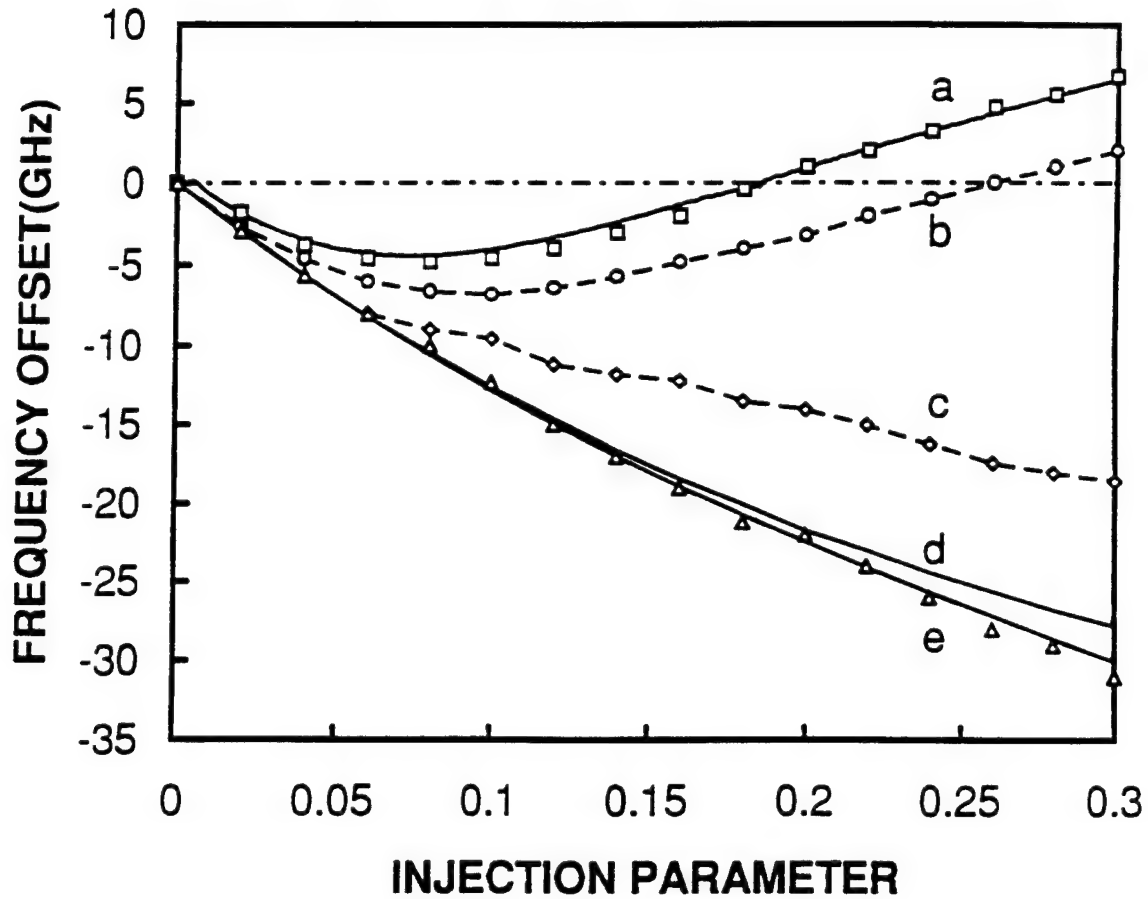
Figure 10: Mapping of different characteristic operation regions of the laser under injection as a function of the injection parameter and the frequency detuning of the injection signal. The thick solid curves are obtained from the linearized analytical solution while the open symbols are data obtained from numerical simulation using the full nonlinear model. The thick broken curves are merely guides of the eye. Curve *a* is the Hopf bifurcation boundary below which the laser is stably locked. Noise reduction under injection locking is found in the region below curve *b*. A locking-unlocking bistability is observed in the region bounded by curves *c* and *e*. Bandwidth enhancement under injection locking occurs in the region above curve *d*. The laser cannot be locked in the region below curve *e*.

In this bistability region, the laser can be either locked or unlocked, depending on the initial condition. If a laser is initially injection-locked with a set of parameters in the stable locking region between curves a and c, it remains locked while the injection signal is slowly tuned in frequency or in strength to cross the boundary marked by curve c into the bistability region. Conversely, if it is initially unlocked, it remains unlocked while the injection signal is tuned within the bistability region until curve c is crossed to enter the stable locking region when the laser suddenly becomes locked. Therefore, unconditionally stable locking occurs only in the region between curves a and c.

2.3.1 Resonance Frequency Enhancement and Noise Reduction

Returning to the analysis of the SDL laser, Figure 11 shows the resonance frequency of the laser under injection locking as a function of the injection parameter. Line d marks the resonance frequency $f_r = 2.93$ GHz for the laser in the free-running condition. Each of the thick curves corresponds directly to the curve that has the same label in Figure 10. For example, curve a in Figure 11 shows how the resonance frequency of the laser under injection locking varies along the Hopf bifurcation boundary and curve c shows how it varies along the bistability boundary. The thin dotted curves in Figure 11 are contour curves for fixed values of frequency detuning. They show how the resonance frequency varies with the injection parameter when the frequency detuning is fixed at a certain value in gigahertz that labels a curve.

While not a precise correlation, the resonance frequency is often a good indicator of the modulation bandwidth. From Figure 11, we find that bandwidth enhancement due to injection locking occurs within almost the entire locking region of interest shown in Figure 10. Only in a very narrow range between curves d and e within the bistability region does injection locking not lead to bandwidth enhancement. Most significant is the fact that bandwidth enhancement does occur in the entire stable locking region between curves a and c. In fact, it can be seen from Figure 11 that substantial bandwidth enhancement can be realized anywhere in the stable locking region for $\xi > 0.1$. Along the lower boundary of the locking region
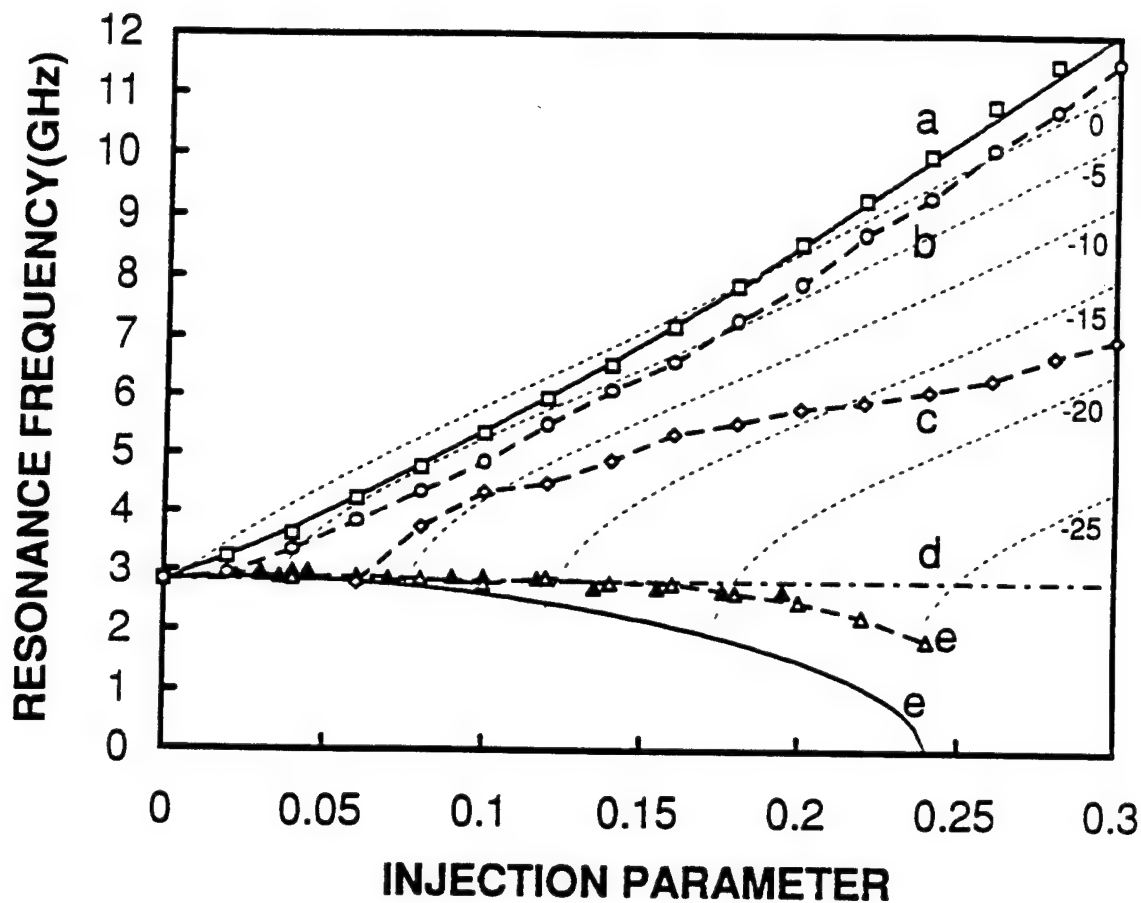
Figure 11: Resonance frequency of the laser under injection locking as a function of the injection parameter. Line d marks the resonance frequency $f_r = 2.93$ GHz for the laser in the free-running condition. Each of the thick curves corresponds directly to the curve that has the same label in Figure 10. The open symbols are data obtained from numerical simulation using the full nonlinear model. The closed triangles are experimental data taken under the conditions on curve e of Figure 4. The thin dotted curves are contour curves for fixed values of frequency detuning in gigahertz.

marked by curve e, the experimentally observed resonance frequencies, which are confirmed by the simulation data, disagree significantly with the analytically calculated values.

The data shown in Figure 11 seem to indicate that the largest benefit of strong injection locking can be realized by operating the injection-locked laser along or near the Hopf bifurcation boundary as the largest bandwidth enhancement occurs there. However, this conclusion does not consider the noise of the laser. Figure 12 shows the total power of the amplitude noise of the laser under injection locking, normalized to that of the laser in the free-running condition, as a function of the injection parameter. Line b marks the noise level of the laser in the free-running condition. Again, each thick curve corresponds directly to the curves in Figures 10 and 11 that have the same label. Curves d and e cannot be distinguished in Figure 12 because they virtually overlap. Each of the thin dotted contour curves in Figure 12 shows how the total noise of the laser varies with the injection parameter when the frequency detuning of the injection signal is fixed at the value in gigahertz that labels a particular curve.

It can be seen that noise reduction by injection locking occurs only in the region between curves b and e. In the region above curve b, the laser noise increases dramatically as the operation condition approaches the Hopf bifurcation boundary marked by curve a. This is expected because dynamic instability of the injected laser starts to appear in the region above the Hopf bifurcation boundary. The significant effect of dynamic instability on the noise of the laser can be very clearly seen by following the contour line of zero frequency detuning. For injection at the free-running frequency of the laser with zero frequency detuning, the laser undergoes several different nonlinear dynamic states, including period doubling and chaos, when the injection parameter varies between $\xi = 0$ and $\xi \approx 0.18$. The high noise levels represented by the zero-detuning contour curve within this range are a clear indication of the instability associated with such nonlinear dynamics.

Though the region without noise reduction covers a large range between curves a and b in Figure 12, it represents only a small range of operation conditions shown in Figure 10 and a still smaller range of variation in the resonance frequency shown in Figure 11. In
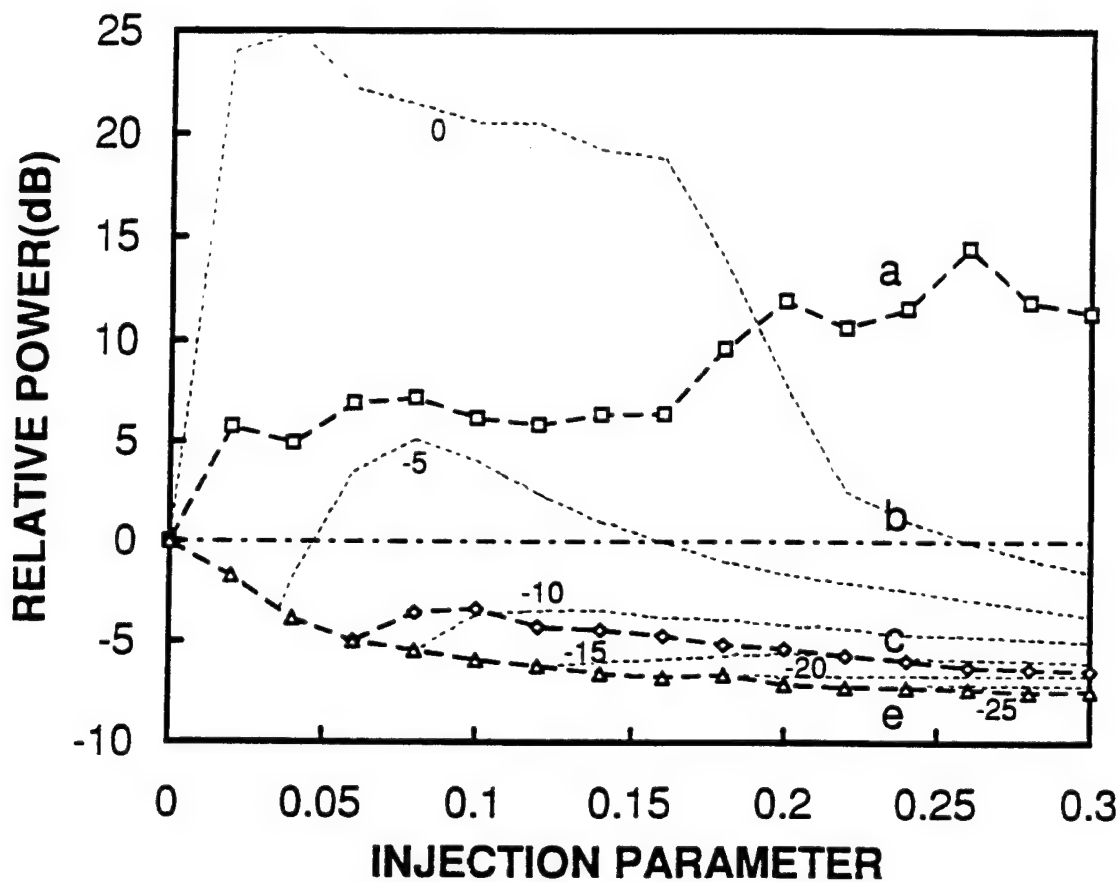
Figure 12: Total noise power of the laser under injection locking, normalized to that of the laser in the free-running condition, as a function of the injection parameter. Line *b* marks the noise level of the laser in the free-running condition. Each thick curve corresponds directly to the curves in Figures 10 and 11 that have the same label. Curves *d* and *e* cannot be distinguished in this figure because they virtually overlap. The thin dotted curves are contour curves for fixed values of frequency detuning in gigahertz.

46

contrast, the bistability region bounded by curves c and e occupies a relatively large range of operation conditions shown in Figure 10 and an even larger range of variation in the resonance frequency shown in Figure 11, but it covers only a small range of maximum noise reduction shown in Figure 12. In the large region bounded by curves b and c, bandwidth enhancement, noise reduction, and stable locking can be simultaneously fulfilled.

By correlating the data shown in Figures 11 and 12, we find that when the injection parameter is fixed at a certain value, the frequency detuning for maximum bandwidth enhancement differs from that for maximum noise reduction. However, at a given value of frequency detuning, both bandwidth enhancement and noise reduction are improved as the injection parameter is increased over the range of parameters considered. At injection levels above those considered here, the resonance frequency can be sufficiently enhanced that there is a significant dip in the modulation response at frequencies below the resonance frequency [12]. Significant bandwidth enhancement coupled with noise reduction under a stable locking condition can be realized with a strong injection signal over a properly chosen frequency detuning range. For example, for the laser biased at $\tilde{J} = 2/3$, stable locking of the laser with an injection signal of $\xi = 0.3$ at a frequency detuning of -10 GHz triples the resonance frequency to 9 GHz while simultaneously reducing the total laser noise by 5 dB. Greater bandwidth enhancement with equivalent noise reduction requires that the laser be subjected to a stronger injection field and/or be biased to a larger value of $\tilde{J}$.

2.3.2 Dynamic Range

In addition to the bandwidth and noise characteristics, one is also interested in the dynamic range of a semiconductor laser. Because semiconductor lasers are a nonlinear medium, a large modulation signal will eventually lead to saturation and to the generation of additional frequencies in the modulation spectrum. Generation of additional frequencies also occurs because of chirp, the tendency of the laser to be both frequency and amplitude modulated by a change in the carrier density. Previous work has shown that operation under strong injection locking leads to a reduction of the frequency chirp [36] and recent calculations using

47

a linearized model similar to the one described above has shown that chirp reduction and modulation distortion can both be achieved when an injection-locked laser is operated in the region of bandwidth enhancement [37, 38].

As the current program was ending, we have started some initial investigations of dynamic range and nonlinear distortion to strong signal modulation. Our results are quite preliminary. As an example, Figure 13 compares the relative gain for a modulation current which is added to the steady (dc) bias current. The operating point discussed above, $\tilde{J} = 2/3$, $\xi = 0.2$ and an offset frequency of -10 GHz, is used. When the modulation index, m, the ratio of the current modulation amplitude to the constant bias current level, is approximately 0.1 or less, then the current-to-light gain closely follows the small signal curve. Compared to the free-running case, the magnitude of the modulation is generally greater at the modualtion frequencies of interest. However, because the injected optical signal simultaneously increases the average optical output, the fractional modulation is actually reduced relative to the free-running case. At higher modulation levels, there is some deviation from the small-signal modulation characteristic, as expected. For instance, there is a clear drop in the gain for modulation frequencies near the resonance frequency for $m = 1$, as shown by comparing the two sets of calculated data in Figure 13. Even here, however, the gain is reduced by < 3 dB. Our full nonlinear calculations confirm the chirp reduction previously calculated using the linearized model.

High modulation levels also generate extra frequency components in the nonlinear medium. Also shown in Figure 13 is a calculated spectrum showing the amplitude modulation signals and noise spectrum that would be measured when the laser is modulated by two components, at 4 GHz and 7 GHz, each with $m = 0.06$. The amplitude of the noise assumes that the frequency resolution for the measurement is approximately 120 MHz, and the noise spectrum reflects the dominant role of the spontaneous emission noise. Appearing above the noise background are nonlinear mixing peaks at 3, 8, 11, and 14 GHz. These components would obscure any real signals at these frequencies with $m < 0.0006$. This dynamic range compares favorably with a free-running laser diode. The lower limit of the dynamic range is ultimately
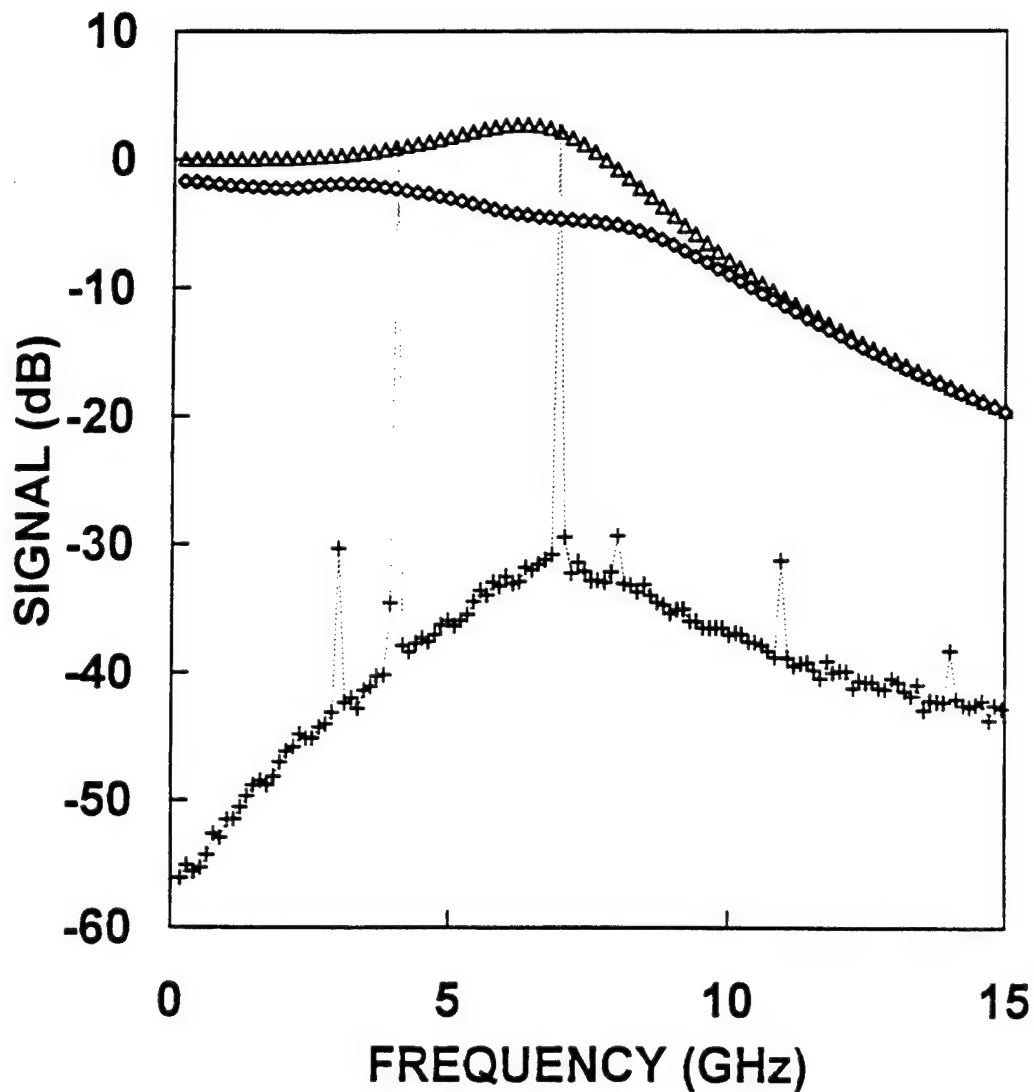
Figure 13: Saturation and nonlinear frequency generation due to a large modulation current which is added to the constant bias current of an injection-locked laser. The parameters of the injection-locked laser are discussed in the text. The relative amplification at the modulation frequency is nearly constant for a modulation index of $m = 0.1$, triangles, or less, but saturates near the resonance frequency for $m = 1$, diamonds. The amplitude modulation spectrum, crosses, for the laser undergoing simultaneous modulation at 4 GHz and 7 GHz, each with a modulation index of $m = 0.06$ shows harmonic, sum and difference fequencies just visible above the noise background. The noise spectrum, dominated by spontaneous emission noise, assumes a frequency resolution of $\sim$ 120 MHz.

set by the noise level. The background noise level in Figure 13, set by the bandwidth of our calculation, is quite high. With a smaller frequency resolution bandwith, the dynamic range can be improved when the modulation index of the peak frequency component is reduced. Further work is underway to quantify modulation distortion and dynamic range characteristics.

3.0 EXPERIMENTAL APPARATUS

In this program, we have carefully investigated the modulation and noise characteristics and nonlinear dynamics of two very different semiconductor laser types. The first is the 5300/5400 series of laser diodes from SDL when subject to external optical injection. For our purposes they are attractive because of their nearly single-mode operation, though as we describe later, mode hopping sometimes occured under external optical injection, and the fact that in past experimental work we have determined the key dynamic characteristics of these lasers [13]. The second laser type is a VCSEL whose properties have been published elsewhere [39, 40]. Due to its very short cavity, wavelength-specific mirrors and gain bandwidth, the VCSEL oscillates in only one longitudinal mode. As we shall describe later in this report, this feature was useful for experimentally verifying specific features of the nonlinear dynamics in semiconductor lasers under optical injection.

Experimental observation of the opical output of a semiconductor laser under external optical injection is a two-laser experiment while optical probing of the laser under external optical injection requires three lasers. The two-laser configuration is also useful for measuring the noise characteristics and dynamic parameters of the free-running laser and for determining the characteristic resonance frequencies of the injection-locked laser. This is because the spontaneous emission noise source effectively acts as a weak optical probe of the injection-locked laser. Therefore, we will first describe the two-laser configuration used for the nonlinear dynamics measurements and then continue with a description of the three-laser apparatus used for the measurement of the optical modulation characteristics of an injection-locked semiconductor laser.

Figure 14(a) shows the two-laser experimental setup. The output of one laser diode (LD1), the master laser, at a frequency ν_1 waspassed through an optical isolator and variable attenuators and directed into a second laser (LD2), the slave laser, oscillating at $\nu_0 = \omega_0/2\pi$. Thus the frequency offset $f = \Omega/2\pi$ is given by $\nu_0 + f = \nu_1$ and can be varied by varying ν_1. Both lasers were temperature and current stabilized. To bring them to near-degenerate
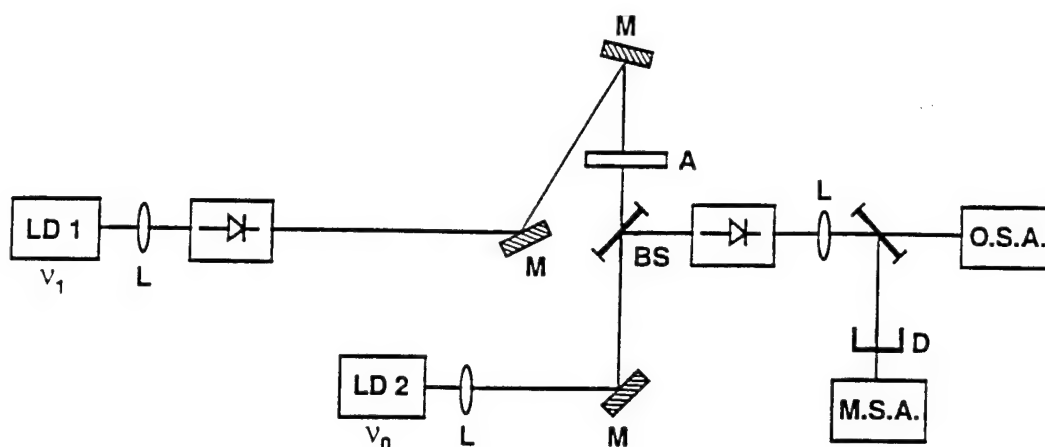
Figure 14(a). Two-laser configuration.
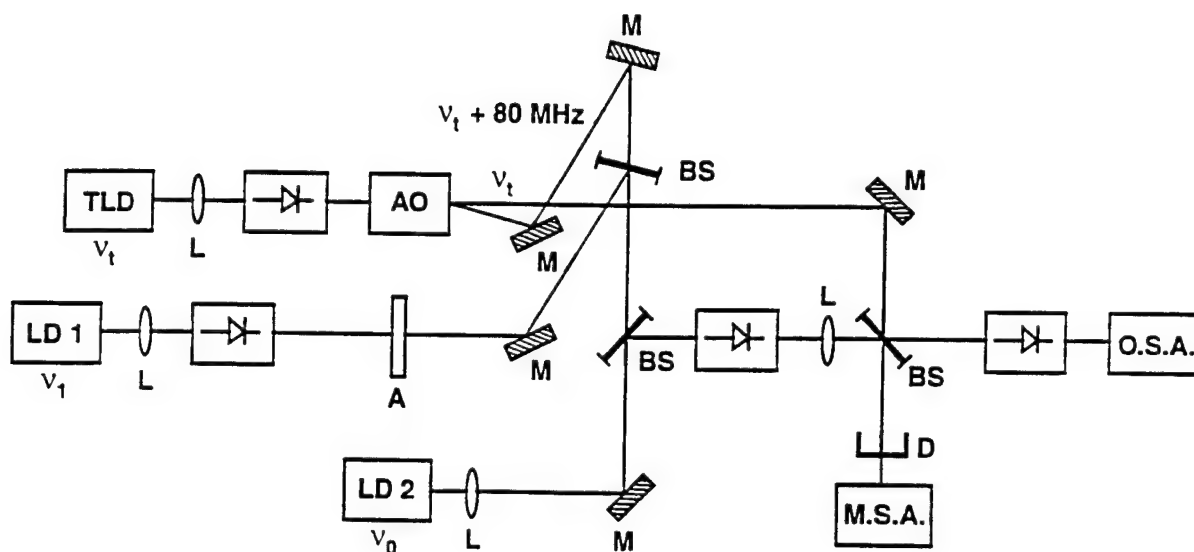
Figure 14(b). Three-layer configuration.

LEGEND			
TLD:	Tunable laser diode	A:	Variable attenuator
LD:	Laser diode	BS:	Beamsplitter
L:	Lens	D:	Fast photodiode
─▷├ :	Optical isolator	M.S.A:	R/F-microwave spectrum analyzer
A.O.:	Acoustooptic modulator	O.S.A.:	Optical spectrum analyzer
M:	Mirror		

Figure 14: Schematic diagram of the experimental apparatus. (a) two-laser configuration and, (b) three-laser configuration.

52

operating frequencies, the temperature was adjusted for gross frequency changes and then the current was adjusted for fine tuning of the frequency offset f. Optical isolators were used to avoid mutual injection and to reject back-reflected light from any components in the optical path. The output of the injected laser was monitored using both optical and microwave/radio-frequency spectrum analyzers to measure both the optical field and power spectra. In this two-laser configuration, the optical spectrum was monitored with a Newport SR-240C scanning Fabry-Perot which has a free spectral range of 2 THz and a finesse of approximately 50,000, giving an optical frequency resolution of about 40 MHz. The power spectrum was obtained by detecting the output of the injected laser with a fast photodiode of 7 GHz frequency response and displaying the photodiode signal on the spectrum analyzer. Both spectra are necessary for the determination of key dynamic parameters required for the comparison of experimental data with numerical data [13]. Measuring both spectra simultaneously allowed us to distinguish between amplitude and phase modulations of the output of the injected laser.

The first master/slave combination in the two-laser configuration consisted of two Spectra Diode Labs SDL-5301-G1 single-longitudinal and transverse mode GaAs/AlGaAs quantum-well lasers operating at 827.6 nm. These lasers are conventional Fabry-Perot edge-emitting lasers with one facet coated for high reflection and the output facet coated for a reflection of a few percent. The threshold current for the injected laser was approximately 24 mA and the data presented here were taken at an injection current level of 40 mA, $\tilde{J} = 2/3$. Other dynamic properties for this laser are summarized in Table 1 on page 11. The master laser was operated at a higher current level, approximately 55-65 mA, to have lower noise characteristics. The intrinsic spontaneous emission noise of the laser oscillator acts like a weak optical probe of the injection-locked slave laser.

During this program, after several years of consistently good performance, the slave laser underwent a serious performance drop and could no longer be overlapped in frequency with the master laser. Overlapping two of the SDL lasers is not a trivial matter because they do not have a continuous tuning spectrum under temperature and current changes. The lasers

undergo longitudinal mode hops at points which vary randomly from laser to laser. We tried a variety of laser combinations using new SDL-5411-G1 lasers. However, while the original lasers were made with a 500 μm cavity, the newer lasers all had a 750 μm cavity. The longer cavity meant a reduced value of the laser-cavity photon decay rate. This translates into a smaller modulation bandwidth for both the free-running and injection-locked lasers, all other parameters being equal. The longer cavities did allow the lasers to be operated at higher pump currents, yielding larger output powers. After some trial and error, we found that the best combination of available lasers was to use the original master laser as the slave lasers and one of the newer, higher power lasers as the pump laser. We were able to achieve good frequency overlap at approximately 826.8 nm.

With an operating master and slave laser, we could proceed with the modifications required for measuring optical modulation characteristics of the injection-locked slave laser. A schematic of the new experimental configuration is shown in Figure 14b. An optically isolated master laser, LD1, operating at the optical frequency ν_L, injection locks, in a dynamically stable state, a slave laser, LD2, initially operating at the free-running frequency ν_0. The output from LD2, after passing through other optical isolators, is detected by either a scanning Fabry-Perot optical spectrum analyzer or a fast photodiode, microwave spectrum analyzer combination. The output of an optically isolated, tunable, external cavity semiconductor laser, TLD, operating at the frequency ν_1, is passed through an acoustooptic modulator where part of the beam is split off and frequency shifted by 80 MHz. This shifted output is used to probe the modulation characteristics of the slave laser while the unshifted part of the beam is used as a local oscillator. When the microwave spectrum analyzer is set to a narrow frequency window at 80 MHz, then, as the probe laser is scanned about ν_L, the microwave spectrum analyzer measures the spectrum of the regeneratively amplified probe signal. When the local oscillator beam is blocked so that only the slave laser output is captured by the fast photodiode, then the microwave spectrum analyzer measures the amplitude modulation spectrum of the laser. An upgraded photodiode extended the frequency response of the amplitude modulation measurements to 15 GHz.

The slave has very similar dynamic parameters to the same type of laser that we characterized earlier [13]. Specifically, $\gamma_c = 2.5 \times 10^{11}$ s^{-1}, $\gamma_s = 1.5 \times 10^9$ s^{-1}, $\gamma_n = 2\tilde{J} \times 10^9$ s^{-1} and $\gamma_p = 3.6\tilde{J} \times 10^9$ s^{-1}, where $\tilde{J}$ is the differential injection current above threshold, normalized to the threshold current. A different value was found for the linewidth enhancement factor, $b = 5 \pm 1$. For the measurements reported here, $\tilde{J} = 2.13$. The master laser was an SDL 5411-G1 laser. Both lasers were temperature and current stabilized. The probe laser, a New Focus Model 6226 external cavity semiconductor laser, could be scanned over a calibrated frequency range of approximately 40 GHz by dithering a mirror mounted on a piezoelectric crystal.

Feedback to the slave laser from its collimating lens was discovered to play a role in the understanding of details of some of the regenerative amplification and amplitude modulation spectra that we measured. The effect of feedback into the oscillating mode of the injection-locked slave laser spectrum will be discussed later. Here, we will briefly discuss the effects of feedback on the optical probe. Because the probe laser follows the same optical train as the master laser, its coupling into the slave laser could not be simultaneously optimized with the master laser. Even when feedback effects on the master laser and injection-locked slave laser were minimized, it was found that the probe laser was influenced by etaloning effects due to the collimating lens. An example is shown in Figure 15. The figure shows the raw data of two regenerative amplification spectra and the noise level of the measurement system. One of the spectra, with the strong peak, shows the measurement of the free-running laser biased at $\tilde{J} = 2.13$. The frequency axis of the figure is referenced to the free-running oscillation frequency. The other spectrum is taken at the same optical frequency but with the bias reduced to $\tilde{J} = 0.5$. The oscillation frequency has now shifted so that the laser resonance is not recovered in the heterodyne spectrum. However, there are clearly repeating maxima and minima offset by approximately 10 GHz. Inspection of the $\tilde{J} = 2.13$ spectra reveals that the same periodic feature is evident. The frequency spacing identifies a cavity formed by the slave laser and the collimating lens. The fact that the feature is approximately the same in strength in both the on-resonance and off-resonance spectra shows that the etaloning is
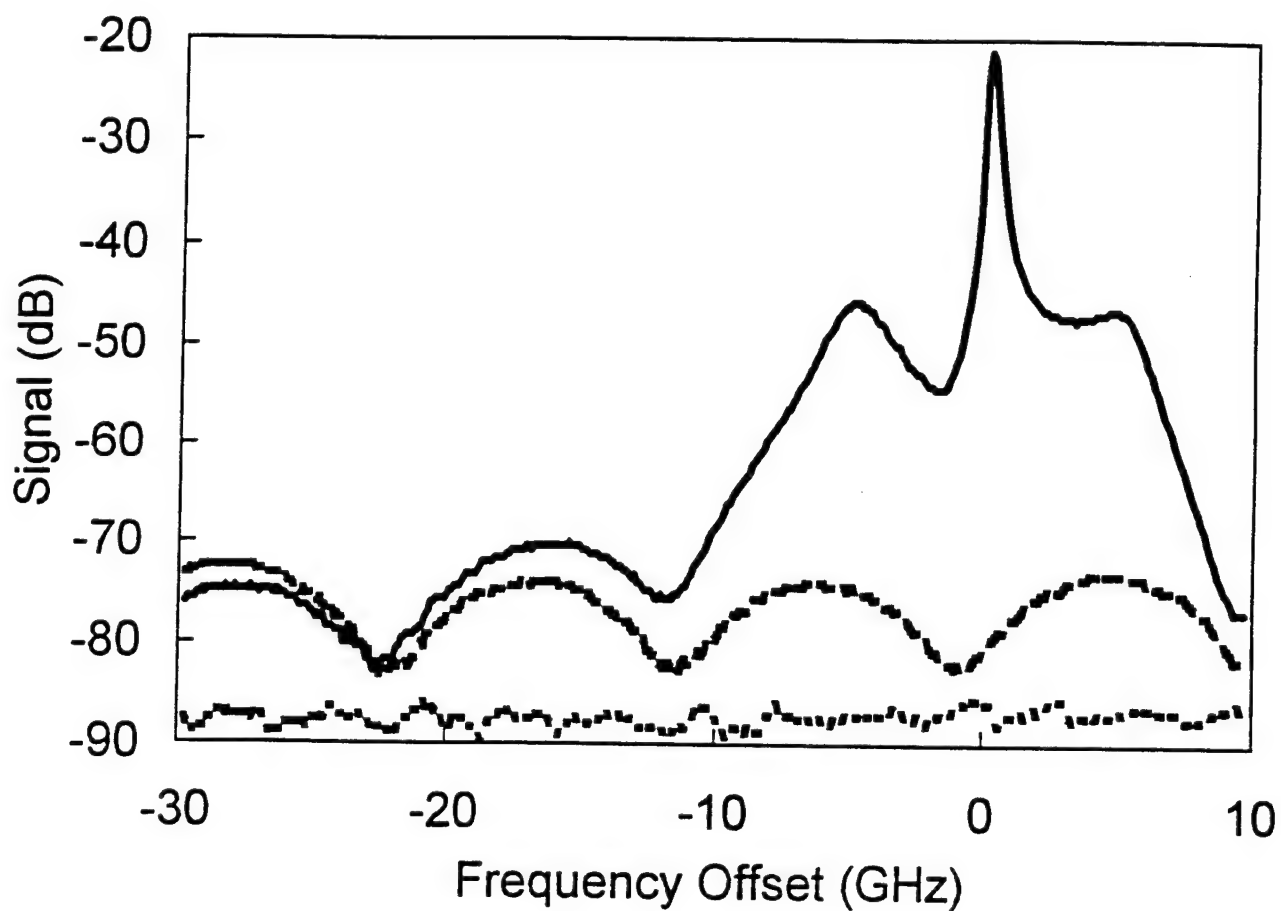
Figure 15: Spectra of the regenerative amplification sideband due to a weak optical probe showing the effects of a weak optical cavity for the probe laser formed by the slave laser and its collimating lens. The cavity does not use the oscillating mode of the slave laser as is seen by the nearly equal strength etaloning in a resonant spectrum taken at $\tilde{J} = 2.13$, solid curve, and a nonresonant spectrum taken at $\tilde{J} = 0.5$, dashed curve. Also shown is the noise level of the measurement system, dotted curve.

not due to coupling into the oscillating mode. The weak optical probe has a frequency-dependent amplitude due to the frequency-dependent feedback of the weak optical cavity formed for the probe beam. The effects of this cavity can be taken into account by simply correcting for the amplitude variation. Because the spectrum analyzer gives the signal in dB, one simply cancels out the etalon effects by adding an equal etalon component to the spectrum which is 180 degrees out of phase. All subsequent modulation data presented here have been corrected for this linear effect on the raw data.

Data from one other master-slave combination are also presented in this report. A New Focus Model 6226 tunable external cavity laser was the master laser and a VCSEL was the injected laser. Unfortunately, from the perspective of getting useful, quantitative results, the VCSEL had the habit of spontaneously changing its output characteristics, such as threshold current, output wavelength, and dynamic parameters, during the course of this research program. The source of this feature is not clear. Such behavior has not been reported in the literature, but, in private conversations, other experimentalists investigating VCSELs have observed such behavior. Throughout much of the program, and for most of the data presented in this report, the VCSEL had the characteristics described below. When the VCSEL changed, it could be recharacterized by our model with appropriate dynamic parameters. Initially, the VCSEL had a threshold for laser oscillation of approximately 3.9 mA and emission wavelength of approximately 850 nm [39, 40, 41]. The total output power as a function of bias current is shown in Figure 16. At currents under approximately 6 mA, the VCSEL oscillates in the lowest order spatial mode but, due to the symmetry of the device, can emit in two orthogonally polarized modes. Also shown in Figure 16 is the polarized output power as a function of the injection current. The higher threshold polarization component eventually dominates the output and, when the output starts to be divided among several spatial modes, all show this polarization. The laser operated with these characteristics during the period that the threshold data and the polarization switching data that are presented later were taken. The dynamic characteristics of the laser were reported in Reference [41]. More recently, the laser operated with a threshold of approximately 3.2 mA. Among the dynamic parameters the most notable change was the linewidth enhancement factor which
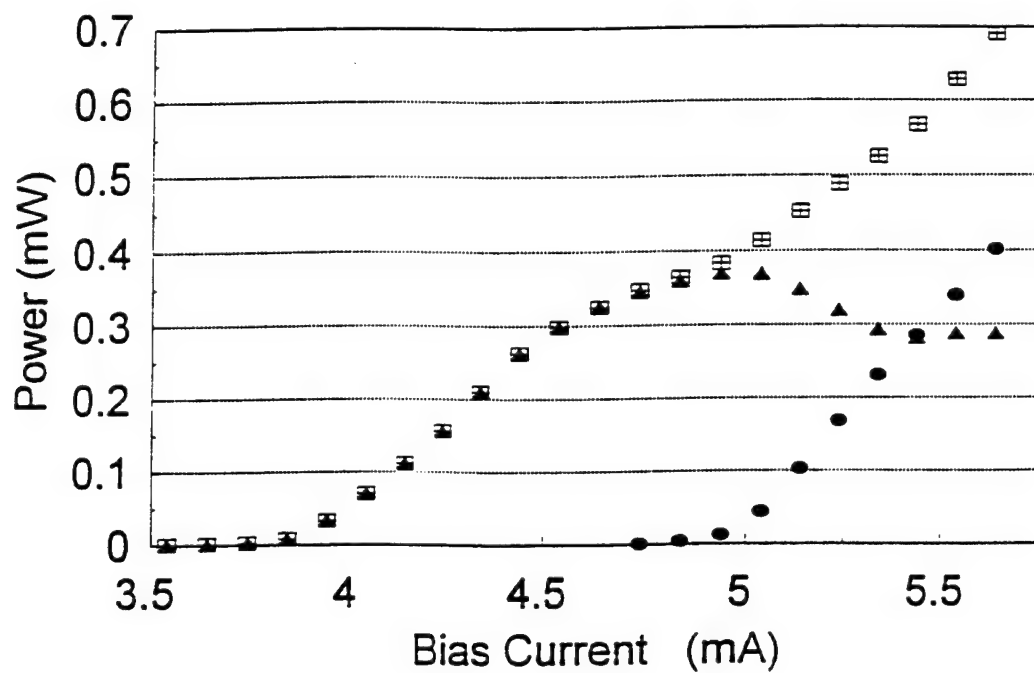
Figure 16: Output power of the VCSEL under study at bias currents where the output power is in one spatial mode with two orthogonal polarization modes.

was reduced from approximately 5-6 to 2-3. The data describing operation above threshold and showing the locking/unlocking bistability were taken with these characteristics.

4.0 SEMICONDUCTOR LASER ABOVE THRESHOLD

When a semiconductor laser is subjected to injection by a near-resonant external optical field, the laser output will exhibit a variety of optical spectra. By comparison between the experimentally observed spectra and calculated spectra, we have been able to categorize the dynamics. Calculated spectra are obtained by numerically integrating the normalized, coupled equations, then performing a Fourier transform on the resulting time series to calculate the spectra.

As we have already discussed, some key features can be predicted from the perturbation analysis with the set of coupled equations which assumes that the changes to the amplitude, phase and carrier density are sufficiently small that the three equations can be linearized. Figure 17 shows a typical mapping of the predicted locking and stability range based on a linearized analysis [12]. The actual values used to calculate the map correspond to the injected SDL laser at the bias current of 40 mA, $\tilde{J} = 2/3$, but the qualitative characteristics are more general. The analysis predicts an asymmetric locking range [19] with a bounded range of unstable operation within the locking range. The circulating field amplitude increases with increasing injection parameter and/or decreasing offset frequency within the locked region. A larger value of b increases the low frequency boundary of the locked operating range and increases the range of unstable dynamics. A larger value of $\tilde{J}$ shifts the unstable region to larger values of ξ with the low ξ limit shifting approximately in proportion to $\tilde{J}$ or A_0^2 and the upper limit shifting approximately with A_0 [12]. The analysis also predicts that the eigenvalues of the coupled equations are strong functions of the operating point. Figure 18 plots the eigenvalues, or resonance frequencies of the field-free carrier coupling, as a function of ξ for two different cases. The first case is for external optical injection at the free-running frequency of the injected laser. This corresponds to a phase offset of $\arctan b$ between the master and injected laser optical fields in the linearized analysis. For this case the resonance frequencies increase monotonically with ξ. In contrast, when the injection frequency is changed as ξ is increased so that there is no phase offset between the master and injected laser optical fields, a case which approximately corresponds to following the low

60
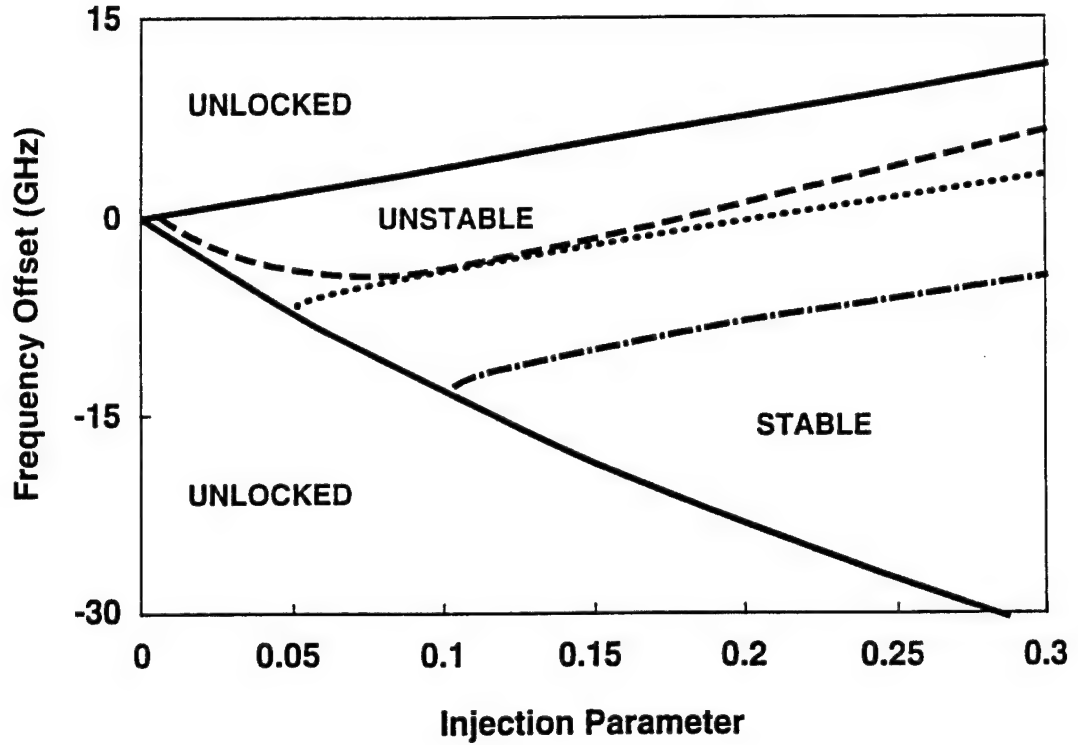
Figure 17: Mapping of the locking and stability characteristics of the conventional, edge-emitting semiconductor laser with $\tilde{J} = 2/3$ as a function of the frequency offset between the locking and free-running laser fields and the injection parameter, ξ. The thick solid line is the boundary of the injection-locked region. Shown in the interior of the locking region is the Hopf bifurcation line (thick dashed line) separating the stable and unstable operating regimes. The positive frequency boundary of the locked region is a line of constant output field amplitude at the free-running level, A_0. Also shown are the lines for $1.1A_0$ (dotted) and $1.2A_0$ (dot-dashed).
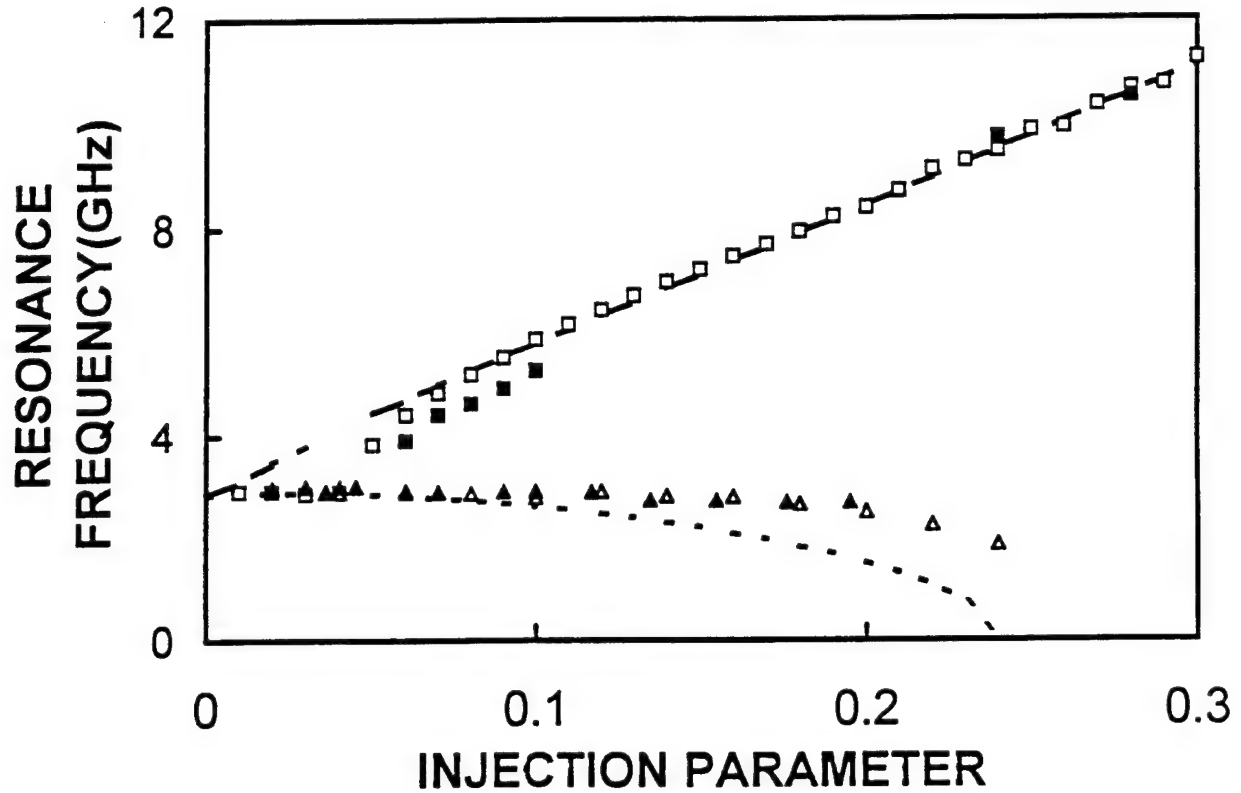
Figure 18: Calculated eigenfrequency and measured frequency of the optical spectrum side-band peak for the conventional, edge-emitting semiconductor laser with $\tilde{J} = 2/3$ as a function of the injection parameter, ξ. Experimental data are shown as solid symbols, calculated frequencies using the full nonlinear equations are shown as open symbols and calculated eigenfrequencies from the linearized approximation are shown as curves. Two cases are plotted: Dashed Line and Squares - injection at the free-running optical frequency, Dotted Line and Triangles - injection corresponding to $\phi_L = 0$. The former case shows unstable operation for $0.007 < \xi < 0.24$ while the latter case is always stable.

frequency boundary of the locked operating region, the linearized analysis predicts a decreasing resonance frequency. Also shown in Figure 18 are the resonance frequencies calculated by numerically integrating the full nonlinear equations and Fourier transforming the resulting time series and the experimentally measured resonance frequencies. The experimental data show excellent agreement with the full nonlinear calculation, and good agreement with the linearized analysis. The major discrepancies with the linearized analysis occurs within the region where the full nonlinear analysis indicates chaotic dynamics at the $\phi_L = \arctan b$ phase offset or bistable operation at the phase offset of $\phi_L = 0$.

4.1 NONLINEAR DYNAMICS

Using equations 74 to 76 with experimentally determined parameters, we have been able to produce calculated spectra quite similar to the observed spectra. When the noise source is eliminated from the calculated spectra, the spectra can be directly related to the underlying dynamics induced by the optical injection [7, 8, 9]. As an example, Figure 19 shows the progression of observed spectra from the conventional, edge-emitting laser when subjected to resonant, $\Omega = 0$, optical injection as the injection parameter, ξ, is increased. To determine the injection level, we calibrated the system by measuring the four-wave mixing spectrum in the weak injection limit and used our previously developed techniques to compare the generated sideband signal with the central peak [13]. The injected power was varied by changing the attenuation in the path of the master laser and the power level was monitored. In the spectra, the frequency is relative to the free-running frequency or, equivalently, the injection frequency and the scale of the signal level is consistent throughout the series. Expanded versions of the spectra showing weak details are referenced to the right vertical axis scale. Figure 19(a) is the free-running spectrum consisting of a single peak and weak relaxation resonance sidebands which are visible in the expanded scale version of the spectrum. The asymmetry is due to b. In Figure 19(b) $\xi^2 = 1 \times 10^{-4}$, and the spectrum consists of relatively narrow peaks separated by a frequency spacing of 2.9 GHz, which is the relaxation resonance frequency of the free-running laser. These are typical features of highly unstable injection locking [19]. In Figure 19(c) $\xi^2 = 3 \times 10^{-4}$, broad period-doubling features appear in the

63
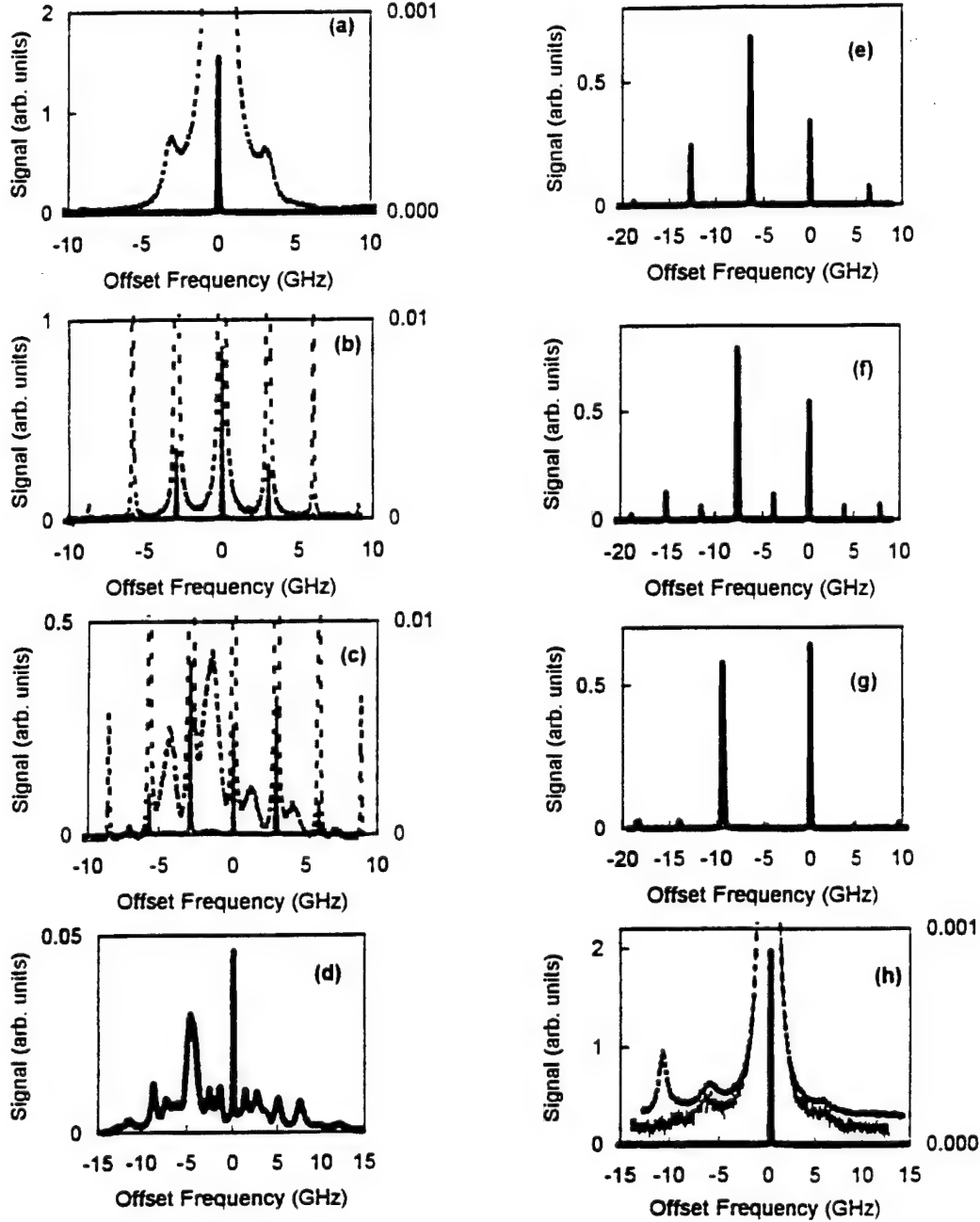
Figure 19: Measured optical spectra of the conventional, edge-emitting semiconductor laser with $\tilde{J} = 2/3$ under optical injection at the free-running optical frequency: (a) free-running operation with expanded scale showing the relaxation resonance sidebands, (b) unstable injection locking, limit cycle, at $\xi^2 = 1 \times 10^{-4}$ with expanded scale spectrum, (c) period doubling at $\xi^2 = 3 \times 10^{-4}$ with features shown clearly in the expanded scale, (d) chaotic dynamics at $\xi^2 = 1.3 \times 10^{-3}$, (e) limit cycle at $\xi^2 = 3.6 \times 10^{-3}$, (f) period doubling at $\xi^2 = 7.2 \times 10^{-3}$, (g) transition back to limit cycle at $\xi^2 = 1.7 \times 10^{-2}$, and (h) stable operation at $\xi^2 = 8.5 \times 10^{-2}$ along with expanded scale spectrum and the expanded scale sideband spectrum of the master laser.

spectrum between the narrow oscillation peaks [8]. They are stronger at negative detunings, a reflection of the positive value of b. Comparing the expanded versions of (b) and (c) clearly shows the qualitative diffference between the spectra before and after the period-doubling features emerge. The field noise source causes the broadening of the period-doubling features. When it is removed in the calculated spectra, sharp period-doubling peaks result [8]. In Figure 19(d), $\xi^2 = 1.3 \times 10^{-3}$, the spectrum becomes dominated by a broad pedestal and many secondary peaks develop. Relatively little energy remains in the narrow injection spike. At this stage chaos has fully developed and elimination of the noise source in the calculated spectra does not change the qualitative features [8]. Within the region of chaotic dynamics, a fraction of the oscillating power, increasing to up to 35% as the injection level is increased, is shifted from the principal oscillating mode into several of the weak side modes. Over a narrow injection range, the broadened spectrum collapses again into an equally spaced set of narrow features, as shown in Figure 19(e) where $\xi^2 = 3.6 \times 10^{-3}$, and the principal mode regains its full power [7]. Now, however, the separation of the peaks has increased and the spectrum is much more strongly shifted to the negative components. At still higher injection levels, Figure 19(f) where $\xi^2 = 7.2 \times 10^{-3}$, a new, clear period doubling is observed with a further increase of the peak separation and relative strengthening of the negative frequency components. The strongest spectral feature is clearly frequency-shifted, pushed by the resonant injection. The period doubling peaks then steadily decrease in amplitude as the resonance peak monotonically increases while the peak separation continues to increase. The spectra in Figure 19(g) is observed when $\xi^2 = 1.7 \times 10^{-2}$ and the injection peak again begins to dominate the spectrum. Eventually, the side peaks decrease in magnitude so that only a single peak at the injection frequency dominates the spectrum. In Figure 19(h) $\xi^2 = 8.5 \times 10^{-2}$ and stable dynamics has been reestablished. The peak separation has now increased to 10.5 GHz and the side peak is visible in the expanded spectrum. Also visible in the expanded spectrum are replicas of the relaxation resonance features of the master laser. The identification of these features is confirmed by comparison with sideband spectrum of the master laser, also shown. At high injection levels, the noise sidebands of the master laser appear in the spectrum of the injection-locked slave. These noise features do not reflect the dynamics of the injected laser system. The dynamics are reflected in the

shifted resonance feature. Note that the strong asymmetry of the resonance peaks continues when stable dynamics has been reestablished. The weak asymmetry in the resonance peaks of the free-running laser has become a strong asymmetry in the injection-locked laser. The measured shift in the resonance peaks is compared with the calculated eigenfrequencies of the coupled equations in Figure 18 and shows very good agreement with the full nonlinear calculation and reasonable agreement with the linearized treatment.

To understand the deterministic dynamics, the full nonlinear coupled equations are first solved with the noise source terms set to zero. Figure 20 depicts the numerically obtained bifurcation diagram of the values of the extrema of the amplitude, $a(t)$, versus the injection parameter, ξ. As the injection level is increased, the steady state is destabilized and the relaxation frequency is undamped (Hopf bifurcation), in agreement with the linear stability analysis. Further increasing the injection leads to a period-doubling bifurcation route to chaos and then a similar, but reversed, route out of chaos. To confirm the chaotic nature, the Lyapounov exponents and the corresponding Kaplan-Yorke dimension of the attractor have been calculated [42]. For $\xi = 0.03$, the three Lyapounov exponents are $0.0145\gamma_c$, 0.0, and $-0.0298\gamma_c$, and the Kaplan-Yorke dimension is 2.48. The positive Lyapounov exponent is a clear measure that the system is chaotic in this parameter range. At even higher injection levels, the bifurcation diagram shows a second period-doubling. Finally, at the highest injection levels, the laser diode reverts to stable operation (reverse Hopf bifurcation). Therefore, the deterministic dynamics is seen to largely determine the experimentally observed optical optical spectra and to reproduce all of the key changes in the spectral characteristics which we observe.

When both coherent injection and spontaneous emission are present, there is, effectively, a fluctuating injected field. This leads to a blurring of the period-doubling cascades into and out of chaos. In the forward cascade, only the first period-doubling is not obscured, and the new frequency components are severely broadened. The reverse cascade is completely obscured. This effect can be numerically recovered by including spontaneous emission noise sources in the amplitude and phase equations. Figure 21 compares calculated spectra with
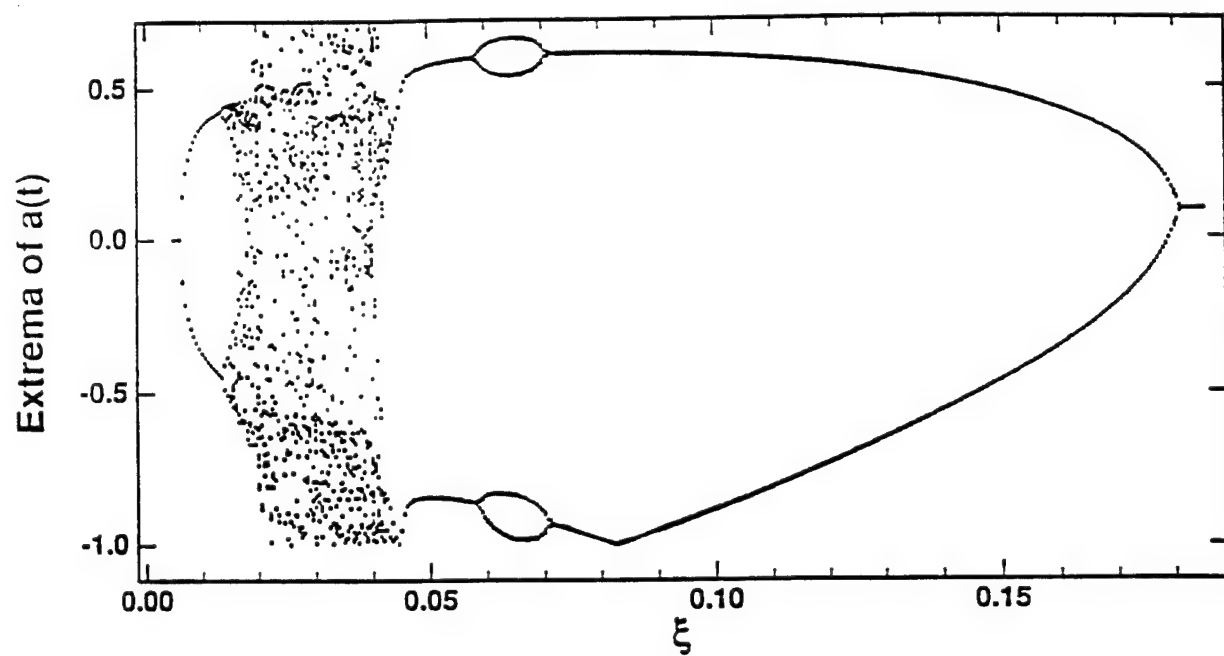
Figure 20: Numerically calculated bifurcation diagram of the extrema of the normalized optical field amplitude, $a(t)$, versus the normalized injection level, ξ. Injection is at the free-running frequency of the slave laser. Experimentally determined parameters of the semiconductor laser are used in the calculation.

and without the noise source terms at three injection levels. Without noise, a region of period doubling, Figure 21(a), and period quadrupling, Figure 21(b), are clearly distinguishable in the forward cascade. With noise, however, the calculations show only broadened period-doubling features, Figures 21(d) and (e), which are similar to the experimental data shown in Figure 19(c). In the period-doubling bubble at higher injection levels, however, the noise does not severely broaden the new spectral peaks, as shown in Figures 21(c) and (f). Likewise, the measured spectrum in Figure 19(f) has sharp period-doubling features.

Before proceeding to a more general picture of the dynamics induced under external optical injection, we distinguish a special type of period-doubling-like spectra, the region of sub-harmonic resonance [10]. Here, the half-offset frequency feature can totally dominate the frequency component offset from the central peak by the resonance frequency. Figure 22 shows a set of spectra which illustrate the subharmonic resonance. Again, the offset frequency is referenced to the frequency of the free-running laser. In these spectra the master laser is offset by ≈ 5.5 GHz and the injection level is varied. A complementary set of spectra, where the injection level is held constant while the offset frequency is varied from below to above twice the relaxation resonance frequency of the free-running laser, has been presented elsewhere [10]. At low injection levels the spectrum consists of narrow, weak sidebands, equally and oppositely offset from a main peak with its relaxation resonance sidebands, as shown in Figure 22(a). These narrow features are due to regenerative amplification of the injected signal and four-wave mixing between the injected signal and the central peak [13]. As the injected signal is increased, the spectral features near the relaxation resonance frequency narrow and increase, Figure 22(b) where the injection level is $\xi^2 = 2.1 \times 10^{-4}$. Note, however, that these features are halfway between the injection feature, or its oppositely shifted partner, and the central peak. This frequency is slightly less than the relaxation resonance frequency of the free-running laser. There is also a small frequency pushing of the central peak. At still higher injection levels, Figure 22(c) with $\xi^2 = 4 \times 10^{-4}$, the sub-harmonic resonance nature of the dynamics becomes clear. The sideband at the injection frequency is now dominated by the feature at half the offset. Also, the frequency pushing has stopped and the central peak is slightly pulled toward the injected frequency [10]. As

68
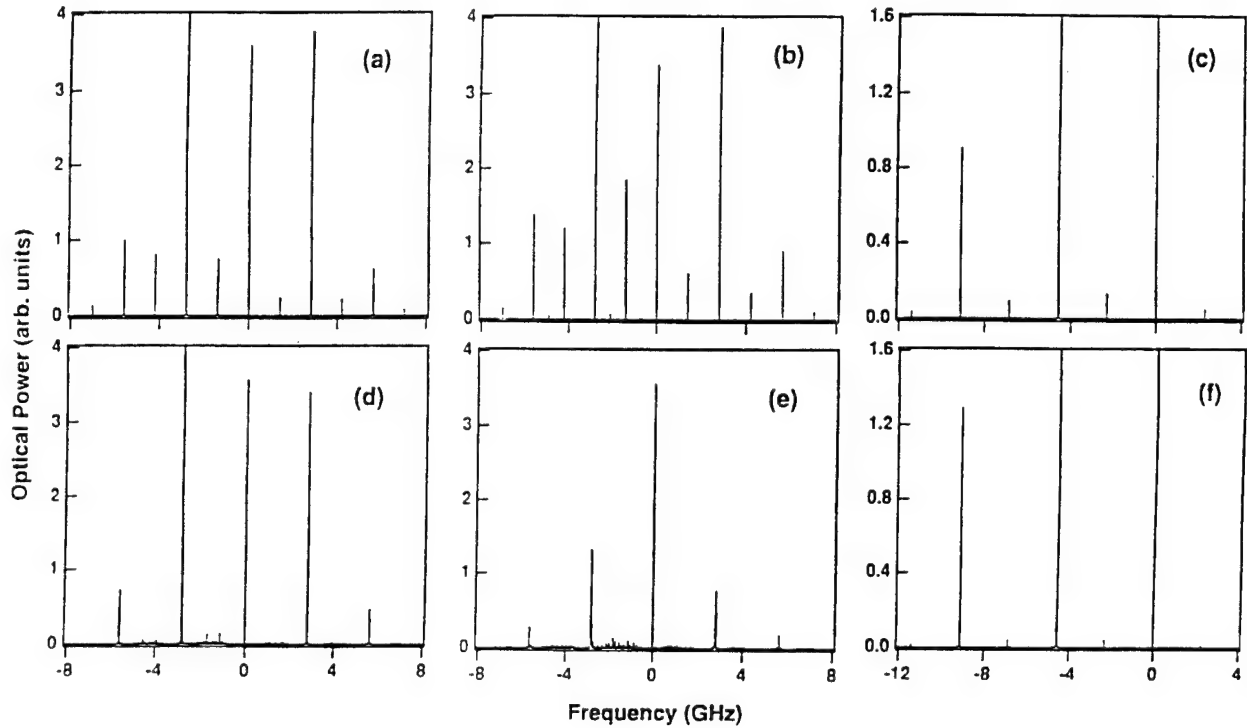
Figure 21: Computed optical spectra showing the effects of the spontaneous-emission noise at three levels of injection. (a) and (d) $\xi = 0.0145$, (b) and (e) $\xi = 0.0152$. (c) and (f) $\xi = 0.064$. (d)-(f) include the spontaneous-emission noise source term while the others do not. The strongest spectral feature in (a), (b), and (d), and the two strongest in (c) and (f) are clipped to emphasize the detailed features.
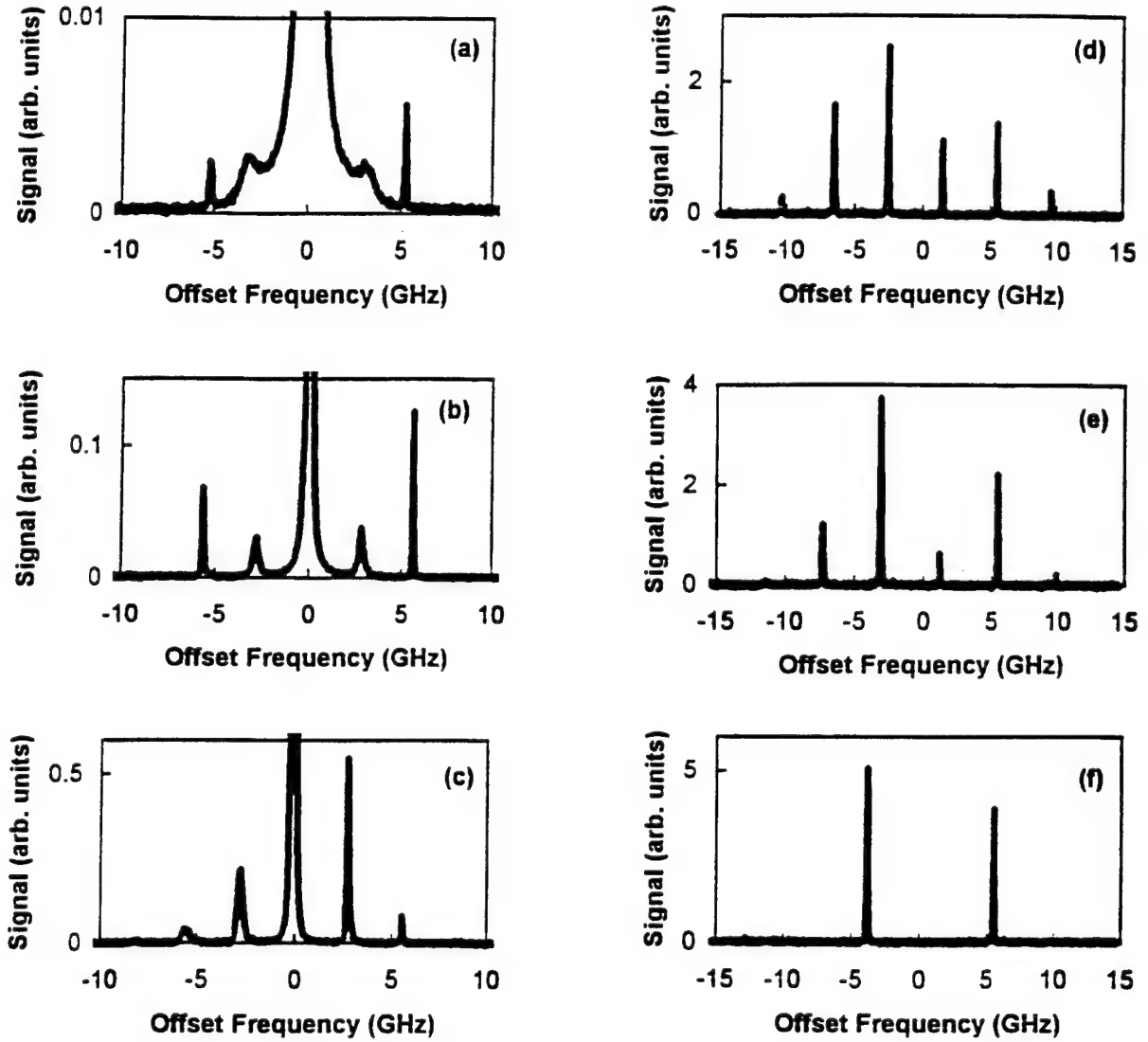
Figure 22: Measured optical spectra of the conventional, edge-emitting semiconductor laser with $\tilde{J} = 2/3$ under optical injection at a frequency offset ≈ 5.5 GHz: (a) weak injection with regenerative amplification and four-wave mixing sidebands. (b) enhanced subharmonic signal at $\xi^2 = 2.1 \times 10^{-4}$, (c) subharmonic resonance at $\xi^2 = 4 \times 10^{-4}$, (d) weak period quadrupling at $\xi^2 = 2.6 \times 10^{-3}$, (e) period doubling at $\xi^2 = 6 \times 10^{-3}$, and (f) limit cycle at $\xi^2 = 1.2 \times 10^{-2}$.

the injection level is increased to $\xi^2 = 2.6 \times 10^{-3}$, Figure 22(d), the pushing of the central peak and the dominance of the resonance frequency, now significantly larger than the initial offset freqency, are reestablished. This is actually a period-quadrupling spectrum, with weak, broadened features just discernible above the noise level in between the some of the sharp spectral features. At higher injection levels the spectrum follows the progression to period doubling, Figure 22(e) with $\xi^2 = 6 \times 10^{-3}$, and to limit cycle oscillations, Figure 22(f) with $\xi^2 = 1.2 \times 10^{-2}$. The frequency pushing continues to increase and the pushed feature gets relatively weaker. At very high injection levels, $\xi^2 > 3 - 4 \times 10^{-2}$, the laser output begins to smoothly shift to other longitudinal modes.

Using spectra like that of Figures 19 and 22, we have constructed a mapping of the dynamics for the laser at this pump level as the injection parameter and the frequency offset are varied. In the mapping of Figure 23, the frequency axis is relative to the free-running frequency of the injected laser. The map symbols are: 4 - perturbation spectrum with weak regenerative amplification and four-wave mixing sidebands; S - stable injection locking; SR - subharmonic resonance; P1 - limit cycle oscillation; P2 - period doubling; P4 - period quadrupling; Chaos - deterministic chaos; M' - multiwave mixing with most output on another longitudinal mode; hatched regions - principal output on another longitudinal mode; thin lines - smooth transition between dynamic regions; thick dotted lines - abrupt mode hop transitions with minor hysteresis; thick dashed lines with arrow - one way mode hops out of mode; thick solid lines - abrupt transition to/from a region of chaos or multiwave mixing where there is significant power in another longitudinal mode, from/to a region with power primarily in the principal mode. The smooth transitions represented by the thin lines are approximate. For instance, a peak-to-sideband ratio of 10:1 was used for the transition line from stable to unstable dynamics. For small values of ξ, the optical injection acts as a perturbation. Weak sidebands are generated at the offset frequency of the external optical injection and equally and oppositely shifted from the central peak. These are the regenerative amplification and four-wave mixing sidebands, respectively. As the injection parameter is increased, various dynamic instabilities develop. At negative detunings the locked region

71
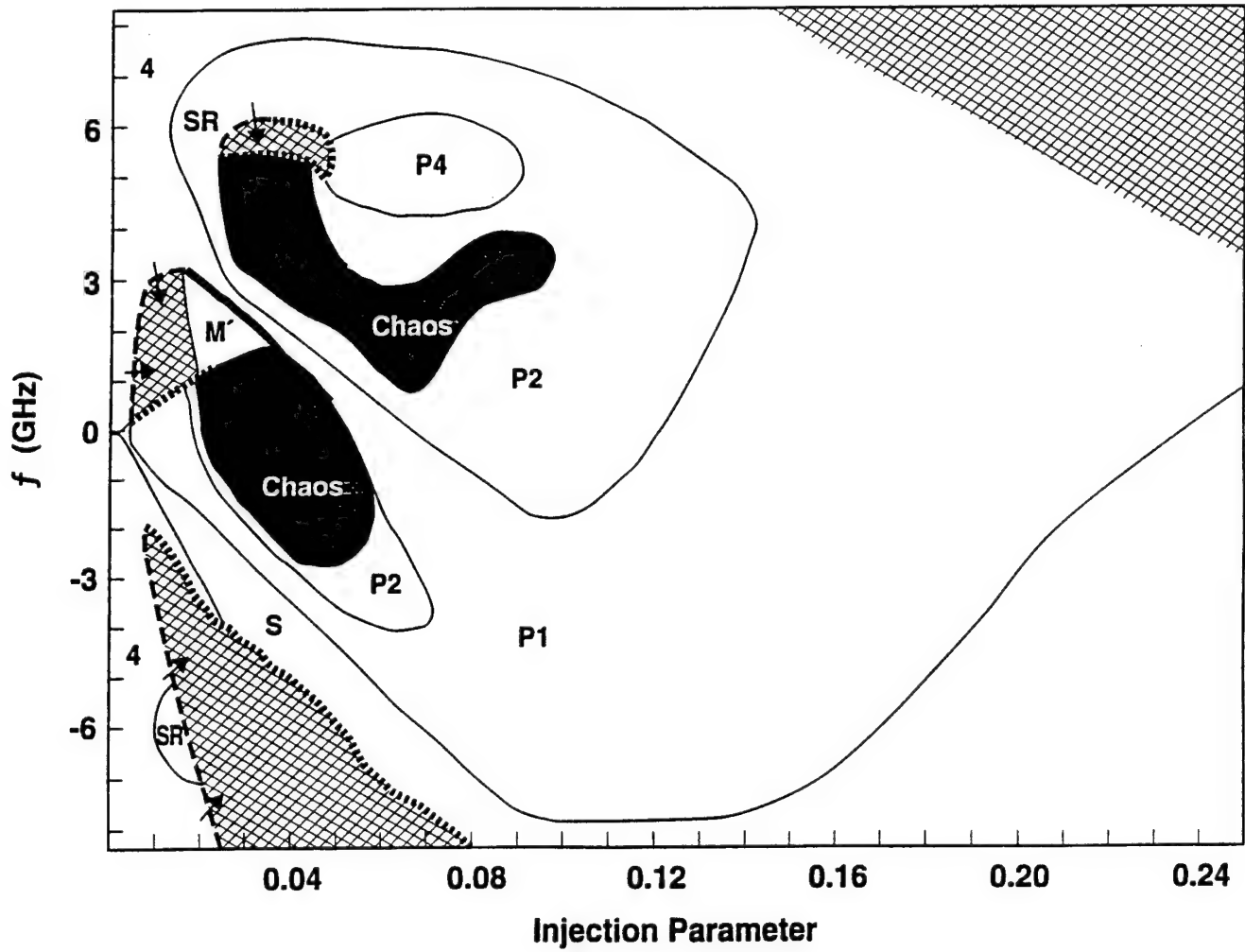
Figure 23: Mapping of the experimentally observed dynamic regions for a conventional edge-emitting semiconductor laser with $\tilde{J} = 2/3$. The dynamics are determined by comparison of observed spectra with calculated spectra with and without noise. Symbols are defined in the text.

resembles the predictions of the mapping from the linearized analysis. There is a narrow region of stable injection locking at lower values of ξ which opens up for $\xi \gtrsim 0.1$.

Most of the dynamic regions and transitions are directly recovered in the single-mode model of semiconductor laser operation. The value of the linewidth enhancement factor, b, is a critical parameter in determining the limits of the range of nonlinear dynamics and whether that range will include regions of chaotic dynamics. From the mapping it can be seen that the second region of period-doubling dynamics along the $\Omega = 0$ line is associated with a second region of chaotic dynamics at positive offset frequencies. The positive detuning region is more complicated because boundaries between different types of nonlinear dynamics are difficult to draw. For instance, when the offset is approximately equal to the free-running relaxation resonance frequency, the distinction between the perturbation, four-wave-mixing-type, spectrum and the limit-cycle spectrum blurs into one of qualitative difference. There are no clear features in the spectra which distinguish between locked and unlocked operation. The various unstable dynamics show no qualitative distinction as they cross the line where the linearized analysis divides locked and unlocked operation. Within the nominally locked operating regime, the various spectral features of the optical spectrum clearly show broadening with respect to the narrow feature at the injection frequency and are, therefore, not locked to the injection source.

Also associated with injection at positive offset frequencies is the general trend of frequency pushing of the originally free-running spectral feature. One anomaly of the subharmonic resonance is the slight pulling of the original oscillation peak in that region. For optical injection at positive offset frequencies, the excitation has a tendency to push the original oscillation peak to negative offset frequencies with the degree of pushing increasing as the offset frequency of the excitation is decreased or the injection parameter is increased. Figure 24 plots the frequency pushing for the injection offset at 5.5 GHz. More details of the weak frequency-pulling effect around the subharmonic resonance are given elsewhere [10]. Here, we concentrate on the general frequency-pushing trend. The pushing effect highlights a key point which is central to the asymmetry of the mapping. The external optical injection
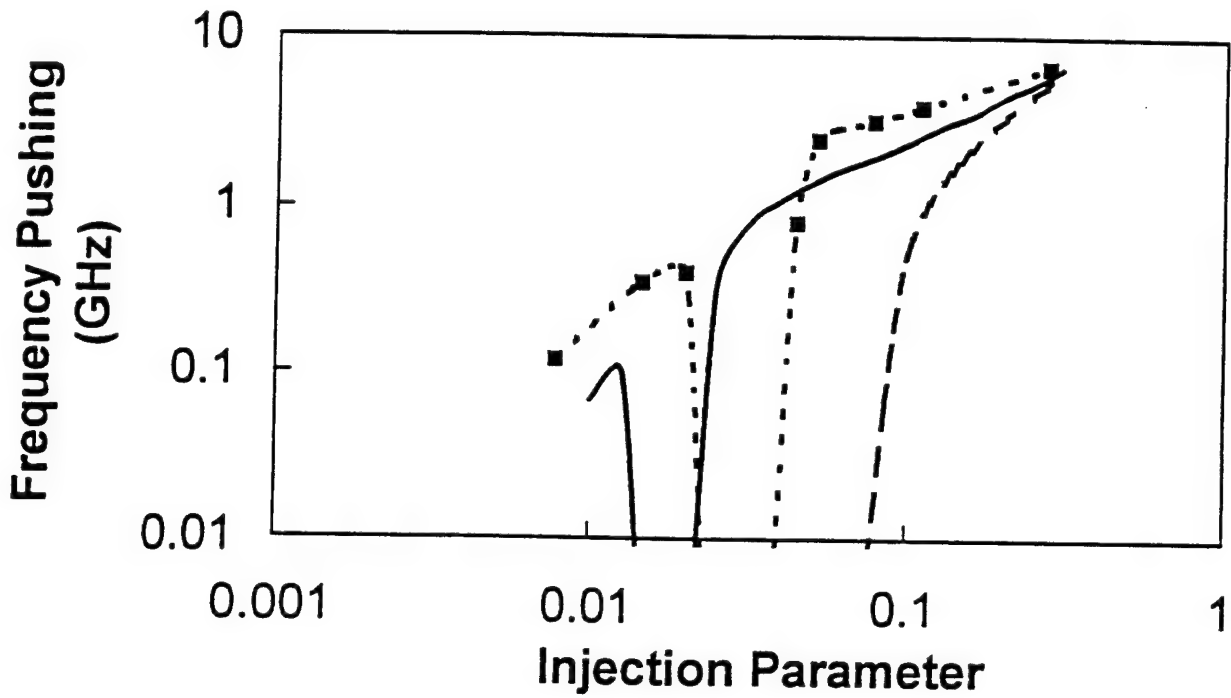
Figure 24: Frequency pushing of the initially free-running spectral feature as a function of injection with the master laser frequency offset by 5.5 GHz, experimental data - squares and dotted line, full nonlinear equations - solid line, eigenvalues of linearized equations - dashed line. Frequency pulling in the subharmonic resonance region causes the abrupt dip in the experimental data and nonlinear calculation curves.

shifts the Fabry-Perot oscillation frequency of the laser cavity by changing the steady-state carrier density. The excitation follows the new Fabry-Perot frequency along the zero phase offset line in the stable operating region. When the optical excitation is off of the Fabry-Perot resonance, there is a new frequency in the coupled field-carrier system. The shifting of the resonance oscillation frequency with excitation level is due to the competition between the original relaxation resonance, and its associated damping, and the frequency difference between the injected signal and this new resonance, and its associated phase offset, to control the response. The system restabilizes within the injection-locked operating region when the Fabry-Perot frequency shifts and associated damping are large compared to the original system resonances [12]. In this region of stable operation under strong injection, where linearized dynamics again prevail, the modulation characteristics of the semiconductor laser are strongly modified.

4.2 ENHANCED MODULATION BANDWIDTH AND REDUCED NOISE IN INJECTION-LOCKED SEMICONDUCTOR LASERS

Recently, several studies using conventional coupled-equation models have predicted that the modulation bandwidth of strongly injection-locked semiconductor lasers can be significantly improved relative to the free-running case [11, 12, 43, 37]. However, experimental work to date has only confirmed that the resonance frequencies of an injection-locked laser scale in accordance with the predictions of the model [12]. In a free-running semiconductor laser, the maximum current modulation bandwidth is set by the K-factor [44], $K = (2\pi)^2(\gamma_n + \gamma_p)/\Omega_r^2$, and $f_{max} = 2^{3/2}\pi/K$. Here, γ_n and γ_p are the decay rates due to stimulated emission and gain saturation, respectively, and $\Omega_r/2\pi$ is the relaxation resonance frequency, $\Omega_r^2 = \gamma_c\gamma_n + \gamma_s\gamma_p$, where γ_c is the photon decay rate from the laser cavity and γ_s is the free-carrier spontaneous decay rate. Because γ_n and γ_p are proportional to the circulating power in the laser cavity, f_{max} gives the limiting modulation bandwidth at high power levels. Here, we demonstrate that at accessible operating conditions an injection-locked laser can reach higher modulation bandwidths than f_{max} for the laser.

Semiconductor lasers have an asymmetric frequency range for injection-locked operation [19]. This is because a change in the free carrier density modifies both the gain and the refractive index. The change in the refractive index is related to the change in the gain by the linewidth enhancement factor, b. When the injected optical power is within a bounded range, typically from 10^{-4} to 10^{-2} of the output power, a sizeable fraction of the locked operating region displays unstable dynamics. However, for strong injection locking, at a level higher than 10^{-2}, stable dynamics again dominates the locked operating region and bandwidth enhancement has been calculated [12]. In regions of stable dynamics, a small-signal analysis is expected to be appropriate for calculating the modulation characteristics due to a weak optical probe or current modulation. A weak optical probe at a frequency offset from the locked operating frequency generates a regenerative amplification sideband at the probe frequency. When there is no optical feedback into the slave laser, the small-signal regenerative amplification spectrum is given by [12]:

$$\frac{|A_r|^2}{|A_i|^2} = \frac{\eta^2}{|D|^2}\{[-\Omega^2 + (V + b\gamma_{pL}/2)\Omega + \Omega_L^2/2 + (\gamma_s + \gamma_{nL})2U/2]^2$$

$$+[-\Omega(\gamma_{rL} - \gamma_{pL}/2) + V(\gamma_s + \gamma_{nL}) + b\Omega_L^2/2]^2\}. \tag{79}$$

Here, A_r and A_i are the amplitudes of the regenerative amplification sideband and the injected probe, respectively, η is the coupling parameter for external fields into the laser, and $\Omega/2\pi$ is the offset between the probe frequency and the operating frequency injection-locked laser. Injection locking shifts the operating point of the complex gain as described by $\gamma_{nL} = \gamma_n a_L^2$, $\gamma_{pL} = \gamma_p a_L^2$, $U = (\eta/\gamma_c)a_L \cos(\phi_L)$ and $V = (\eta/\gamma_c)a_L \sin(\phi_L)$, where $a_L = |A_L|/|A_0|$ is the ratio of the locked to free-running field amplitudes and ϕ_L is the phase offset between the circulating and injected fields. Also, $\Omega_L^2 = (\gamma_c - 2U)\gamma_{nL} + \gamma_s\gamma_{pL}$ and

$$D = (-i\Omega + U)[-\Omega^2 + \Omega_L^2 + (\gamma_s + \gamma_{nL})U - i\Omega\gamma_{rL}]$$

$$+(\Omega_L^2 - i\Omega\gamma_{pL})bV + (-i\Omega + \gamma_s + \gamma_{nL})V^2, \tag{80}$$

where $\gamma_{rL} = \gamma_s + \gamma_{nL} + \gamma_{pL} + U$. Note that we write $2U/2$ for one term in Equation 79 because the factor of 2 in the denominator was incorrectly included in Equation 47 of Reference [12]. Similarly, the amplitude modulation spectrum due to a weak current modulation that would

76

be measured by direct detection of the injection-locked laser output is described by [12, 37, 43]:

$$|\hat{\sigma}|^2 \propto \frac{[\Omega^2 + (U + bV)^2](\gamma_c - 2U)^2\gamma_{nL}^2}{|D|^2} \tag{81}$$

where $\hat{\sigma}$ is the complex amplitude modulation coefficient. Fitting the regenerative amplification spectrum determines all of the parameters needed to calculate the parasitic-free amplitude modulation characteristic due to a weak current modulation.

The strength of the signal from the master laser is given by the injection parameter, $\xi = (\eta/\gamma_c)a_L$, which can be experimentally determined [8]. The injected power is proportional to ξ^2. Figure 25 shows the regenerative amplification spectra for the free-running laser and for three different operating points when the laser is injection locked at the highest injection level we could achieve, $\xi = 0.4 \pm 0.1$. The frequency axis is with respect to the free-running frequency of the slave laser. The signal axis is relative to the system noise level. Changing the offset frequency of the master laser with respect to the free-running slave laser modifies the regenerative amplification characteristic of the injection-locked laser. Detunings of the master laser of 0, -4.8 and -9.7 GHz are shown. Each of the injection-locked laser spectra contains a narrow peak at the injection frequency corresponding to the injection-locked peak. It is not part of the true modulation spectrum. Along with the experimental data, calculated spectra are shown using the experimentally determined parameters. For the calculations, the overall signal level is a free parameter. It was adjusted to match the free-running data. The injection parameter was fixed at $\xi = 0.4$. The value of the linewidth enhancement factor was then adjusted, within its allowable range, to give a good fit for the frequency offset of the resonance peak in the zero detuning data yielding $b = 5.4$. The amplitude of the signal is no longer a free parameter for these data. There are then no free parameters for the fitting of the detuned injection spectra. Note that the injection-locked laser spectra are strongly asymmetric, reflecting the shift of the Fabry-Perot cavity resonance frequency under the optical injection [12].

77
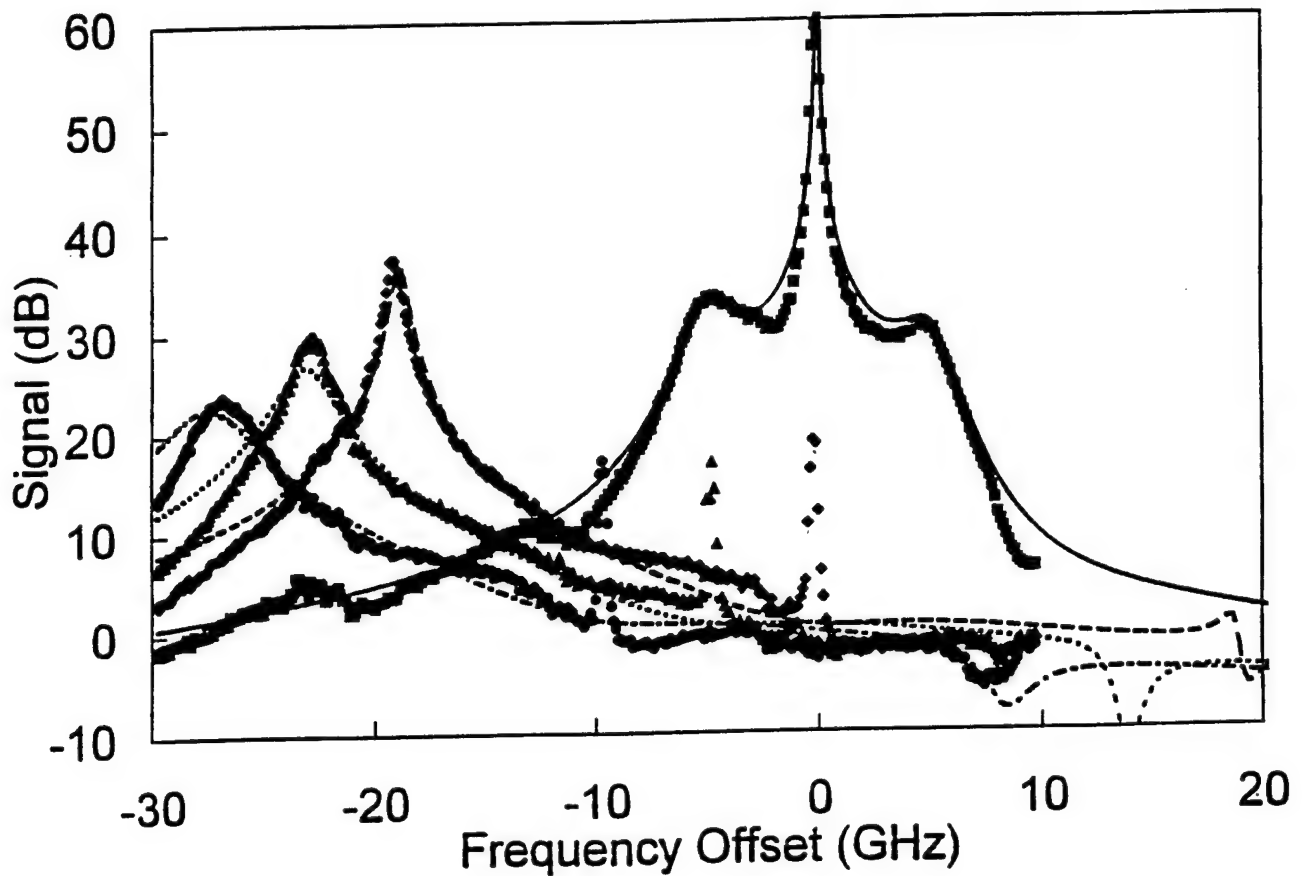
Figure 25: Spectra of the regenerative amplification sideband due to a weak optical probe under four different operating conditions. The frequency axis is relative to the free-running frequency of the slave laser and the signal axis is relative to the noise level of the measurement system. Solid symbols are experimental data and curves are calculated spectra using the experimentally determined dynamic parameters and Equation 52. Solid Line and Squares - Free-running laser, Dashed Line and Diamonds - Injection locking at the free-running frequency, Dotted Line and Triangles - Injection locking offset at −4.8 GHz, Dot-dashed Line and Ovals - Injection locking offset at −9.7 GHz.

The good agreement between the measured and calculated spectra allows us to calculate the amplitude modulation spectra due to a small oscillating current when the laser is at the operating point corresponding to the four regenerative amplification spectra. The calculated spectra, normalized to the zero-frequency signal level, are plotted in Figure 26. The free-running laser shows the characteristic relaxation resonance peak in the spectrum. The modulation spectra of the injection-locked laser all show a slight dip before a shifted resonance peak. Based on the deviation between the calculated and measured spectra for the detuned injection locking, the calculated curves slightly overestimate the resonance frequency and underestimate the width of the resonance peak of these two spectra. For the laser under investigation, $f_{max} = 19.3$ GHz, a value higher than can be practically achieved due to constraints on the injection current level. All three injection-locked modulation curves have 3-dB rolloff frequencies higher than f_{max}.

The dip in the current modulation characteristic highlights the fact that, in the strong injection limit, the spectrum is made up of two resonances [12]. The zero-frequency resonance has a damping corresponding primarily to the field-enhanced free-carrier decay rate, $\gamma_s + \gamma_{nL}$. The circulating power increases as the detuning becomes more negative within the injection-locked operating region, decreasing the size of the dip. The non-zero resonance corresponds to the offset of the shifted Fabry-Perot resonance frequency with respect to the injection-locked peak. In the large injection limit, the offset is largely determined by V, with associated damping determined by U. As the detuning of the master laser becomes more negative, ϕ_L decreases towards zero in the injection-locked region. This explains the combined decrease in the resonance frequency and increase in the damping rate.

In the design of high-speed semiconductor lasers, great attention is paid to decreasing the values of b and γ_p [26]. In the injection-locked case, this is not as important. The value of b needs to be kept low to minimize the frequency chirp. However, under strong injection locking, it has recently been shown that the frequency chirp is greatly reduced in the bandwidth-enhanced operating region [37]. Also, increasing b increases the frequency shift of the Fabry-Perot resonance, all other parameters being unchanged. Decreasing γ_p yields an
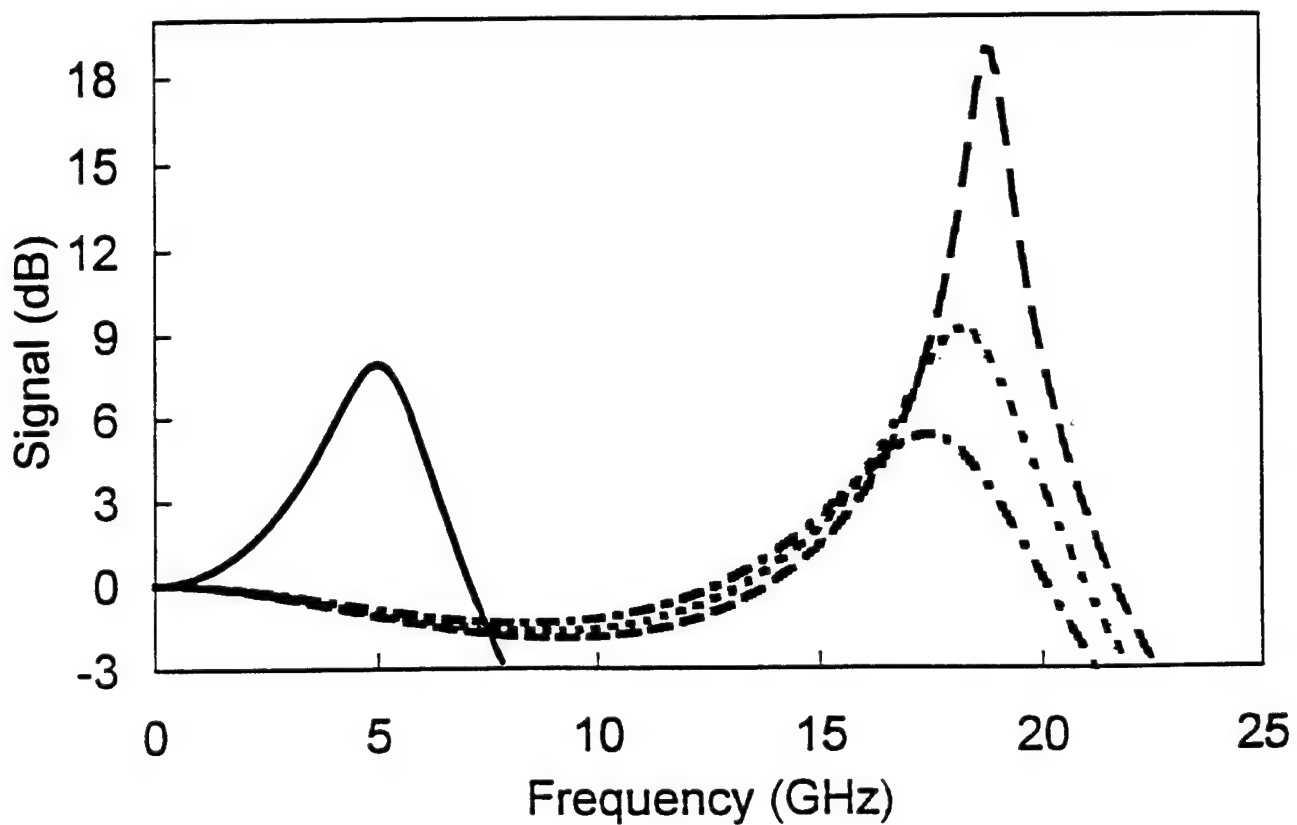
Figure 26: Calculated amplitude modulation spectra due to a weak current modulation corresponding to the regenerative amplification spectra plotted in Figure 25. All curves are normalized to the signal at zero frequency offset. Solid Line - Free-running, Dashed Line - Injection locking at the free-running frequency, Dotted Line - Injection locking offset at −4.8 GHz. Dot-dashed Line - Injection locking offset at −9.7 GHz.

increased f_{max} through the K-factor. However, the K-factor does not apply to the injection-locked laser. Under injection locking, increasing γ_p has the principal effect of increasing the damping rates of the charactersitic resonances. Therefore, it can actually enhance the useful operating range of the system.

We have shown that parasitic-free modulation bandwidths in excess of 20 GHz, and in excess of the K-factor limit, can be achieved in relatively low cost, commercially available lasers by using strong injection locking. The bandwidth enhancement relative to the free-running case was approximately a factor of three. Factors of 2-3 improvement in bandwidth are calculated to be achievable in a wide range of laser diodes, and parasitic-free bandwidths in excess of 60 GHz appear to be feasible with high-speed lasers.

We have previously described how the noise spectra of a laser diode can be understood in terms of the external injection model in the weak injection limit [15]. This analysis was then extended to the case of the injection-locked laser to understand changes in the amplitude noise spectrum [11]. Specifically, data was taken of the injection-locked laser when the offset frequency is changed to maintain the $\phi_L = 0$ condition. In the previous publication, the injection-locked data showed only qualitative agreement with calculated spectra. The discrepancy was largely due to improperly accounting for the increased circulating power under injection locking in the previously calculated spectra. Figure 27 replots the previously published data of the noise amplitude spectra. It compares the data with properly scaled calculated spectra using the linearized analysis and full nonlinear calculations. There is now good agreement between calculated and measured spectra. As long as the laser is not biased too close to the threshold for laser oscillation, $\tilde{J} = 0$, then the noise can be considered a linear perturbation and the noise improvements calculated above are recovered experimentally.

4.3 FEEDBACK EFFECTS ON MODULATION SPECTRA IN INJECTION-LOCKED SEMICONDUCTOR LASERS

During the course of our experimental investigations on bandwidth enhancement in injection-locked laser diodes, we found that we observed spectra which could not be fully explained

81
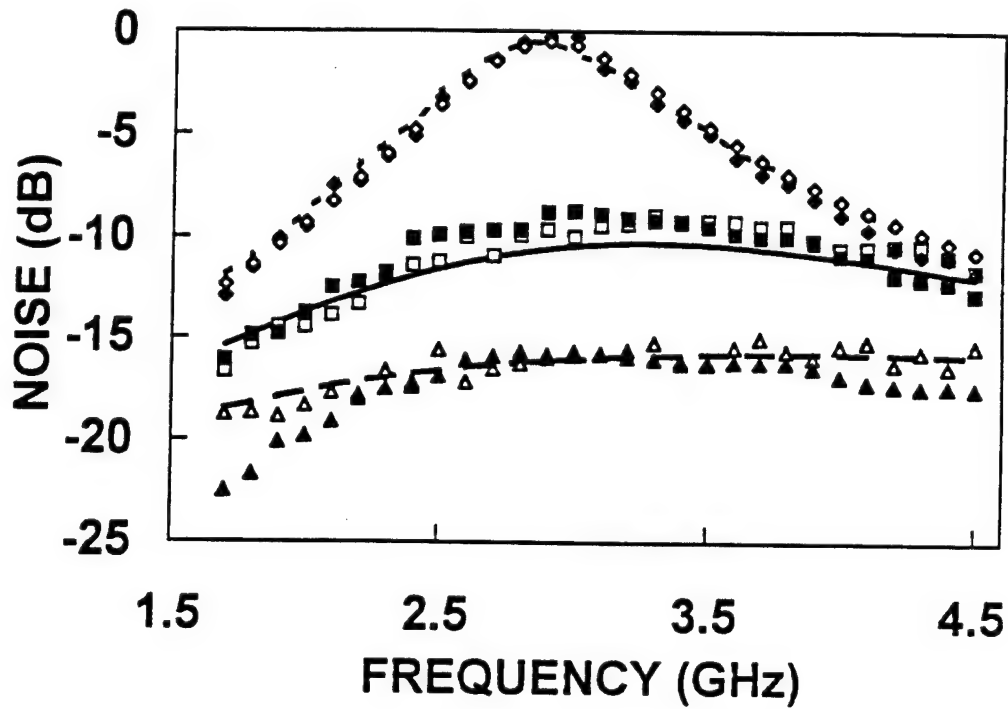
Figure 27: Changes in the amplitude noise spectrum of a quantum-well laser diode, where the dominant noise source is spontaneous emission, due to stable injection locking by an external laser. The experimental data, solid symbols, are for the detuning that minimized the amplitude of the noise spectrum. Two different calculated spectra are shown. The open symbols are the calculated spectra using the full nonlinear coupled equations that minimized the noise spectrum. The curves are the calculated spectra at the different injection levels for the offset frequency where $\phi_L = 0$. Dotted Line and Diamonds - $\xi = 0$, Solid Line and Squares - $\xi = .06$, Dashed Line and Triangles - $\xi = .2$.

without including feedback into the slave laser cavity from its collimating lens. We have already described how the lens and laser surfaces formed a weak cavity for the linear probe laser. Here, we discuss the effects of the feedback on our experimentally observed spectra using the expanded model for laser diode operation, with the effects of feedback included, that was described above. These formulas are appropriate when the external optical injection is sufficiently strong to induce stable, injection-locked operation and the feedback is not so strong that it destabilizes the injection-locked operating point.

When there is feedback into an injection-locked laser, there is a shift in the phase, ϕ_L, and normalized amplitude, a_L, of the output field as described by Equations 14-16. These changes will be reflected in the offset frequency and damping characteristics of the resonance associated with the shifted cavity Fabry-Perot resonance frequency. Depending upon the phase of the feedback signal due to the round-trip delay, the damping can be either enhanced or reduced. The effects of feedback are further reflected in the modulation characteristics with the additional etaloning associated with the feedback cavity.

The effects of feedback can be clearly seen in the regenerative amplification spectra of Figure 28 and amplitude modulation spectra of Figure 29. The experimental data was taken with the laser subject to an injection level of $\xi = 0.2 \pm 0.05$ and the master laser was offset from the free-running frequency of the slave laser by -22 GHz. Two calculated spectra, with and without feedback, are shown in each figure. In Figure 28 they are calculated from Equation 52 and in Figure 29 from Equation 54. The calculated spectra used $\xi = 0.225$ and the strength and phase shift of the feedback was adjusted to give a good fit to the data. The calculated spectra with feedback used $r = 0.055$ and $\arccos(\omega_L \tau) = 2.945$, nearly out of phase with the externally injected signal. The other parameters were the same as for the data above which did not show the feedback. The optical power which is fed back into the cavity is approximately an order of magnitude less than the injected signal and, from a realistic applications point of view, represents fairly strong undesired feedback.
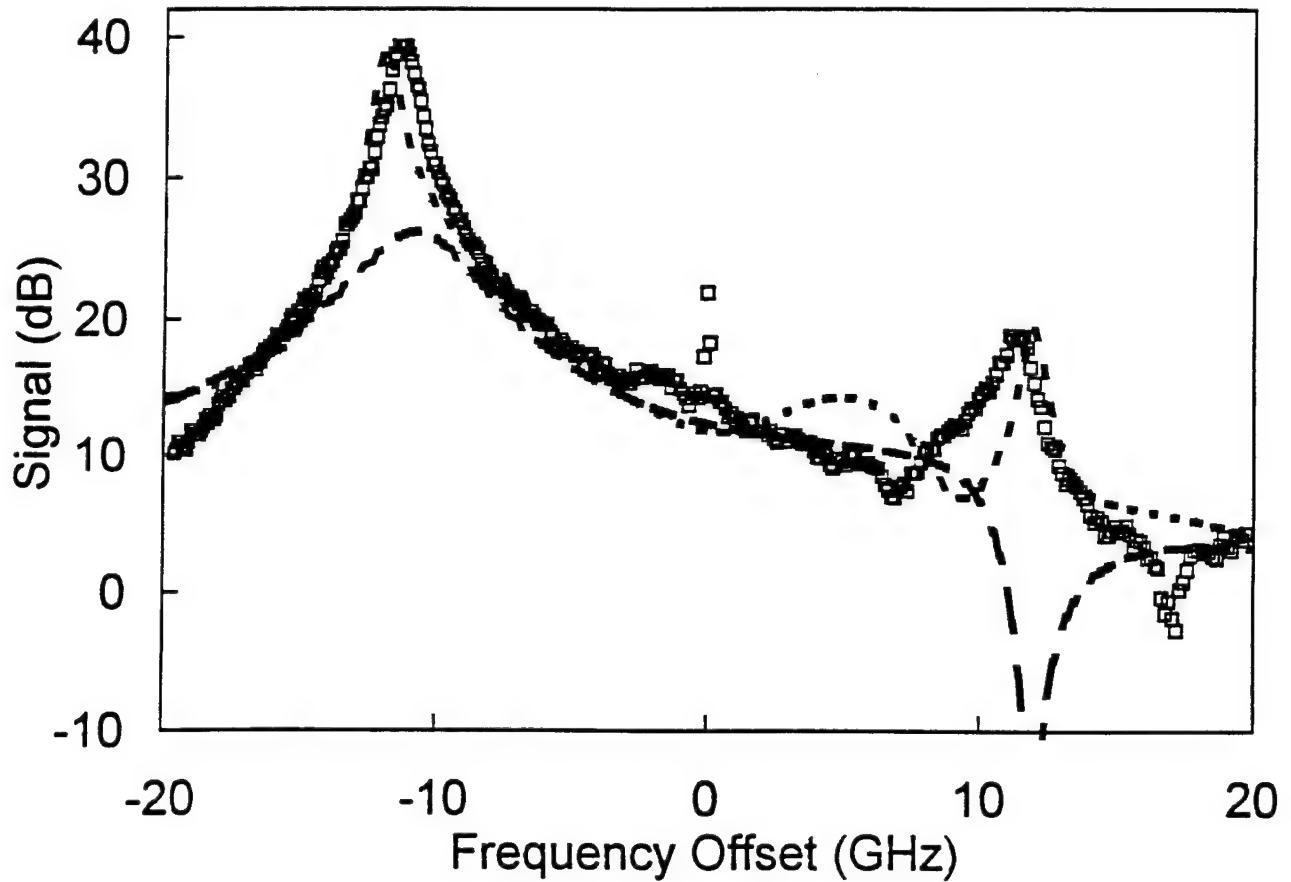
Figure 28: Spectra of the regenerative amplification sideband due to a weak optical probe showing the effects of feedback on an injection-locked laser. The frequency axis is relative to the injection-locked operating frequency which is shifted from the free-running frequency of the slave laser by -22 GHz. The signal axis is relative to the noise level of the measurement system. Open symbols are experimental data and curves are calculated spectra using the experimentally determined dynamic parameters and Equation 52. The injection level is $\xi = 0.225$ with, Dashed Curve- feedback amplitude is $r = 0$, and Dotted Curve - feedback amplitude is $r = 0.055$ and phase is $\arccos(\omega_L \tau) = 2.945$.

Figure 29: Spectra of the amplitude modulation due to a weak optical probe showing the effects of feedback on an injection-locked laser. The frequency axis is relative to the injection-locked operating frequency which is shifted from the free-running frequency of the slave laser by -22 GHz. The signal axis is relative to the noise level of the measurement system. Open symbols are experimental data and curves are calculated spectra using the experimentally determined dynamic parameters and Equation 52. The injection level is $\xi = 0.225$ with, Dashed Curve- feedback amplitude is $r = 0$, and Dotted Curve - feedback amplitude is $r = 0.055$ and phase is $\arccos(\omega_L \tau) = 2.945$.

As further examples of the effects feedback can have on the modulation spectra, we show calculated regenerative amplification and current modulation induced amplitude modulation spectra. The calculations compare spectra which use parameters relevant to the data described above with spectra where either the amplitude or the phase of the feedback has been changed. Figures 30 and 31 show that when the phase or amplitude of the feedback are adjusted, one can observe both enhanced and reduced stability of the shifted resonance peak. The curve with the phase shifted by π corresponds to feedback close to being in phase with the externally injected signal. Such feedback can diminish the magnitude of the resonance peak rather than enhance it. When the feedback is approximately out of phase with the injected signal, as was the case with the experimental data, an increase in the feedback enhances the magnitude of the resonance peak.

To a reasonable approximation, the effects of feedback at this level are the same as changing the strength and frequency offset of the injected optical signal. Indeed, the data could be adequately fit using the feedback-free formulas of Reference [12] with injection parameters and frequency offsets that did not match the experimental conditions. If one operates too close to the stability/instability boundary of injection-locked operation, feedback can cause a nominally stable system to undergo amplitude and phase oscillations at the resonance frequency. Therefore, as long as one operates well within the unconditionally stable operating region and the feedback level is not too high, feedback will not preclude the bandwidth enhancement and improved modulation characteristics.

4.4 VCSEL ABOVE THRESHOLD

The effects of optical injection on the optical spectrum of a VCSEL are shown in Figure 32. For these spectra, the VCSEL was operated at a bias current of 6 mA. Again, zero frequency corresponds to the free-running optical frequency of the VCSEL. The master laser was also tuned to this frequency for this series of spectra. At this injection current level, there is some output power in higher order spatial modes which are spectrally offset from the region shown. Optical injection at the free-running frequency of the dominant, lowest order spatial mode,
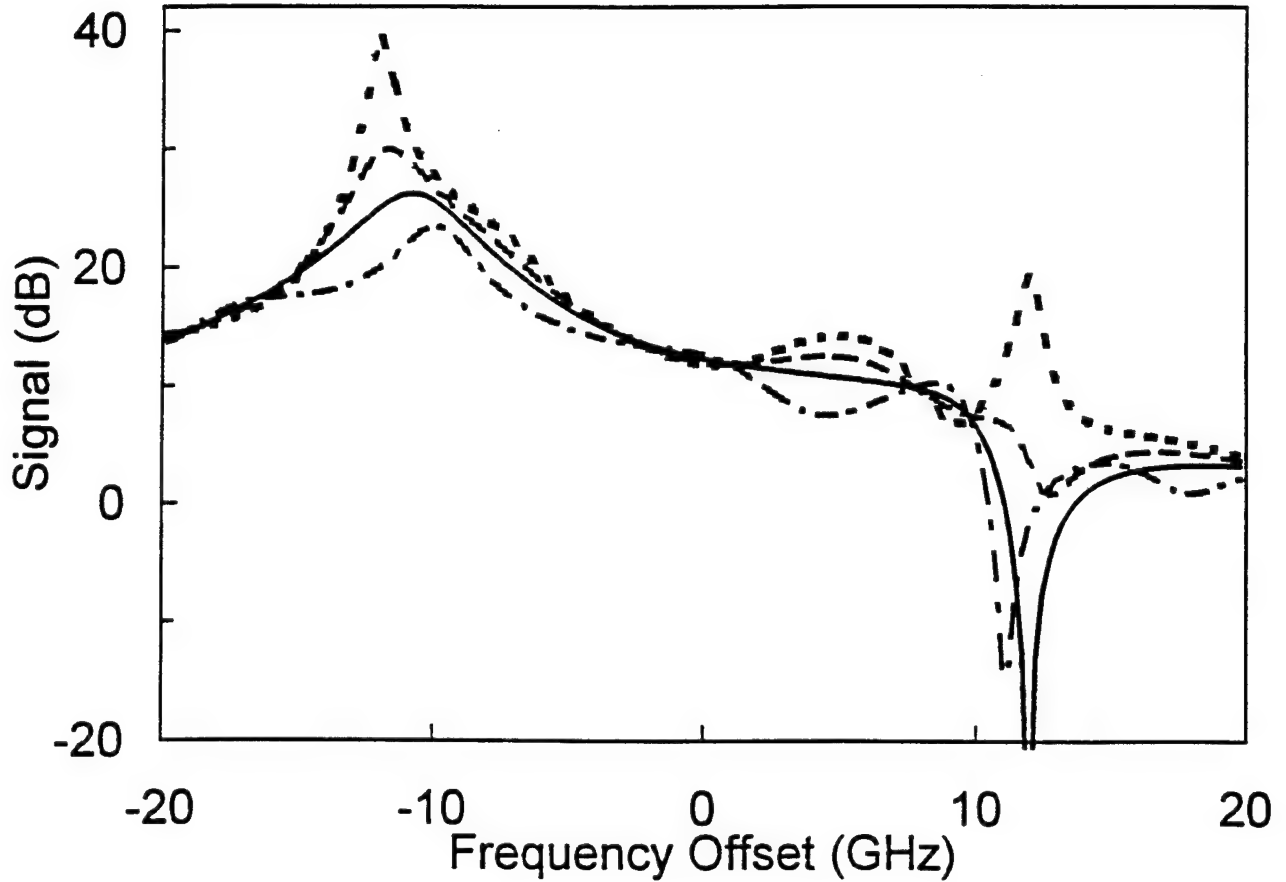
Figure 30: Spectra of the regenerative amplification sideband characteristic due to a weak optical modulation. showing the effects of optical feedback. The frequency offset is with respect to the free-running optical frequency. The dotted and solid lines correspond to the calculated curves of Figure 28 with and without feedback, respectively. The dashed curve is for the feedback amplitude reduced to $r = 0.0275$ and the phase of the feedback unchanged at $\arccos(\omega_L \tau) = 2.945$ while the dot-dashed curve is for the amplitude of the feedback unchanged at $r = 0.055$ and the phase shifted by π to $\arccos(\omega_L \tau) = 6.087$.
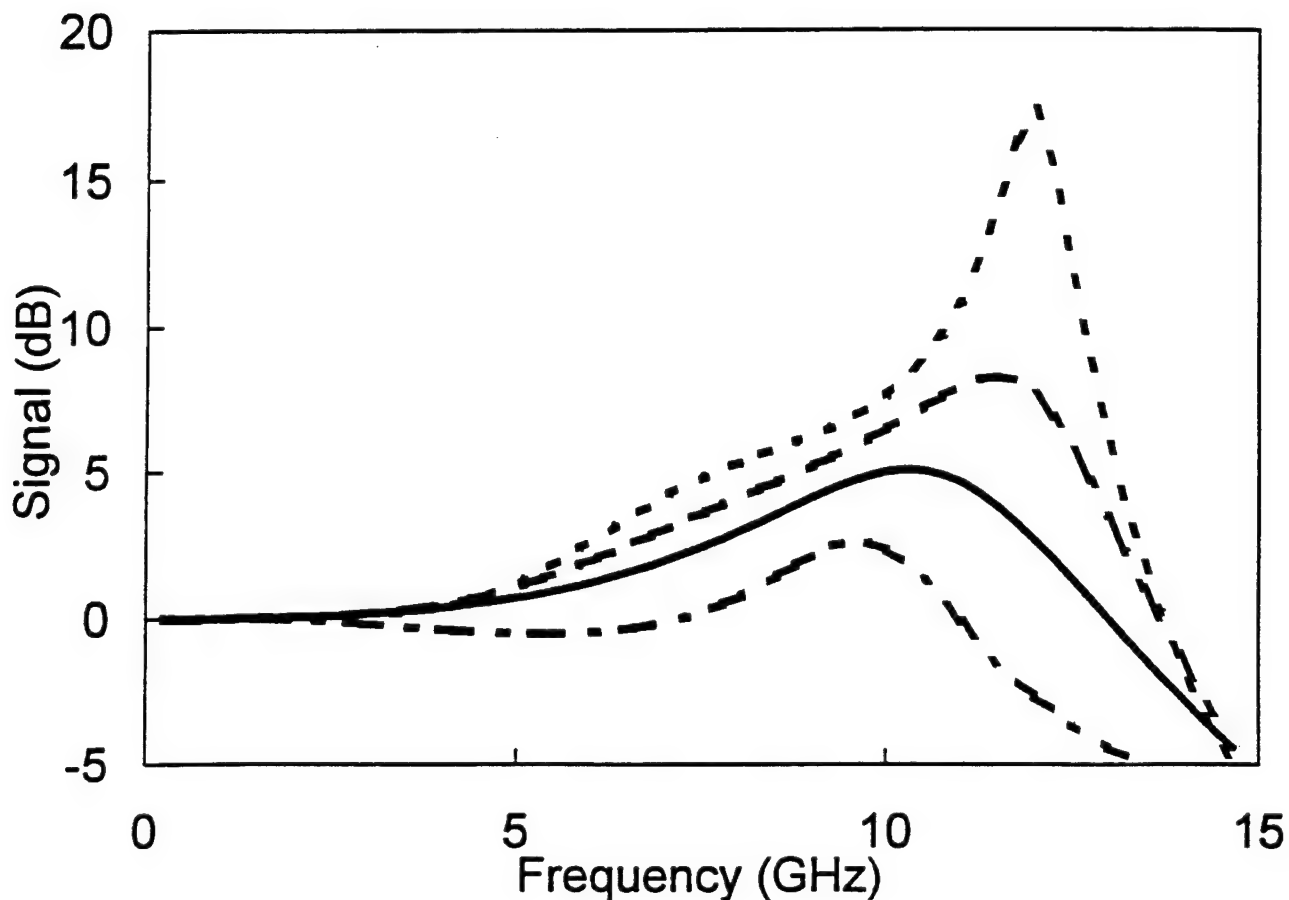
Figure 31: Spectra of the amplitude modulation characteristic due to a weak current modulation. The dotted and solid lines use the same parameters as the calculated curves of Figures 28 and 29 with and without feedback, respectively. The dashed curve is for the feedback amplitude reduced to $r = 0.0275$ and the phase of the feedback unchanged at $\arccos(\omega_L \tau) = 2.945$ while the dot-dashed curve is for the amplitude of the feedback unchanged at $r = 0.055$ and the phase shifted by π to $\arccos(\omega_L \tau) = 6.087$.
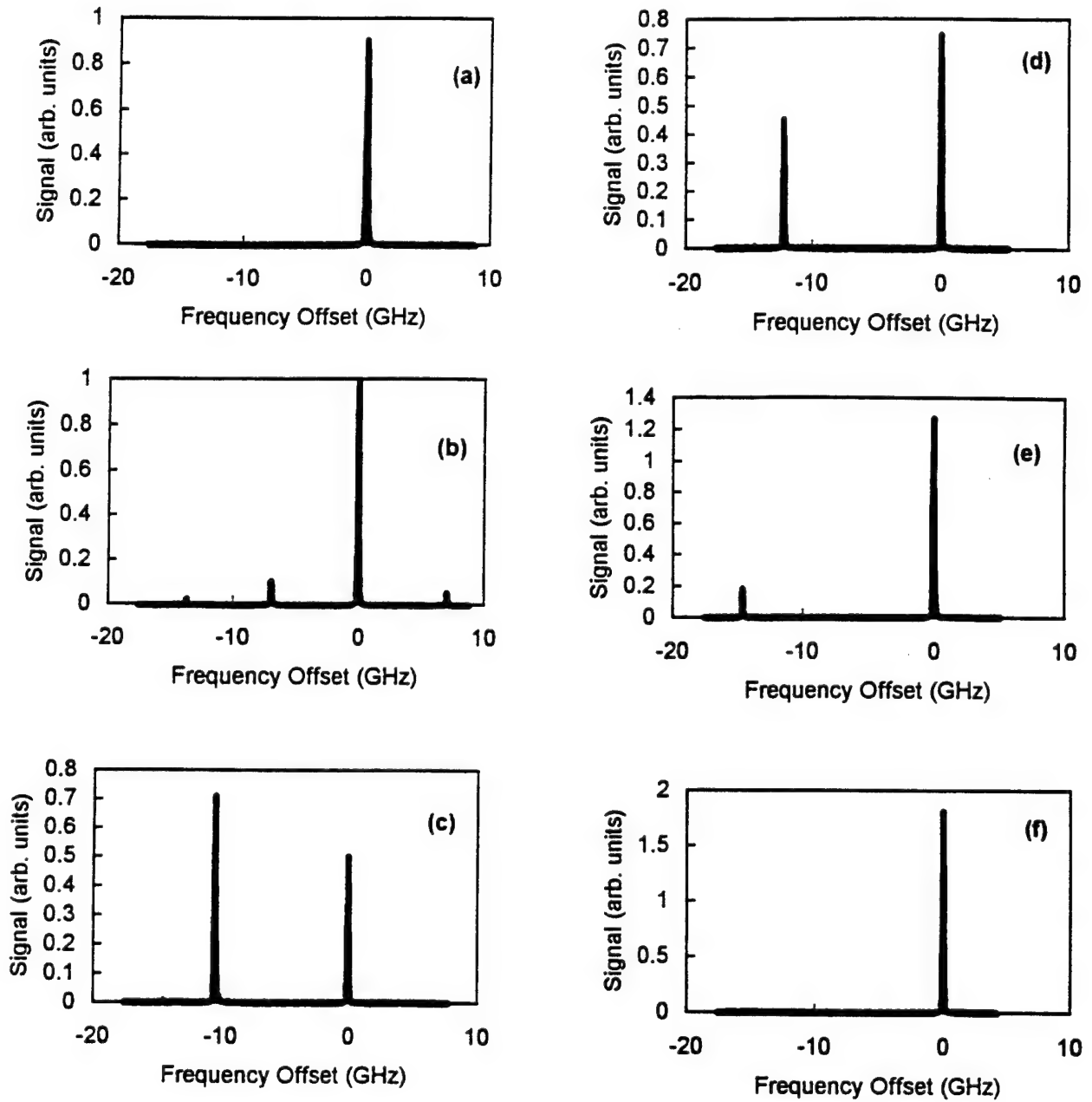
Figure 32: Measured optical spectra of the VCSEL with $\tilde{J} = 0.9$ under optical injection at the free-running frequency. The frequency axis is referenced to the free-running frequency of the VCSEL. The injection conditions are: (a) free-running and relative injection power levels of, in arbitrary units (b) 0.045, (c) 0.234, (d) 0.441, (e) 0.907, and (f) 1.536 where the laser has reestablished stable operation.

the case shown here, leads to a decrease in the power in the higher order modes. However, it did not fully quench this emission. The set of spectra in Figure 32 show an initially free-running laser, 32(a), which undergoes a Hopf bifurcation to a dynamically unstable state as the injection level is increased, 32(b). The resonance frequency monotonically increases as the injection level increases, 32(c)-32(e). Finally, the laser reestablishes stable dynamics at very high injection levels, 32(f). The progression is similar to the one previously observed. The laser did not show period doubling and a transition to chaotic dynamics because the linewidth enhancement factor had a relatively low value, $b = 2$-3. Earlier data taken when the laser displayed a larger linewidth enhancement factor clearly displayed the transition to chaos. All of these features are consistent with the dynamics expected from the coupled equation model.

The increase in the resonance frequency as a function of the injection level is shown in Figure 33. Here, the resonance frequency again shows the nearly linear dependence with the injection parameter seen in the earlier data on the conventional, edge-emitting laser. We have previously shown that this dependence falls to two-thirds power, cube root of the injected power, when the injected power becomes large compared to the free-running output power [41]. Both of these results follow from the coupled equation model [12]. The spectra in Figures 32(c)-(e) show that there are two dominant components of the optical spectrum as the resonance frequency varies over a significant range of microwave frequencies. The beating of these two optical components leads to a strong microwave signal upon conventional detection of the optical beam. This tunability is achieved by changing the injected power from a constant output power optical beam without the requirement for any high-speed electrical imput. The tuning range shown in Figure 33 should not be taken as a performance limit for VCSELs in general or even the VCSEL under study. Others have observed the changing resonance frequency in VCSELs to be as large as 60 GHz [45].

Referring back to the mapping of the conventional, edge-emitting laser, Figure 23, some features of the mapping reflect specific characteristics of the laser under investigation, a conventional, edge-emitting, Fabry-Perot laser diode, where the oscillating mode is always
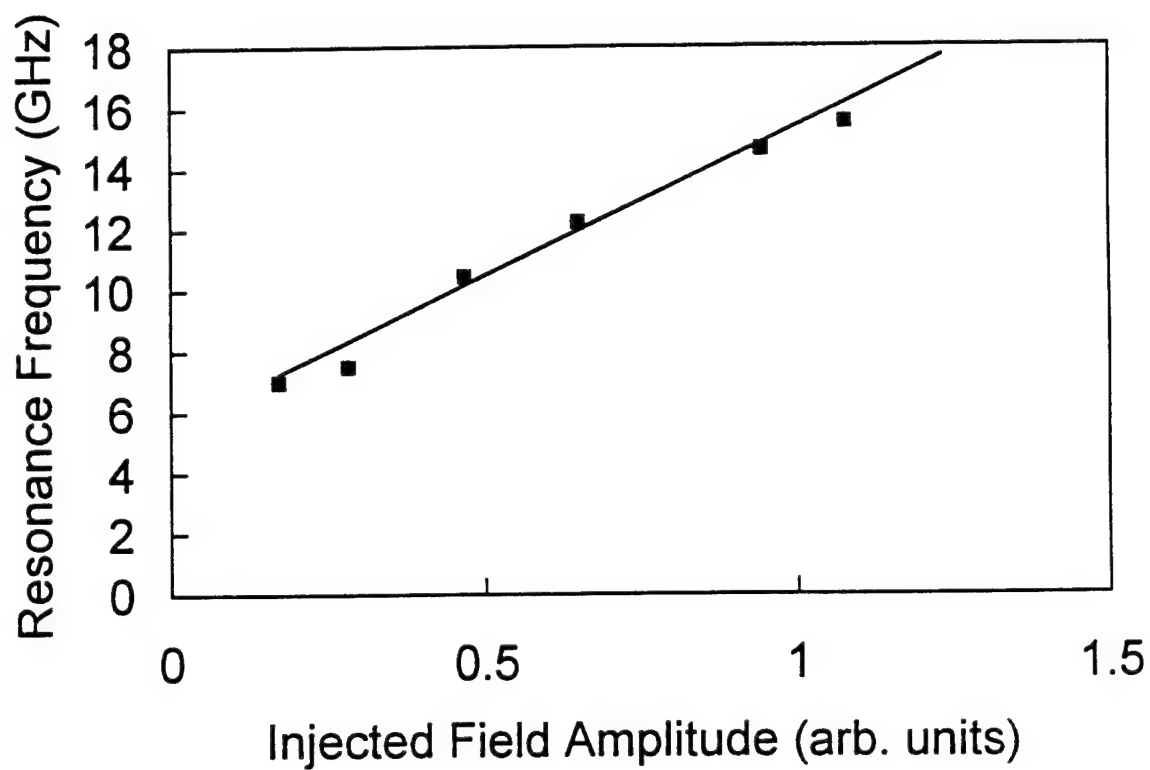
Figure 33: Variation of the resonance frequency of the VCSEL under external optical injection as a function of the square root of the injection power. The squares are the experimental data and the solid line is a visual aid.

in competition with other longitudinal modes which are close to threshold. Because of this, the external optical signal can induce a mode hop and certain regions of the detuning-injection plane become inaccessible. There is an abrupt mode hop near the locking-unlocking boundary which has a small hysteresis, not shown, associated with it. For larger offsets, some of the mode hops are one way and the laser does not reestablish operation on the original longitudinal mode at this boundary. At negative offsets there is a bounded range of unstable dynamics which follows a period-doubling progression, largely obscured by noise, to chaotic dynamics. Within the range of chaotic dynamics a varying fraction of the optical output begins to shift to other modes. One edge of the region of chaotic dynamics is an abrupt transition where power returns to the original longitudinal mode as the laser returns to oscillatory dynamics. Again there is a small hysteresis, not shown, associated with this transition.

Because the longitudinal modes in a VCSEL have such a large frequency spacing, only one is resonant with the high-reflectivity mirrors that define the laser cavity. Therefore, the VCSEL should not show these mode hops and we did not observe them. In addition, it should be able to show the locking/unlocking bistability that was apparently masked in the other laser by the mode hop. The bistability could be observed. Figure 34 shows a set of spectra taken with the bias current to the VCSEL set at 6 mA and the detuning of the master laser varied while the injection level was held constant. When the master laser frequency offset is shifted to negative values away from the free-running slave frequency, the laser remains locked until the detuning is beyond −12 GHz. However, when the detuning shift is then reversed, locking is not reestablished until −10.8 GHz. Between −12 and −10.8 GHz the laser displays the locking/unlocking bistability.

4.5 VCSEL POLARIZATION AND NOISE CHARACTERISTICS

The fact that the VCSEL has two nearly degenerate, orthogonally polarized modes can complicate the interpretation of the laser spectra. Even when the output power of one polarization dominates the other by a factor of 100, the influence of the weak polarization
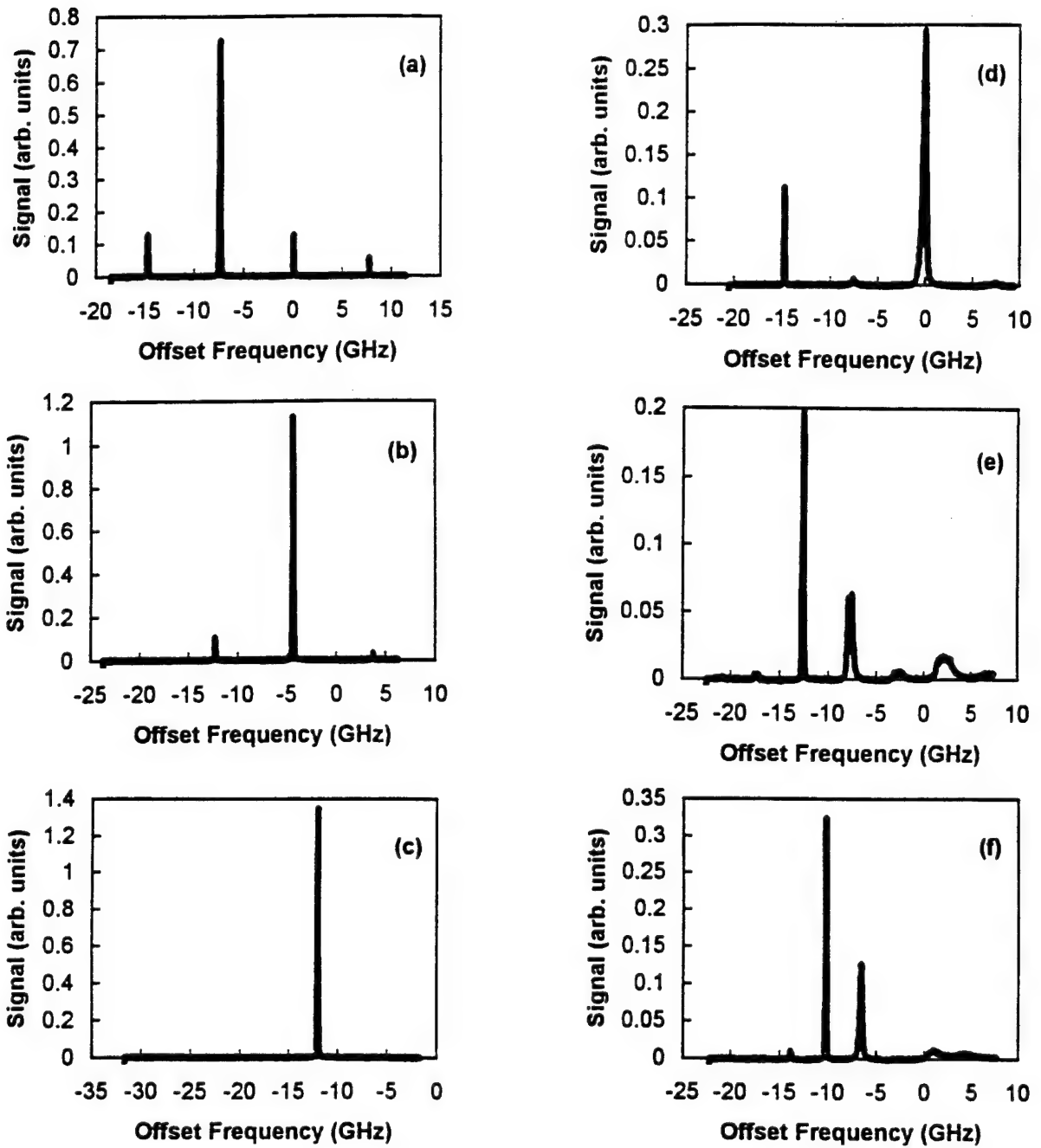
Figure 34: Measured optical spectra of the VCSEL with $\tilde{J} = 0.9$ as the injection frequency offset is shifted. The frequency axis is referenced to the free-running frequency of the VCSEL. Locked injection as the injection frequency is shifted away from resonance: (a) 0 GHz offset, (b) −4.8 GHz. (c) −12 GHz. Unlocked injection as the injection frequency is shifted towards resonance: (d) −15 GHz, (e) −12.6 GHz, and (f) −10.8 GHz.

component is easily observed. First, it causes a broadening of the laser linewidth by more than a factor of 10. Second, it causes a resonance feature in the amplitude (power) spectrum. Figure 35 shows a key characteristic of this resonance. In the figure the resonance is centered at approximately 600 MHz, 0 dB corresponds to the noise level of the measurement apparatus and −5 dB is the resolution limit. Three different power spectra are shown. When the measured polarization component is directed to be along either of the two orthogonally polarized components, the resonance feature is at a relative maximum. However, when the measured polarization direction is rotated to be 45 degrees between the two polarization components, equivalent to measuring the total spectrum without polarization selection, the resonance feature essentially disappears. This shows that the two polarization components display anti-correlated dynamics. Power in one component comes explicitly at the expense of the other so that the total power is left unchanged.

External optical injection into either of the two components can cause an enhancement or a quenching of the resonance depending on the specific injection frequency and power. This is similar to the previously discussed case where the optical injection can cause unstable dyanmics or stable injection locking in the single polarization case. Optical spectra under optical injection are shown in Figure 36. Here, the laser was operated at $\tilde{J} = 0.31$, zero frequency corresponds to the free-running frequency of the dominant peak and the orthogonal polarization component is offset by approximately 8.5 GHz. In both cases, injection on the strong peak, Figure 36(a), and the weak peak, Figure 36(b), the injection matches the polarization direction of the injected component. In the weak component spectra, there is residual signal from the strong component passed by our polarizers. In this spectra, therefore, we see the effect of the injection on the stronger orthogonal component. The orthogonal component shows resonance sidebands due to the injection. Little effect was observed when the polarization of the injected signal was orthogonal to the injected component. The injection strength was not sufficient to induce unstable dynamics directly in the strong component at the offset of the weak component. While the central peak of both polarization components is narrowed by the injection, indicating a quenching of the resonance, the dominant polarization component is clearly destabilized. Even more complicated spectra due to optical

94

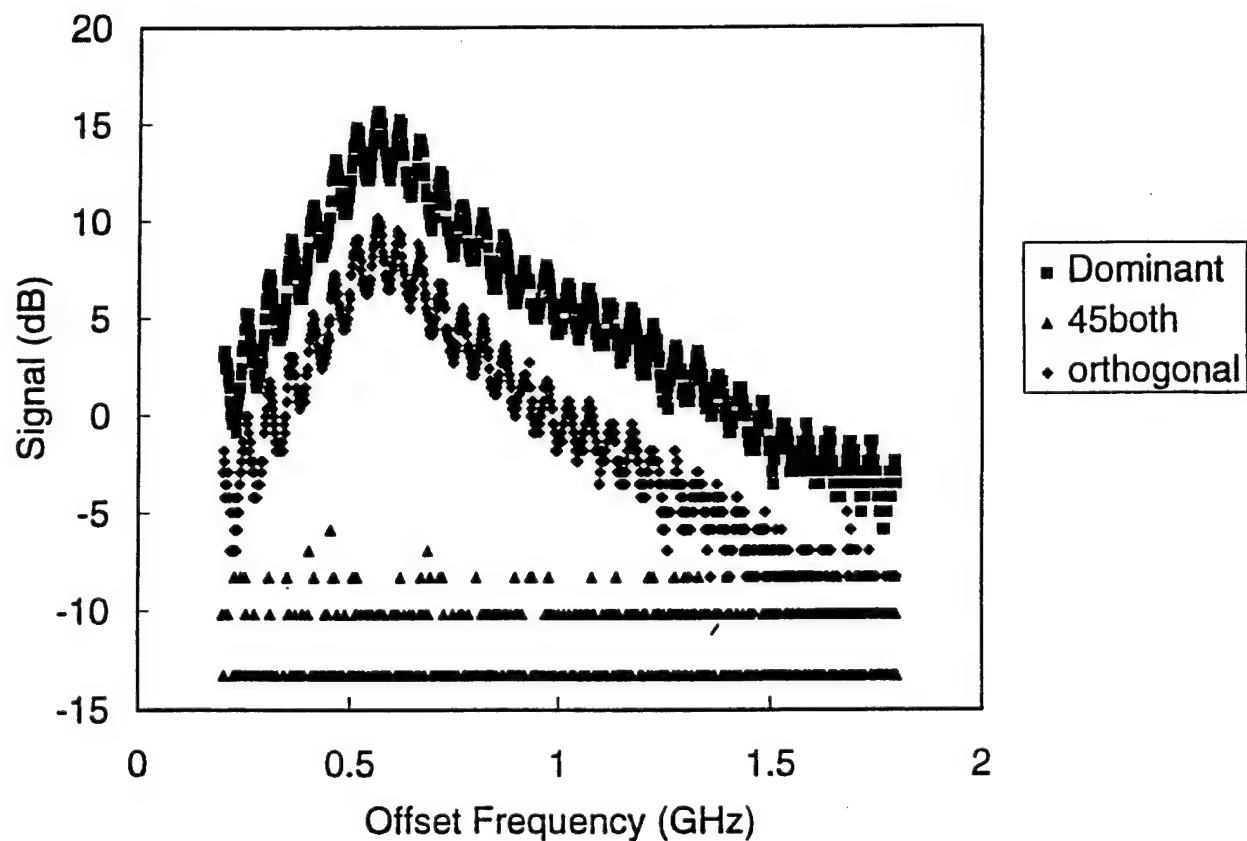Figure 35: Low-frequency power spectrum showing the resonance due to the antimode coupling between the two orthogonally polarized modes. The VCSEL was operated at $\tilde{J} = 0.31$ where the dominant polarization is approximately two orders of magnitude stronger than the orthogonal component. The resonance disappears when the output polarized 45 degrees between the two orthogonal polarizations is passed to the photodetector.

injection are observed when the two polarization components are of nearly equal strength in the free-running case. Figure 37 shows the case when $\tilde{J} = 0.38$ and the measured polarization direction is 45 degrees between the two polarization components. Injection on either peak induces a complicated structure. The details of this structure are not well understood. However, they clearly represent additional noise-like background in any modulation spectrum. For this reason, it is necesary to avoid VCSEL operation when there are two polarization components present for the types of applications that we have proposed in this program.

A more general problem was the strong influence of the intrinsic spontaneous emission noise on the spectral features. Many potential applications require low noise signals of good spectral purity. However, when the laser was operated under conditions where there would be a strong microwave modulation frequency, the resonance feature was quite broad. Figure 38 shows a typical example. The master laser, and thus the optical component at the locking frequency, had an linewidth of under 5 MHz. Therefore, the shifted Fabry-Perot resonance component was not locked but had a much broader linewidth, yielding the order of magnitude larger linewidth of the microwave modulation component in the power spectrum. The spontaneous emission noise broadens the shifted resonance feature and breaks the locking of the master laser. We have calculated the effects of a current modulation at the resonance freqeuncy, in addition to the injected optical signal. The modulation current has the effect of locking the two optical components together and sharply reducing the linewidth. However, the modulation component continued to retain fairly strong noise sidebands. Clearly, the noise characteristics of the VCSEL under investigation are not acceptable for the types of analog systems requiring good spectral purity.

Due to the effects of the polarization instability and the excitation of higher order transverse modes at higher bias currents, the VCSEL under investigation had a relatively narrow range of operating conditions where it had the potential to operate as a single-mode device. Single-mode semiconductor laser noise characteristics generally can be improved significantly by pushing the bias current far above threshold. However, the ability to do this with the
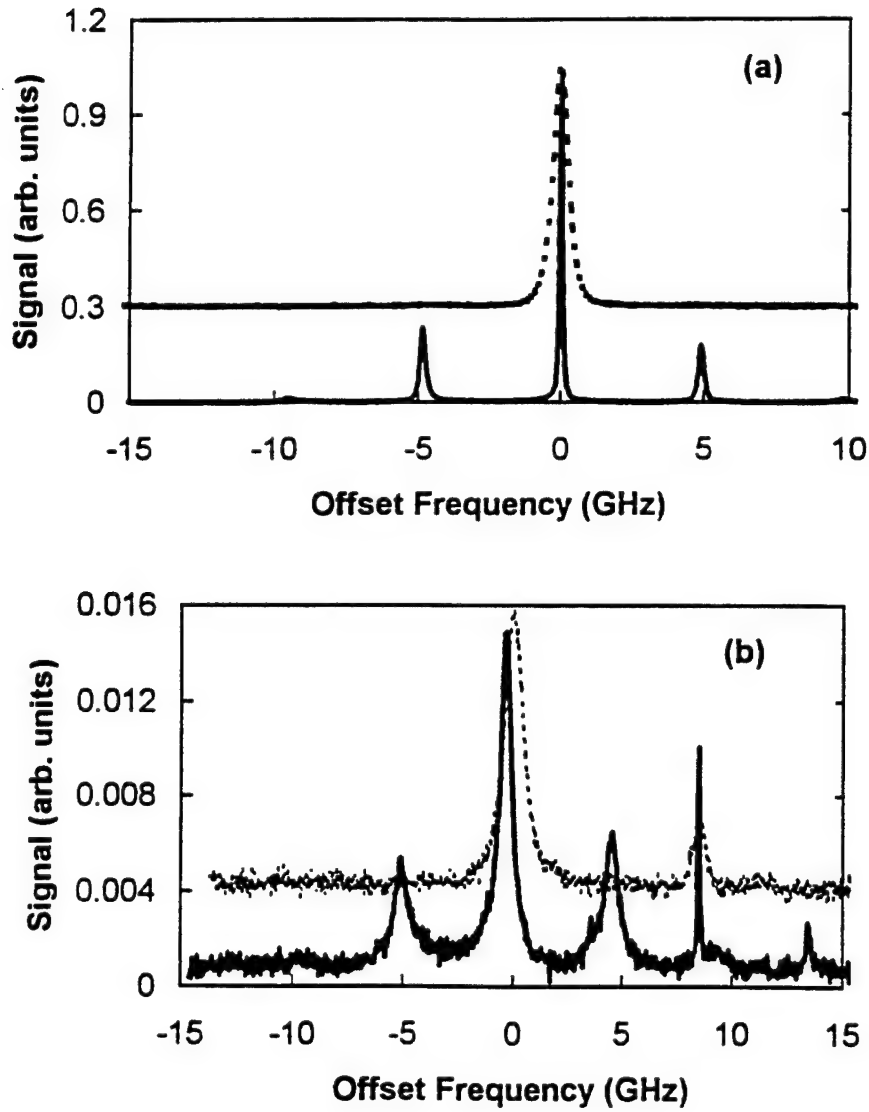
Figure 36: Optical spectra showing the effect of external optical injection on the two polarization components. $\tilde{J} = 0.31$, (a) injection and measurement parallel to the strong polarization component, and (b) injection and measurement parallel to the weak polarization component. The free-running spectra are shown offset for clarity.
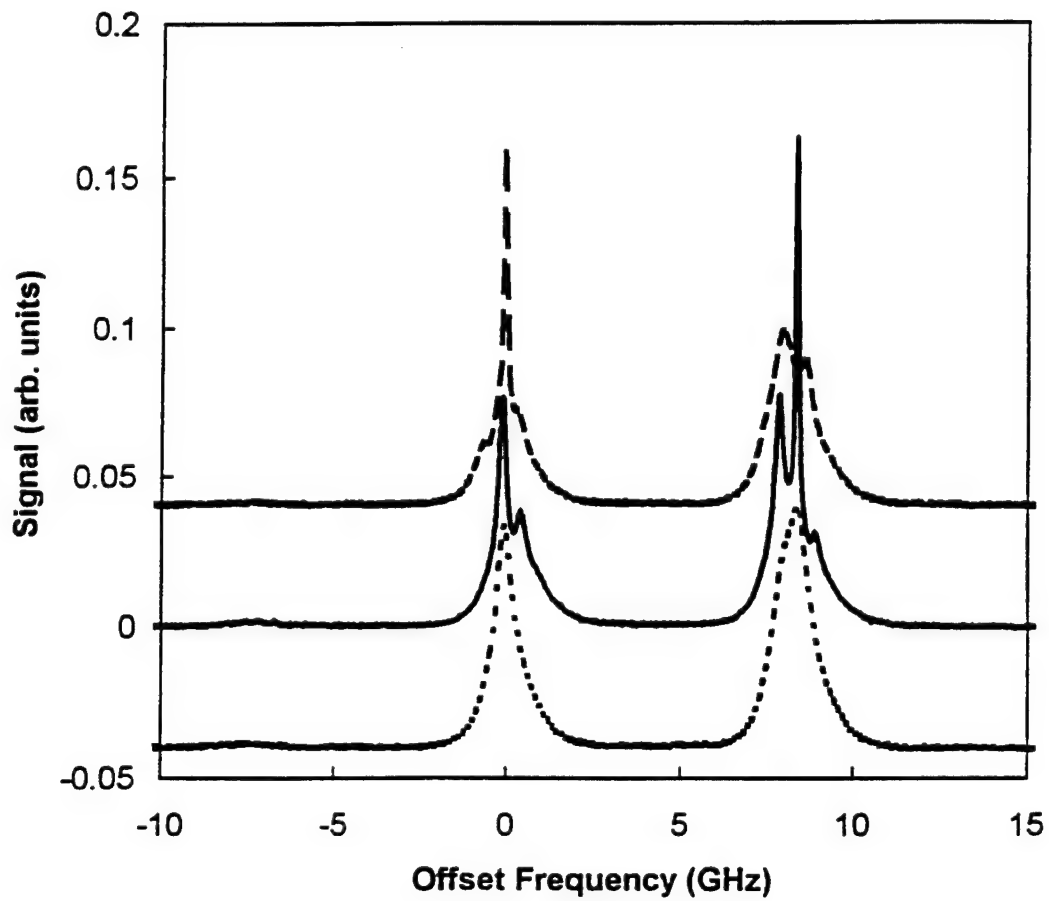
Figure 37: Optical spectra showing the effects of optical injection when the two polarization components are of similar magnitude, $\tilde{J} = 0.38$. Top, injection on the left peak. Middle, injection on the right peak. Bottom, free-running. The spectra are offset for clarity.
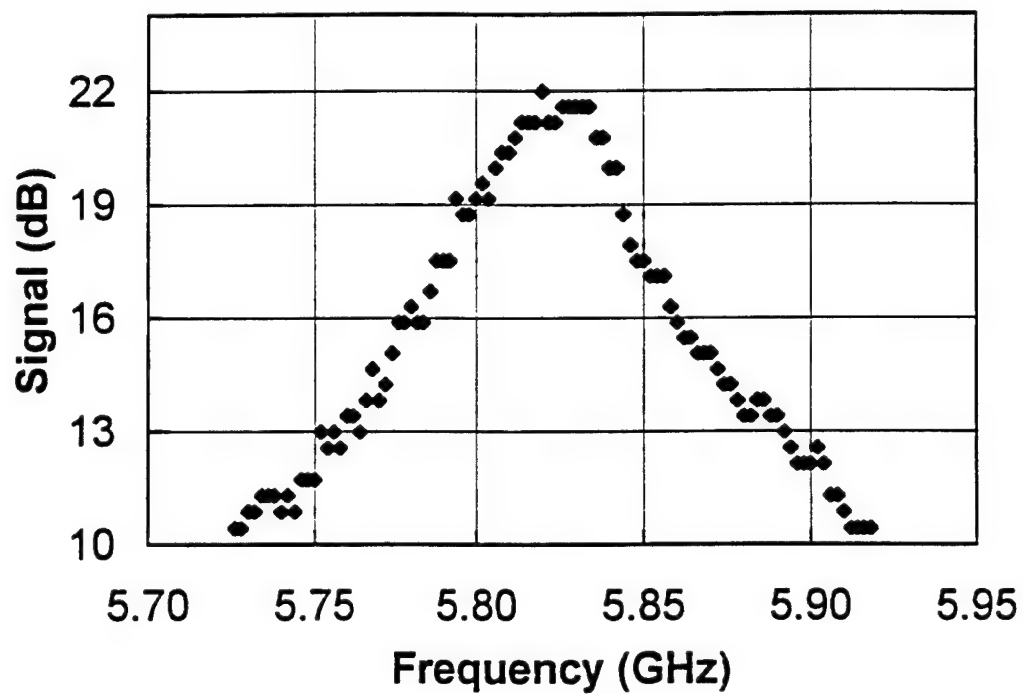
Figure 38: Power spectrum at the beat frequency between the injection-locked optical signal component and the shifted Fabry-Perot cavity resonance feature for the laser under optical injection where the optical spectrum showed two strong optical components. The bias current was 4.8 mA and the master laser had a linewidth of under 5 MHz.

VCSEL was limited by the appearance of the higher order transverse modes. This problem is not intrinsic to VCSELs and better devices are being reported in the literature.

5.0 VCSEL NEAR THRESHOLD

The threshold for laser oscillation is a prototype for the disorder-to-order transition that occurs in a wide range of physical systems [46]. It has a strong analogy with phase transitions of systems in thermal equilibrium [47]. At such transition points, the fluctuations induced by noise sources play a critical role. Noise in lasers near threshold has been studied extensively, but most analyses have concentrated on laser systems where the refractive index of the gain medium is relatively unaffected by changes in the optical gain [48]. Here, we present data starting from a free-running condition which shows a striking change in the lineshape of the semiconductor laser. While the lineshape is Lorentzian below and well above the threshold region of laser oscillation, it is near Gaussian at and just above the threshold. The Gaussian lineshape reflects the fluctuations of the cavity resonance frequency due to the carrier density fluctuations. Injection of an external optical field induces spectral holes and spikes as well as an overall shift in the Gaussian lineshape. The typical optical spectra of a semiconductor laser undergoing deterministic chaos is observed as well as a transition back to linear dynamics and a Lorentzian lineshape of the field-noise-induced spectrum at high injection levels. We observed these features in a VCSEL. However, the key point is not that the laser structure is very different from the conventional edge-emitting laser described above. It is that this laser had significantly larger values of b and γ_c. The larger value of γ_c means that the laser is noisier. All novel features observed in the spectra could be recovered using the coupled equation model.

5.1 FREE-RUNNING OPERATION

Well below and well above the threshold for laser oscillation, the lineshape of a semiconductor has been well studied and is well understood [3]. At an injection current of 3.8 mA, below the oscillation threshold, the laser exhibits a Lorentzian lineshape determined by the difference between the gain and γ_c, as shown in Figure 39(a). As has been observed previously, the linewidth of a semiconductor laser then begins to broaden as the injection current is increased
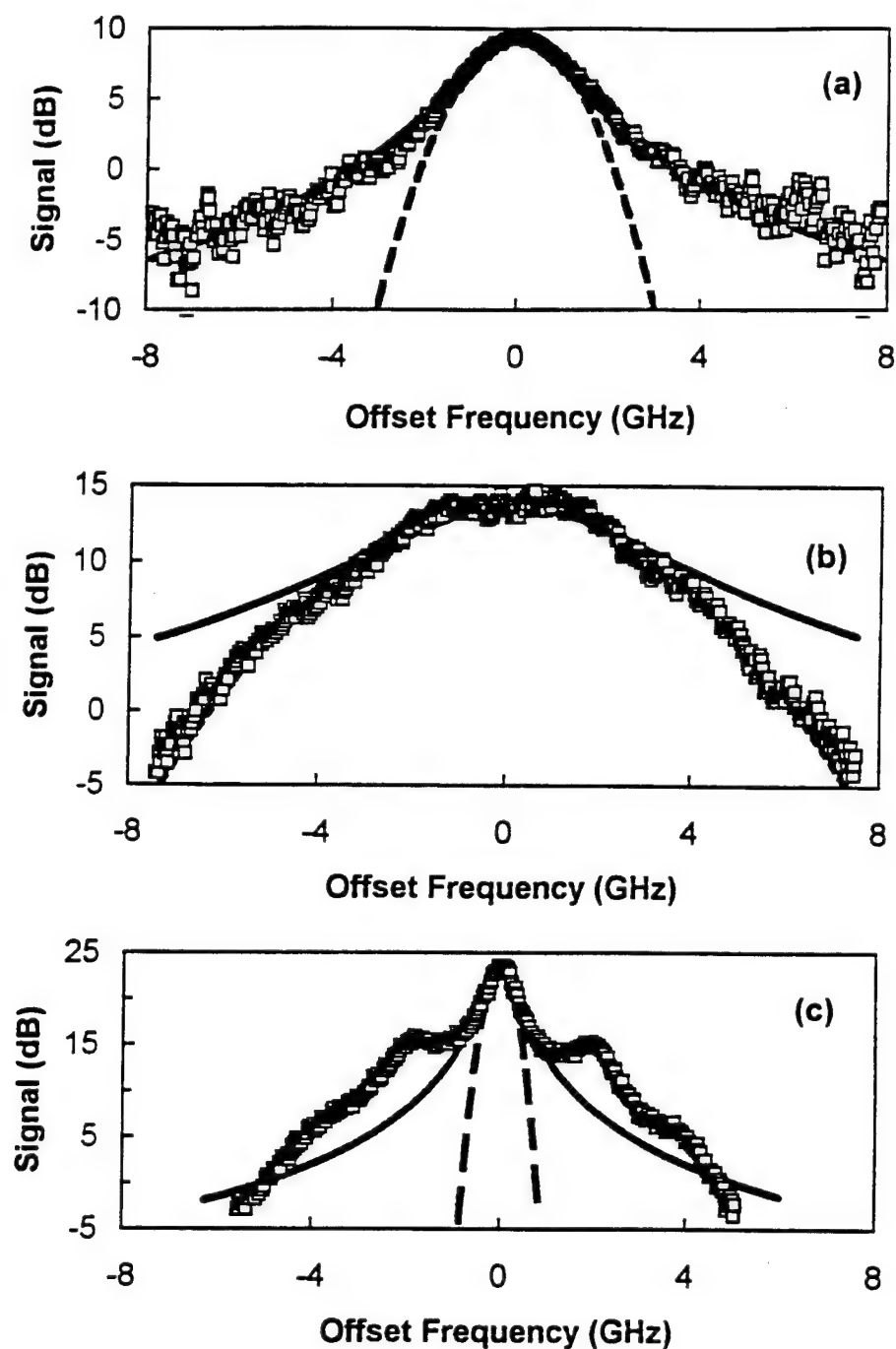
Figure 39: Measured optical spectra of a VCSEL as the bias current is varied: (a) 3.8 mA, just below the oscillation threshold, (b) 4.1 mA, above the oscillation threshold, and (c) 4.4 mA, approximately 10% above the oscillation threshold. Also shown are Lorentzian (solid line) and Gaussian (dashed line) curves fit to match the spectra full width at half maximum.

[49] due to the linewidth-enhancing effects of b [3]. We also observe in the VCSEL, and this is a key experimental feature that we wish to emphasize here, that this broadening is accompanied by a change in the lineshape from Lorentzian to near Gaussian. This is shown in Figure 39(b) where the injection current to the VCSEL is 4.1 mA. As the injection current is increased further, the Lorentzian lineshape, accompanied by relaxation resonance sidebands, reappears. This is the typical optical spectrum of a semiconductor laser biased above threshold, and the spectrum for an injection current of 4.4 mA is shown in Figure 39(c). In the wings the laser lineshape falls off more rapidly than the Lorentzian curve. This feature, along with the relaxation resonances, has been previously observed in semiconductor lasers and explained by pointing out that the linewidth enhancement factor, acting through carrier density fluctuations, is not an instantaneous effect [3]. Ultimately, for large offset frequencies, a Lorentzian lineshape reflecting only field-noise sources acting directly on the optical phase should reappear. It has been previously established in lasers where changes in the gain are not accompanied by significant changes in the refractive index that the lineshape always remains Lorentzian [48]. Past work on the lineshape of semiconductor lasers near threshold has shown non-Lorentzian lineshapes, though this point has not been emphasized, but these lineshapes were not so clearly Gaussian as was observed in our laser [49].

We have calculated the optical spectra for the VCSEL using the coupled equation model. To emphasize the generic nature of the observed phenomena, we use a simplified form of the model. Near threshold, where the circulating optical field is small, it is more convenient to use as the reference point the injection current, J_0, and the carrier density, N_0, where $\Gamma g(N_0) = \gamma_c$ when no optical field is present. Coupled equations for the two quadrature components of the optical field then replace the equations for amplitude and phase used for the above-threshold case. Near threshold, we can ignore the contributions of γ_n and γ_p to the damping due to the small value of the field. We retain the important contributions of the field dependence to the cavity resonance frequency shift and to the field-carrier resonant coupling. If we make the assumptions that $\gamma_s = \gamma_n \tilde{J}$ when $\tilde{J} = 1$ and that cavity losses are due to output coupling only, then the coupled equations take on a particularly simple form.

$$\frac{dE_1}{dt} = \frac{\gamma_c}{2}(E_1 + bE_2)\tilde{n} + A_i \cos(\Omega t) + F_1, \tag{82}$$

103

$$\frac{dE_2}{dt} = -\frac{\gamma_c}{2}(bE_1 - E_2)\tilde{n} - A_i\sin(\Omega t) + F_2, \tag{83}$$

$$\frac{d\tilde{n}}{dt} = \gamma_s(\Delta - \tilde{n}) - \frac{2\epsilon_0 n^2}{\hbar\omega_0}g_N(E_1^2 + E_2^2). \tag{84}$$

Here, E_1 and E_2 and F_1 and F_2 are the quadrature field and field-noise components, respectively. The experimentally accessible control parameter is the injection current which is normalized for numerical calculation in the parameter $\Delta = (J - J_0)/ed/\gamma_s N_0$. A convenient normalization for the equations can be made by defining $R_{sp} = \gamma_c F_0^2$ and normalizing the field equations with respect to F_0. Values for the parameters are derived from previously reported data [41] with $b = 6$, $\gamma_c = 5 \times 10^{11}$ s^{-1}, $\gamma_s = 1.1 \times 10^{-2}\gamma_c$, and

$$\frac{2\epsilon_0 n^2}{\hbar\omega_0}g_N F_0^2 = 10^{-6}\gamma_c. \tag{85}$$

Using the simplified equations, we can recover the transition from Lorentzian to near Gaussian to Lorentzian as Δ, or the injection current, is increased. Calculated optical spectra of the free-running laser are plotted in Figure 40. Due to the more simplified model, the agreement is relatively less quantitative than for the edge-emitting laser described above. Lorentzian wings are calculated for the near-Gaussian lineshape at offset frequencies beyond 25 GHz. If, however, the linewidth enhancement factor is reduced to $b = 3$, or the strength of the noise power, R_{sp}, is reduced by a factor of 2, the Gaussian lineshape at $\Delta = 0.1$ disappears, as shown in Figure 41. In either of these cases the lineshape remains essentially Lorentzian, with the relaxation resonance sidebands above threshold, throughout. We should point out that a change in the noise power is also equivalent to a simultaneous scaling of γ_s and g_N because of the intimate relationship between R_{sp} and γ_c [50].

Unlike the optical spectrum, the amplitude (intensity) spectrum of the laser field and the spectrum of carrier density fluctuations are not influenced by a change in the linewidth enhancement factor. Similarly, for the range of values considered here, they show only minor changes in shape, accompanied by an overall scaling in strength, due to a change in the amplitude of the noise source. The calculated spectra for the intensity and carrier density follow the expected profile from a linearized analysis [15], except at low frequencies due to

104

Figure 40: Calculated optical spectra (solid line) and histograms of the Fabry-Perot resonance frequency variation based on fluctuations in the carrier density (squares) using the experimentally determined VCSEL parmeters for different values of the normalized bias current parameter: (a) $\Delta = -0.02$, (b) $\Delta = 0.1$, and (c) $\Delta = 0.2$.

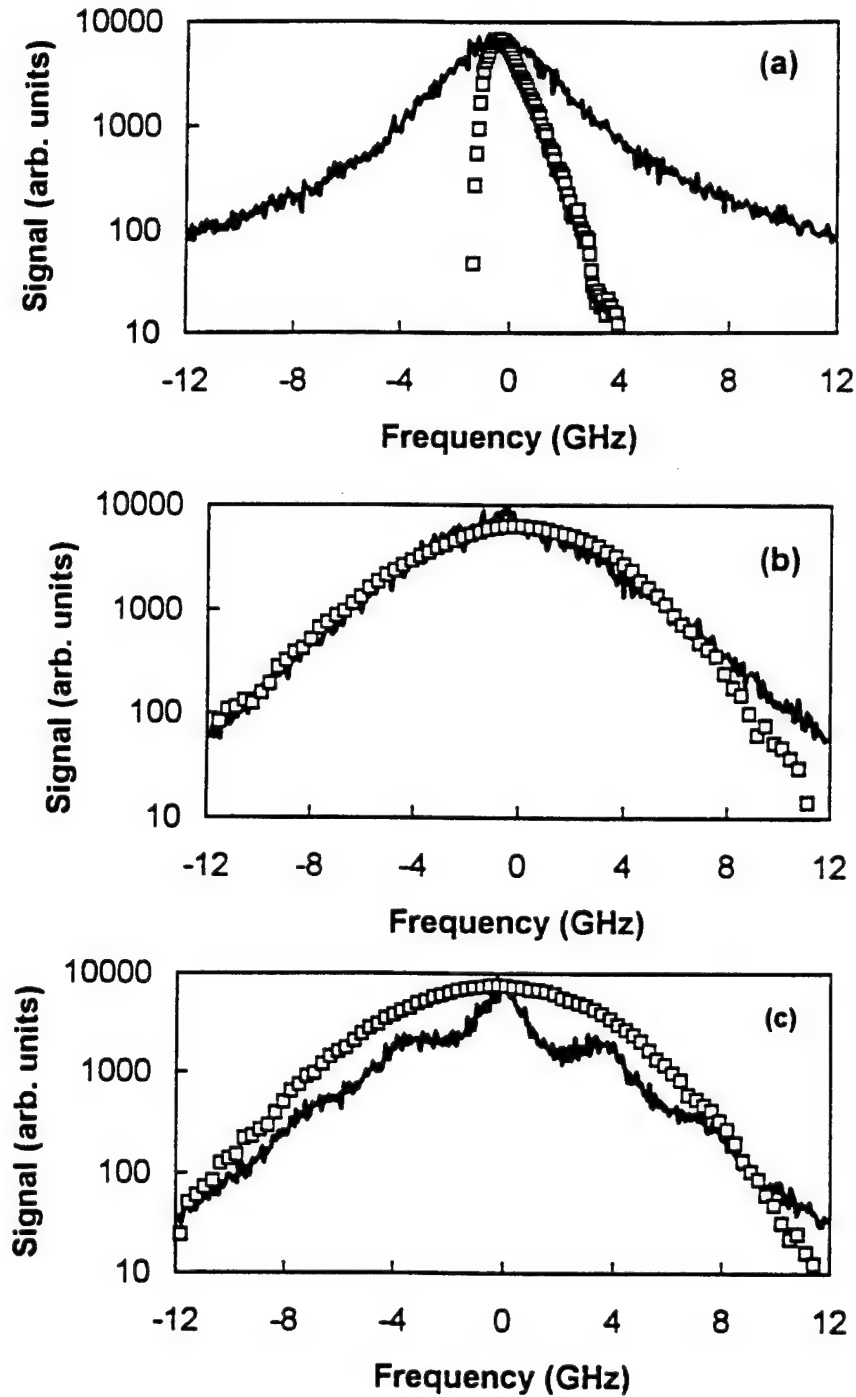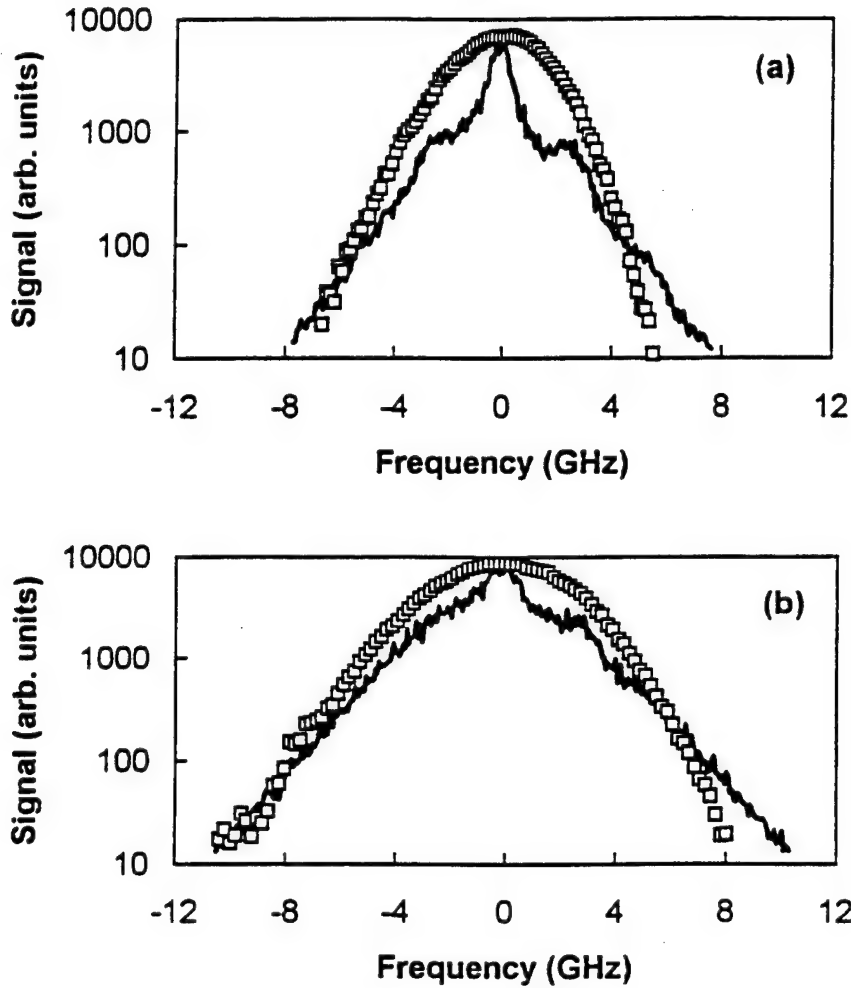Figure 41: Calculated optical spectra (solid line) and histograms of the Fabry-Perot resonance frequency variation based on fluctuations in the carrier density (squares) using modified values of the experimentally determined VCSEL parmeters for the case of Figure 16(b). In (a) the linewidth enhancement factor, $b = 3$, not 6. and in (b) the field noise power is reduced by a factor of 2. All other parameters remain the same.

the incomplete amplitude pinning near threshold. The amplitude of the laser field and the carrier density are mutually coupled but are independent of the phase of the field. While the phase fluctuations do not couple back to these two quantities, they are strongly influenced by them through the linewidth enhancement factor and the dependence of the gain on the carrier density. However, the near-Gaussian lineshape is not a result of nonlinear dynamics. All three equations can be linearized and the same lineshape will appear. In a semiconductor laser, the Lorentzian lineshape occurs when the relaxation resonances are well outside of the central linewidth so that the resonant peaks separated by the relaxation resonance frequency overlap weakly [3, 51]. Near threshold this approximation will fail. In cavities characterized by a fast photon decay rate, with correspondingly large field-noise source term, and a large linewidth enhancement factor, like the VCSEL studied here, strong deviations from the Lorentzian lineshape can be expected.

To determine the source of the near-Gaussian lineshape it is necessary to analyze the calculated time series for the carrier density equation. The carrier density fluctuations are proportional to index of refraction changes through the dependence of the gain on the carrier density. These fluctuations lead to instantaneous variations in the cavity resonant frequency. A histogram of the frequency variations is also shown in Figures 40(a) and 41. It is generated by counting the number of times the frequency (carrier density) value falls within a frequency bin interval and plotting the count as a function of frequency. This generates a curve with values proportional to the fraction of time that the particular frequency bin is the instantaneous resonant frequency. The curve of resonant frequencies is dissimilar to the laser lineshape in Figures 40(a) and (c) and in Figure 41, but follows the same Gaussian profile in Figure 40(b). At this pump level, it is the range of carrier density fluctuations that determine the laser lineshape and not the usual phase diffusion fluctuations. The instantaneous cavity resonant frequency fluctuations are caused by the same field-noise source terms as the phase diffusion fluctuations, but usually they are not a significant factor in determining the lineshape because the linewidth of each of the relaxation resonance features that forms the overall lineshape is less than the resonance frequency. Therefore, the normal phase diffusion term reasserts its dominance above threshold even though the carrier density fluctuations

persist. Only when the different relaxation resonance components show substantial overlap is there strong deviation from a central Lorentzian lineshape.

5.2 OPERATION UNDER EXTERNAL OPTICAL INJECTION

Having understood the free-running characteristics of the VCSEL near threshold, we then investigated the effects of external optical injection. We first investigated the spectral changes when the VCSEL was biased at 3.9 mA where the free-running spectrum shows only modest deviation from a Lorentzian spectrum. This study was motivated, in part, by the publication of an analysis of near-threshold VCSEL operation which used an amplifier model, as opposed to the lumped-element oscillator model we use, to describe some novel features in the optical spectra of a VCSEL under strong optical injection [24]. The model predicted that stimulated emission and absorption due to the coherent transfer of energy significantly enhanced the semiconductor response and produced new resonances in the optical spectrum which are distinct from the relaxation resonances typically observed in semiconductor lasers. Here, we show that the laser cavity plays a profound role in the generation of the new resonances and in the enhancement of the modulation bandwidth. Therefore, the lumped-element model is more appropriate than the travelling wave amplifier model.

When the free-running laser is biased near threshold and is subjected to a near-resonant locking field, the limit $|A_0^2/A_L^2| \ll 1$, and $\gamma_c \gg 2U$ and γ_s, then $U \approx \delta/2 + \gamma_c \gamma_{nL}/2\gamma_s$. In this limit, Equations 52 and 53 can be solved to show that the regen term dominates the fwm term. If the gain defect, δ, is large compared to γ_s and V, the central peak of the regen spectrum is shifted from the free-running spectrum. The difference between the two in the weak locking, large δ limit has maxima and minima shifted from the free-running frequency by $-\gamma_s[1/b \pm (1 + 1/b^2)^{1/2}]$, the same as predicted by the amplifier analysis [24]. However, Equation 52 predicts that the amplifier analysis is inadequate when the free-running laser is near or above threshold, and/or when V becomes comparable to δ. As the injecting field is increased so that U and V dominate the other rates, except for γ_c, the regen term contains a strong resonance at $\Omega \approx -V = \omega_0 - \omega_L - b\gamma_c \gamma_{nL}/2\gamma_s$. The corresponding resonance at

108

positive frequencies is much weaker due to a cancelling term, $\Omega - V$, in the numerator. The magnitude of the shift is proportional to the circulating locked power, due to the coherent field-induced carrier decay rate, γ_{nL}. Unlike the amplifier analysis, there is a multiplicative factor of approximately $b\gamma_c/2\gamma_s$ for the resonance shift. This factor is typically on the order of 100 - 1000 in semiconductor lasers. When $\gamma_c \gg \gamma_s$, a large shift in the resonance can be observed even if $\gamma_s \gg \gamma_{nL}$.

To verify these predictions, we investigated the VCSEL biased near threshold. Many of the characteristics of this VCSEL have been described previously [39, 40]. Figure 42 shows the output spectrum and the regen spectrum when the laser is biased at 4.8 mA, well above the threshold value of 3.9 mA. Total output power at this injection current is ≈ 0.35 mW and the coherent output power is ≈ 0.3 mW. Here, we can determine the key dynamic parameters of the laser from its spectra. Figure 42 shows the good agreement between data and model that is achieved using the determined parameters, $b = 6$, $\gamma_c = 5.5 \times 10^{11}$ s^{-1}, $\gamma_s = 5 \times 10^9$ s^{-1}, $\gamma_n = 3.5P \times 10^9$ s^{-1}, and $\gamma_p = 5.3P \times 10^9$ s^{-1}. P in the formulas refers to the coherent output power in milliwatts and the uncertainty for the parameters is $\pm 20\%$. The enhancement factor for the frequency shifts, relative to the amplifier case, is approximately 330.

For the injection locking measurements, the bias current was set to 3.9 mA and the output from a tunable, narrow linewidth, external cavity laser (New Focus Model 6126) was injected into the VCSEL. Output power from the free-running VCSEL was ≈ 0.02 mW. Near threshold operation insured that $|A_0^2/A_L^2| \ll 1$. Here, we concentrate on optical injection at the free-running frequency. Consistent results were obtained for detuned injection. Figure 43 shows free-running and injection-locked optical spectra taken with a high finesse optical spectrum analyzer (Newport Model SR-240C) with ≈ 60 MHz resolution. The resonance feature shifts to lower frequencies as the injection power increases.

Features from these spectra can be compared with the predictions of the model. The injection-locked output power can be determined from the spectra and the measured output
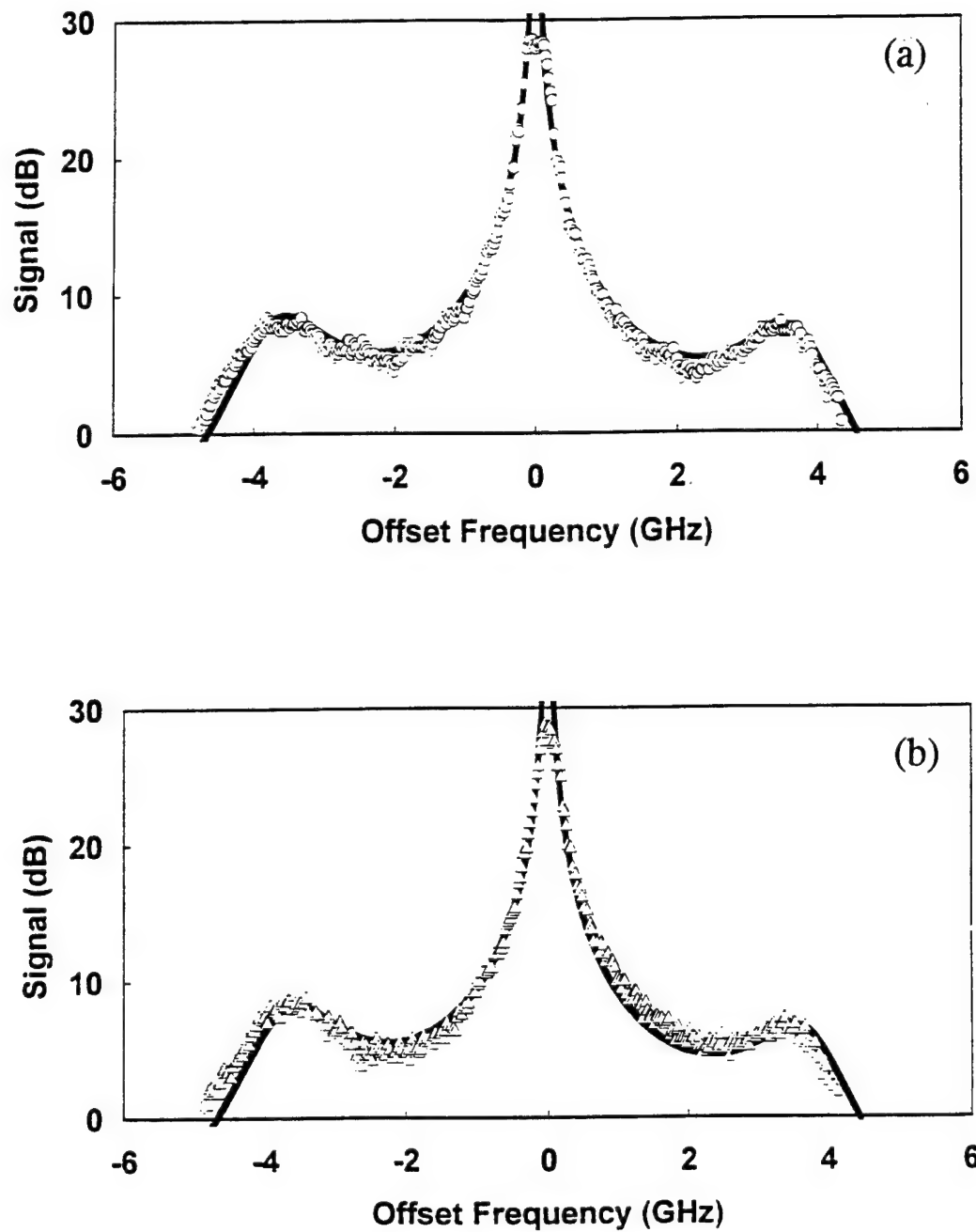
Figure 42: (a) The optical spectrum of the free-running VCSEL biased well above threshold and (b) the regeneratively amplified spectrum due to the injection of a weak optical probe. The experimental data is compared with the calculated spectra using the parameters listed in the text.
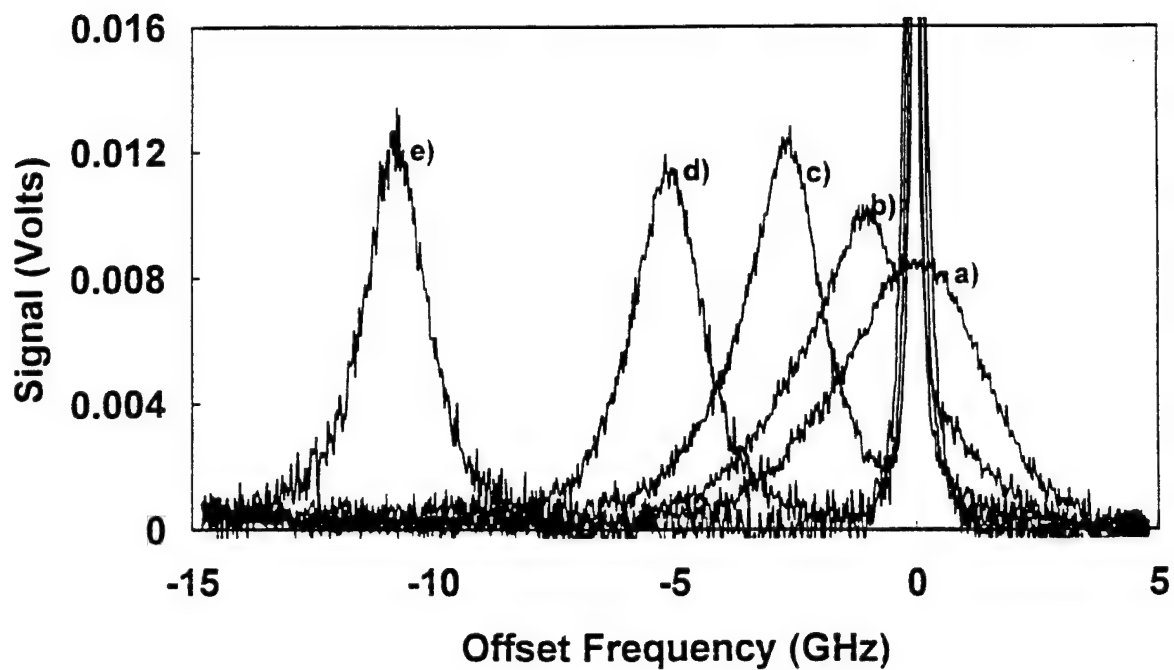
Figure 43: Representative optical spectra of the free-running VCSEL biased near threshold (a), and under increasing injected power from a narrowband laser tuned to the free running oscillation frequency (b)-(e). The injected power ratio of (b):(c):(d):(e) is 1:10:100:1000.

power. Figure 44 shows the dependence of the injection-locked coherent power and the frequency shift of the resonance on the power injected into the VCSEL. Because we are unable to independently determine the coupling parameter, η, we can only make a relative measurement of the injection power and the relative uncertainty is $\pm 50\%$. Using the experimentally determined parameters, model calculations for both the injection-locked coherent power and the frequency shift are in good agreement with the data. At high injection power levels, the offset frequency scales linearly with the injection-locked coherent power, and both scale with the cube root of the injected power. Even at the highest injected power measured, where the injection-locked coherent power is ≈ 0.07 mW, the field-induced enhancements of the decay rate are $\gamma_{nL} \approx 0.05\gamma_s$ and $\gamma_{pL} \approx 0.075\gamma_s$. These values coincide with the expected values at the lower operating power.

The lumped-circuit analysis of laser oscillation assumes that spatial effects can be averaged over the mode profiles. It has given excellent quantitative agreement with a wide variety of single-mode semiconductor lasers, including Fabry-Perot edge emitting lasers with large output coupling [7, 13]. The linearized treatment, like that given here, fails to accurately reproduce the central linewidth of the free-running laser and, more generally, the dynamics whenever a resonance becomes unstable, but it shows good accuracy in the prediction of the positions and shifts of the resonance frequencies. The laser cavity strongly enhances the frequency shifts induced by the injection field beyond what is expected from the increased stimulated emission due to the stronger oscillating field. Phase and amplitude characteristics must be analyzed for a detailed quantitative understanding of the spectral features.

When the free-running Gaussian-lineshape laser is subjected to external optical injection, several spectral changes occur. As before, we first concentrate on resonant injection. The first observable change as the injection level is increased is a shifting of the spectrum to lower optical frequencies. This reflects the drop in the overall carrier density due to the higher circulating field and enhanced stimulated emission. As the injection level is increased further, the spectrum shows a new spike at negative offset frequencies and a dip at positive offset frequencies in addition to the overall shift and a spike at the injection frequency, as
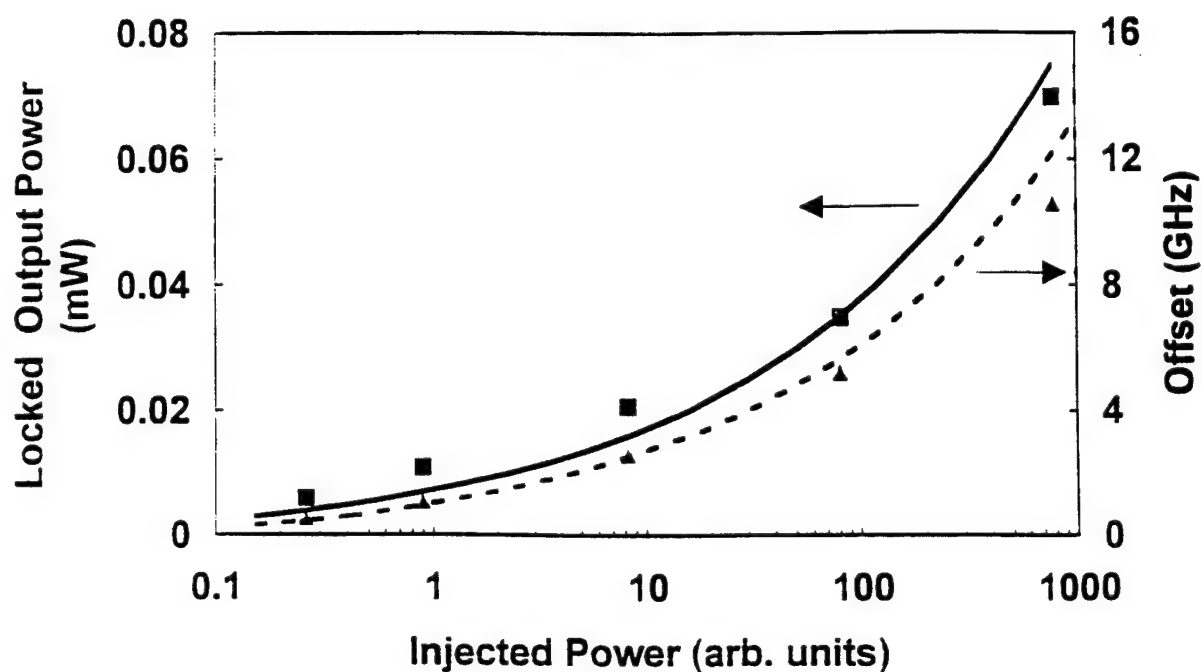
Figure 44: The dependence of the injection-locked power, (□)-data and (——)-model, and the shift of the resonance from the free-running frequency, (△)-data and (– –)-model, for the VCSEL biased near threshold when subject to an injected signal at the free-running oscillation frequency.

shown in Figure 45(a). The free-running spectrum is also shown for reference. The spike and dip are oppositely offset by 1 GHz, approximately the relaxation resonance frequency. As the excitation level is increased further, spikes and dips appear at multiples of the original offset, corresponding to the different resonance features. At higher excitation levels, the spectra are similar to the chaotic dynamics spectra discussed above, Figure 45(b). Finally, at very high excitation levels, the spectral structure has shifted away from the excitation peak and assumed a more Lorentzian lineshape, Figure 39(c). Calculated spectra show the progression from shift with spike and dip, Figure 46(a), to chaotic-like, Figure 46(b), to shifted Lorentzian, Figure 46(c).

We have previously presented the shift of the Fabry-Perot resonance feature due to optical injection when this laser was initially biased at 3.9 mA, at the laser threshold [41]. There, the initial deviation from Lorentzian was not large but the spectra clearly showed a narrowing and a progression to a more Lorentzian lineshape as the injected power was increased. This effect can also be seen as the laser frequency is tuned across the resonance at strong injection levels at the higher operating current described by the spectra presented here. Figure 47 plots this trend under strong external injection. For large positive detunings the Gaussian lineshape is retained but there is a shift of the feature. As the detuning is decreased the feature narrows, with increased amplitude. For injection close to the edge of the locking range, near −24 GHz, the emission feature becomes weak, indicating stable, injection-locked operation. The smooth progression of the shift of the Fabry-Perot resonance feature is summarized in Figure 48. For positive detunings, the shift decreases with increasing offset as the injection undergoes less amplification in the cavity. For negative detunings the shift is greater than but approaching the magnitude of the injection offset as the offset decreases to more negative values. At the edge of the locking range this smooth progression abruptly halts and the laser displays a weaker, more complex spectrum. The shift of the cavity resonance frequency and the associated damping are caused by the reduced carrier density under strong external injection. The dynamics are strongly influenced by the magnitude of the shift and damping.
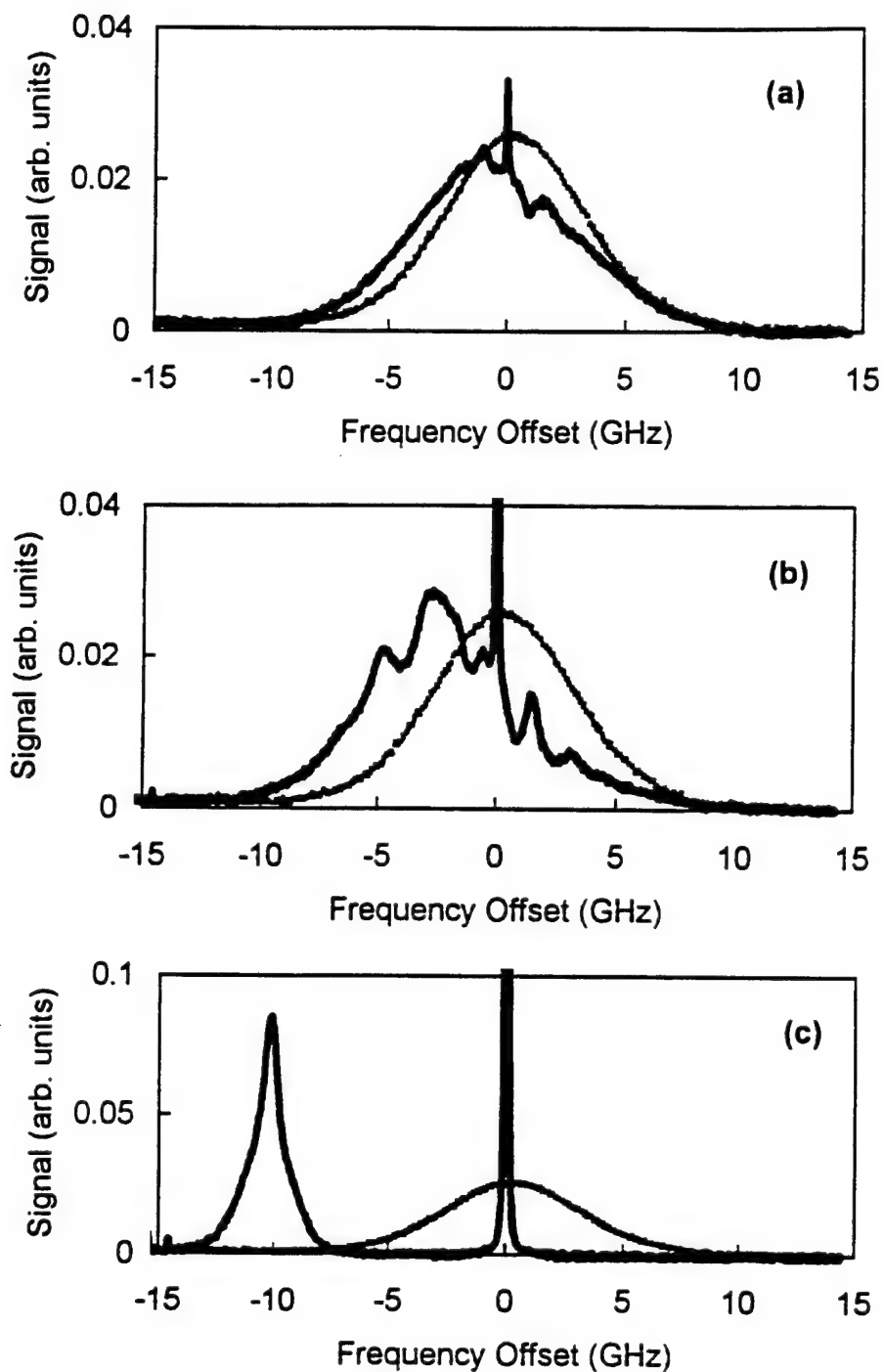
Figure 45: Measured optical spectra of the VCSEL biased at 4.1 mA and subjected to external optical injection. The ratio of injected power is: (a) 1, (b) 10, (c) 940. The free-running spectrum is also shown for reference.
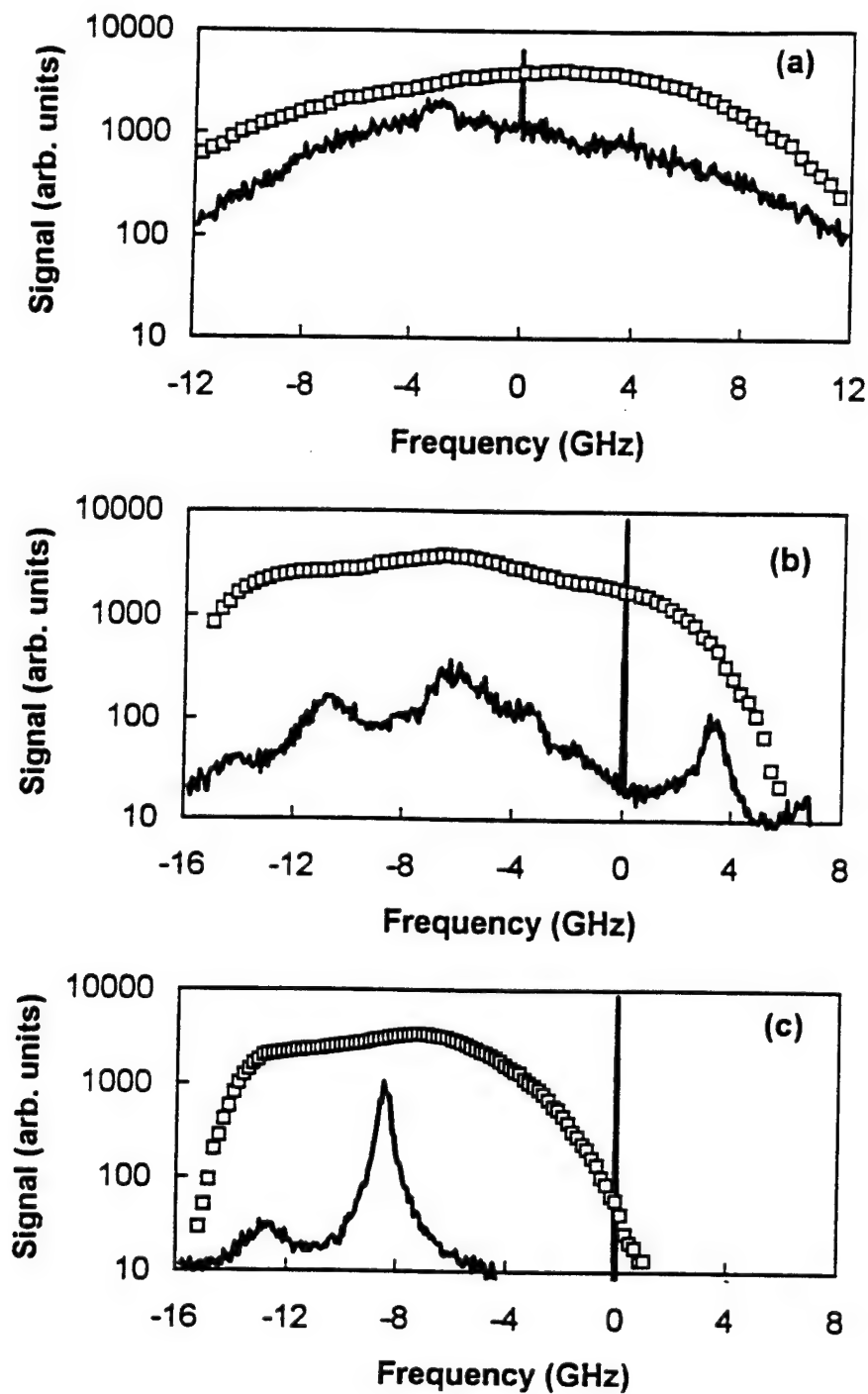
Figure 46: Calculated optical spectra of the VCSEL biased at 4.1 mA and subjected to external optical injection. The ratio of injected optical power is: (a) 1, (b) 4, (c) 100.
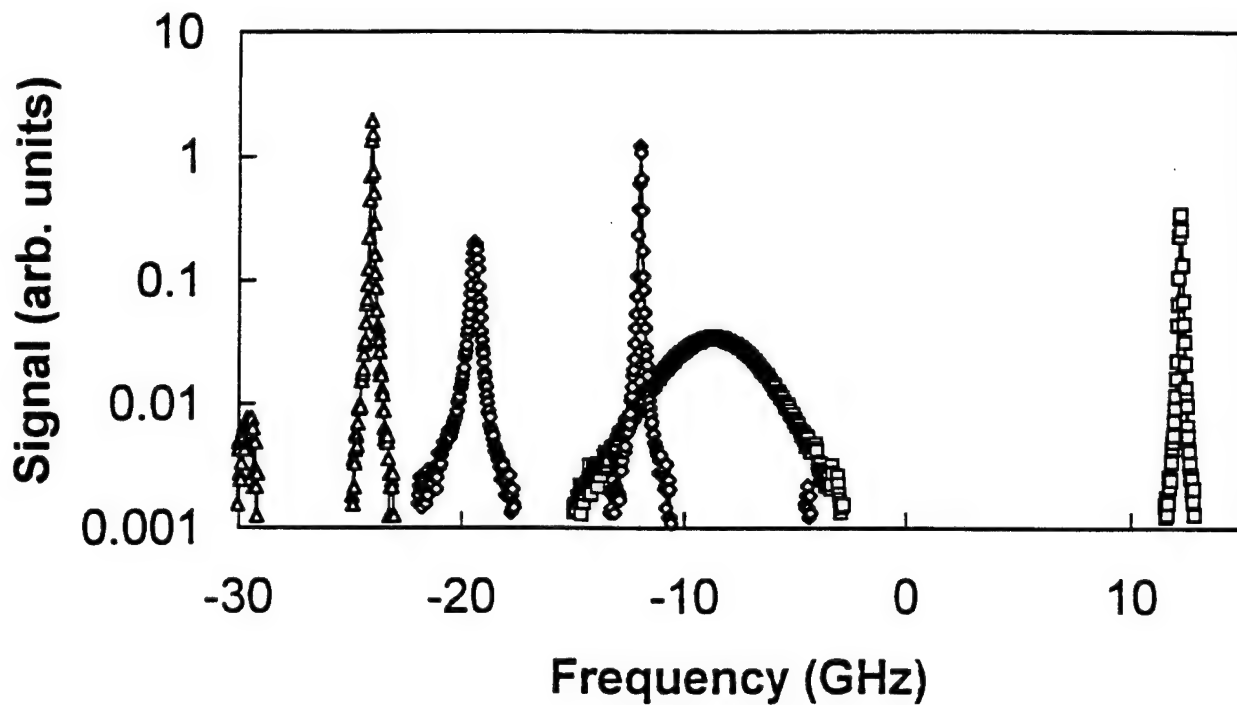
Figure 47: Spectra of the VCSEL under strong optical injection as the detuning is varied: 12 GHz (squares), −12 GHz (diamonds), and −24 GHz (triangles). Each spectrum has two principal features, the regeneratively amplified injected signal and the regeneratively amplified spontaneous emission at the shifted Fabry-Perot resonance peak of −8.5 GHz, −19.5 GHz, and −29.5 GHz, respectively. The −12 GHz offset excitation spectrum also shows a weak four-wave mixing peak at −4.5 GHz.
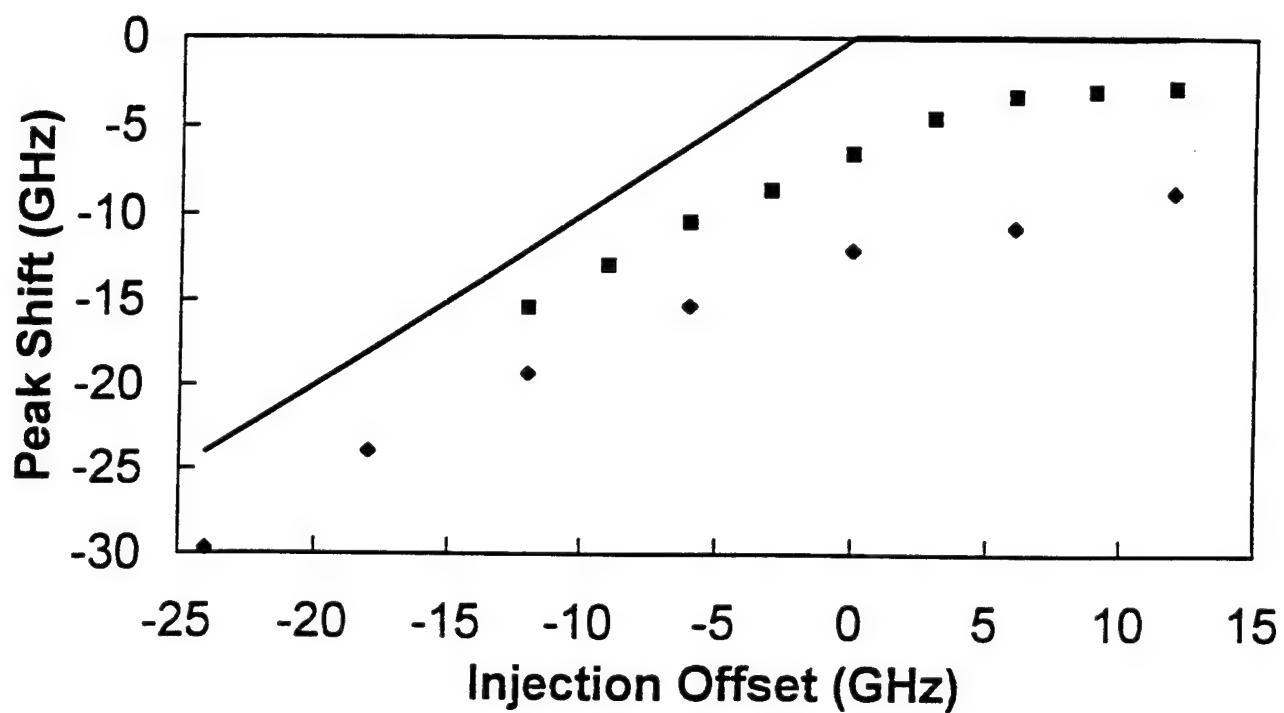
Figure 48: Measured pushing of the Fabry-Perot resonance as a function of the detuning of the injected signal. The diamonds are for an injected power approximately an order of magnitude stronger than the squares. The solid line is a slope of one line at negative offsets and slope of zero line at positive offsets to aid the eye.

6.0 CONCLUSIONS

The work done under this program has identified the key output characteristics and nonlinear dynamics of a semiconductor laser subject to external optical injection. It has confirmed that the coupled equation model for a semiconductor laser under optical injection predicts and/or reproduces the spectral characteristics that we observe. This has allowed us to identify the underlying deterministic dynamics that, to a large extent, determine the output characteristics of the semiconductor laser under optical injection. We have verified that bandwidth enhancement and noise reduction can be simultaneously achieved in an injection-locked laser diode. Certainly, there is no sacrifice in the dynamic range of an appropriately injection-locked semiconductor laser and there can be considerable enhancement as well as reduction of the frequency chirp which limits the effectiveness of laser diodes in certain applications. In the region of unstable dynamics, we have been able to generate a broadly tunable modulation signal when the master laser is appropriately tuned to the region of limit cycle, period one, oscillations under strong injection. However, the microwave signal generated by the beating of optical components is quite noisy when the laser is excited to display unstable dynamics due to the strong effects of spontaneous emission noise. More work is necessary to improve the operating characteristics in this region. We have observed that feedback can modify the modulation characteristics. Perhaps it can be used to improve the stability of the unstable modulation feature as well. Several novel spectral characteristics have been observed in a VCSEL. These include a Gaussian lineshape near threshold, strong frequency pushing of the Fabry-Perot resonance signal, and a locking/unlocking bistability. All observed features have been understood by comparing measured spectra with the predictions of the model. Under strong injection locking, semiconductor lasers are calculated to be able to achieve bandwidths broadly tunable in the millimeter-wave region, with tunable modulation characteristics and reduced noise relative to the free-running case. This technique may be very useful for augmenting the performance of available laser diodes so that they can be useful in a variety of applications.

119

References

[1] Yamamoto, Y. and Imoto, N., "Internal and External Field Fluctuations of a Laser Oscillator: Part I-Quantum Mechanical Langevin Treatment," <u>IEEE Journal of Quantum Electronics</u>, Vol. QE-22, No. 10, pp. 2032-2042, October 1986.

[2] Tredicce, J.R., Arecchi, F.T., Lippi, G.L. and Puccioni, G.P., "Instabilities in lasers with an injected signal," <u>Journal of the Optical Society of America B</u>, Vol. 2, No. 1, pp. 173-183, January 1985.

[3] Henry, C.H., "Phase noise in semiconductor lasers," <u>Journal of Lightwave Technology</u>, Vol. LT-4, No. 3, pp. 298-311, March 1986.

[4] Sacher, J.,Baums, D.,Panknin, P., Elsässer, W. and E.O. Göbel, "Intensity instabilities of semiconductor lasers under current modulation, external light injection, and delayed feedback," <u>Physical Review A</u>, Vol. 45, No. 3, pp. 1893-1905, 1 February 1992.

[5] Chen, Y.C., Winful, H.G. and Liu, J.M., "Subharmonic bifurcations and irregular pulsing behavior of modulated semiconductor lasers," <u>Applied Physics Letters</u>, Vol. 47, No. 3, pp. 208-210, 1 August 1985.

[6] Mørk, J., Mark, J. and Tromborg, B., "Route to chaos and competition between relaxation oscillations for a semiconductor laser with optical feedback," <u>Physical Review Letters</u>, Vol. 65, No. 16, pp. 1999-2002, 15 October 1990.

[7] Simpson, T.B., Liu, J.M., Gavrielides, A., Kovanis, V. and Alsing, P.M., "Period-doubling cascades and chaos in semiconductor lasers subject to optical injection." <u>Physical Review A</u>, Vol. 51, No. 5, pp. 4181-4185, May 1995.

[8] Simpson, T.B., Liu, J.M., Gavrielides, A., Kovanis, V. and Alsing, P.M., "Period-doubling route to chaos in a semiconductor laser subject to external optical injection." <u>Applied Physics Letters</u>, Vol. 64, No. 26, pp. 3539-3541, 27 June 1994.

[9] Kovanis, V, Gavrielides, A., Simpson, T.B. and Liu, J.M., "Instabilities and chaos in optically injected semiconductor lasers," <u>Applied Physics Letters</u>, Vol. 67, No. 19, pp. 2780-2782, 6 November 1995.

[10] Gavrielides, A., Kovanis, V., Varangis, P., Erneux, T. and Simpson, T.B., "Subharmonic resonances in an optically injected semiconductor laser," <u>Proceedings SPIE</u>, Vol. 2693, pp. 654-665, 1996.

[11] Simpson, T.B., Liu, J.M. and Gavrielides, A., "Bandwidth enhancement and broadband noise reduction in injection-locked semiconductor lasers," <u>IEEE Photonics Technology Letters</u>, Vol. 7, No. 7, pp. 709-711, July 1995.

[12] Simpson, T.B., Liu, J.M. and Gavrielides, A., "Small signal analysis of modulation characteristics in a semiconductor laser subject to strong optical injection," <u>IEEE Journal of Quantum Electronics</u>, Vol. 32, No. 8, pp. 1456-1468, August 1996.

[13] Liu, J.M. and Simpson, T.B., "Four-wave mixing and optical modulation in a semiconductor laser," IEEE Journal of Quantum Electronics, Vol. 30, No. 4, pp. 957-965, April 1994.

[14] Agrawal, G.P. and Dutta, N.K., Long-Wavelength Semiconductor Lasers. Van Nostrand Reinhold, New York, 1986.

[15] Simpson, T.B. and Liu, J.M., "Spontaneous emission, nonlinear optical coupling and noise in laser diodes," Optics Communications, Vol. 112, No. 1, pp. 43-47, 1 November 1994.

[16] Yamamoto, Y., Machida, S. and Nilsson, O., "Amplitude squeezing in a pump-noise-suppressed laser oscillator," Physical Review A, Vol. 34, No. 5, pp. 4025-4042, November 1986.

[17] Bowers, M.S. and Moody, S.E., "Cavity equations for a laser with an externally injected signal," Journal of the Optical Society of America B, Vol. 11, No. 11, pp. 2266-2275, November 1994.

[18] Simpson, T.B. and Liu, J.M., "Phase and amplitude characteristics of nearly degenerate four-wave mixing in Fabry-Perot semiconductor lasers," Journal of Applied Physics, Vol. 73, No. 5, pp. 2587-2589, 1 March 1993.

[19] Mogensen, F., Olesen, H. and Jacobsen, G., "Locking conditions and stability properties for a semiconductor laser with external light injection," IEEE Journal of Quantum Electronics, Vol. QE-21, No. 7, pp. 784-793, July 1985.

[20] Petitbon, I., Gallion, P., Debarge, G. and Chabran, C, "Locking bandwidth and relaxation oscillations of an injection-locked semiconductor laser," IEEE Journal of Quantum Electronics, Vol. 24, No. 2, pp. 148-154, February 1988.

[21] Spano, P., Piazzolla, S. and Tamburrini, M., "Frequency and intensity noise in injection-locked semiconductor lasers: theory and experiments," IEEE Journal of Quantum Electronics, Vol. QE-22, No. 3, pp. 427-435, March 1986.

[22] Li, L. and Petermann, K., "Small-signal analysis of optical-frequency conversion in an injection-locked semiconductor laser," IEEE Journal of Quantum Electronics, Vol. 30, No. 1, pp. 43-48, January 1994.

[23] Li, L., "Static and dynamic properties of injection-locked semiconductor lasers," IEEE Journal of Quantum Electronics, Vol. 30, No. 8, pp. 1701-1708, August 1994.

[24] Agrawal, G.P., "Population pulsations and nondegenerate four-wave mixing in semiconductor lasers and amplifiers," Journal of the Optical Society of America B, Vol. 5, No. 1, pp. 147-158, January 1988.

[25] Lowry, C.W., Brown de Colstoun, F., Paul, A.E., Khitrova, G., Gibbs, H.M., Grantham, J.W., Jin, R., Boggavarapu, D., Koch, S.W., Sargent III, M., Brennan, T.M. and Hammons, B.E., "Acceleration of coherent energy transfer by stimulated emission and absorption," Physical Review Letters, Vol. 71, No. 10, pp. 1534-1537, 6 September 1993.

[26] Ralston, J.D., Weisser, S., Esquivias, I., Larkins, E.C., Rosenzweig, J., Tasker, P.J. and Fleissner, J., "Control of differential gain, nonlinear gain, and damping factor for high-speed application of GaAs-based MQW lasers," IEEE Journal of Quantum Electronics, Vol. 29, No. 6, pp. 1648-1659, June 1993.

[27] Mork, J., Mark, J. and Tromborg, B., "Route to Chaos and Competition Between Relaxation Oscillations for a Semiconductor Laser with Optical Feedback," Physical Review Letters, Vol. 65, No. 16, pp. 1999-2002, 15 October 1990.

[28] Press, W.H., Teukolsky, S.A., Vetterling, W.T. and Flannery, B.P., Numerical Recipes in Fortran. Cambridge University Press, New York, 1992.

[29] Riggs, T.L. and Phillips, C.L., "Modeling continuous noise sources in digital simulations," Simulation, Vol. 48, No. 1, pp. 11-18, 1987.

[30] Helfand, E. "Numerical integration of stochastic differential equations," Bell System Technical Journal, Vol. 58, No. 10, pp. 2289-2299, 1979.

[31] Greenside, H.S. and Helfand, E., "Numerical integration of stochastic differential equations - II," Bell System Technical Journal, Vol. 60. No. 8, pp. 1927-1940, 1981.

[32] Piazzolla, S., Spano, P. and Tamburrini, M., "Small signal analysis of frequency chirping in injection-locked semiconductor lasers," IEEE Journal of Quantum Electronics, Vol. QE-22, No. 12, pp. 2219-2223, December 1986.

[33] Gallion, P., Nakajima, H., Debarge, G. and Chabran, C., "Contribution of spontaneous emission to the linewidth of an injection-locked semiconductor laser," Electronics Letters, Vol. 21, No. 14, pp. 626-628, 4 July 1985.

[34] Simpson, T.B. and Liu, J.M., "Enhanced modulation bandwidth in injection-locked semiconductor lasers," IEEE Photonics Technology Letters, to be published, October 1997.

[35] Hui, R., D'Ottavi, A. Mecozzi, A. and Spano, P., "Injection locking in distributed feedback semiconductor lasers," IEEE Journal of Quantum Electronics, Vol. 27, No. 6, pp. 1688-1695, June 1991.

[36] Mohrdiek, S., Burhard, H. and Walter, H., "Chirp Reduction of Directly modulated Semiconductor Lasers at 10 Gb/s by Strong CW Light Injection," Journal of Lightwave Technology, Vol. 12, No. 3, pp. 418-424, March 1994.

[37] Yabre, G., "Effect of relatively strong light injection on the chirp-to-power ratio and the 3 dB bandwidth of directly modulated semiconductor lasers," Journal of Lightwave Technology, Vol. 14, No. 10, pp. 2367-2373, October 1996.

[38] Yabre, G. and Le Bihan, J., "Reduction of nonlinear distortion in directly modulated semiconductor lasers by coherent light injection," IEEE Journal of Quantum Electronics, Vol. 33, No. 7, pp. 1132-1140, July 1997.

[39] Chen, H.M., Tai, K., Huamg, K.F., Kao, Y.H. and Wynn, J.D., "Instability in surface emitting lasers due to external feedback," Journal of Applied Physics, Vol. 73, No. 1, pp. 16-19, 1 January 1993.

[40] Tai, K., Lai, Y., Huang, K.F., Huang, T.C., Lee, T.D. and Wu, C.C., "Transverse mode emission characteristics of gain-guided surface emitting lasers," Applied Physics Letters, Vol. 63, No. 19, pp. 2624-2646, 8 November 1994.

[41] Simpson, T.B., Liu, J.M., Huang, K.F., Tai, K., Clayton, C.M., Gavrielides, A. and Kovanis, V., "Cavity enhancement of resonant frequencies in semiconductor lasers subject to optical injection," Physical Review A, Vol 52, No. 6, pp. R4348-R4351, December 1995.

[42] Parker, T.S. and Chua, L.O., Practical Numerical Algorithms for Chaotic Systems. Springer-Verlag, New York, 1989.

[43] Wang, J., Halder, M.K., Li, L. and Mendis, F.V.C., "Enhancement of modulation bandwidth of laser diodes by injection locking," IEEE Photonics Technology Letters, Vol. 8, No. 1) pp. 34-36, January 1996.

[44] Olshansky, R., Hill, P., Lanzisera, V. and Powazinik, W., "Frequency response of 1.3 μm InGaAsP high speed semiconductor lasers," IEEE Journal of Quantum Electronics, Vol. QE-23, No. 9, pp. 1410-1418, September 1987.

[45] Boggavarapu, D., Grantham, J.W., Hu, Y.Z., Gibbs, H.M., Khitrova, G., Koch, S., Sargent, M. III, and Chow, W.W., "Injection locking of vertical-cavity surface-emitting laser," Nonlinear Dynamics in Optical Systems Technical Digest, OSA Technical Digest Series, Vol. 16, pp. 281-283, 1992.

[46] Haken, H., Synergetics. Springer-Verlag, Berlin, 1983.

[47] Sargent, M. III, Scully, M.O. and Lamb, W.E. Jr., Laser Physics. Addison-Wesley, Reading, MA, 1974.

[48] Lax, M., "The theory of laser noise," Proceeedings SPIE, Vol. 1376, pp. 2-20, 1991.

[49] Hui, R., Benedetto, S. and Montrosset, I., "Near threshold operation of semiconductor lasers and resonant-type laser amplifiers," IEEE Journal of Quantum Electronics, Vol. 29, No. 6, pp. 1488-1497, June 1993.

[50] Björk, G., Karlsson, A. and Yamamoto, Y., "On the linewidth of microcavity lasers," Applied Physics Letters, Vol. 60, No. 3, pp. 304-306, 20 January 1992.

[51] Vahala, K. and Yariv, A., "Semiclassical theory of noise in semiconductor lasers-part II," IEEE Journal of Quantum Electronics, Vol. QE-19, No. 6, pp. 1102-1109, June 1983.

DISTRIBUTION LIST

AUL/LSE
Bldg 1405 - 600 Chennault Circle
Maxwell AFB, AL 36112-6424   1 cy

DTIC/OCP
8527 John J. Kingman Rd, Suite 0944
Ft Belvoir, VA 22060-6218   2 cys

AFSAA/SAI
1580 Air Force Pentagon
Washington, DC 20330-1580   1 cy

PL/SUL
Kirtland AFB, NM 87117-5776   2 cys

PL/HO
Kirtland AFB, NM 87117-5776   1 cy

Official Record Copy
  PL/LIMS/Chris Clayton   4 cys

Thomas B. Simpson   2 cys
Jaycor, Inc
P.O. Box 85154
San Diego, CA 92186-5154

Jia-ming Liu   2cys
Department of Electrical Engineering
University of California, Los Angeles
Los Angeles, CA 90024-159410